UiT The Arctic University of Norway

Faculty of Science and Technology

Department of Physics and Technology

Determination of the Dielectric Properties of Marine Surface Slicks Using Synthetic Aperture Radar

Cornelius Quigley

A dissertation for the degree of Philosophiae Doctor - January 2021

Abstract

Over the course of the last three decades, Synthetic Aperture Radar (SAR) has proven itself to be an effective monitoring technology for marine applications. The clear benefits of using SAR as opposed to optical devices is that SAR is insensitive to cloud cover, lighting conditions and can also provide imagery to a high degree of resolution. Given these benefits, there is a large incentive to implement SAR as a primary detection mechanism for marine oil spills due to the fact that SAR is capable of reliably providing data on a semi-daily basis. With increasing levels of maritime traffic due to declines in Arctic multiyear sea ice as well as risks associated with oil and gas exploration in the Arctic, being able to derive important geophysical information on the state of an oil slick is important for the decision-making process of first responders and clean-up personnel. This thesis is concerned with attempting to determine the dielectric properties of oil slick using SAR. The dielectric constant is a proxy for the volumetric water/oil content within an oil slick. This is due to the fact that when pure crude oil is inserted to the marine environment, it becomes subjected to a host of processes collectively referred to as weathering. Throughout these processes, oil-in-water emulsions can form that alter the dielectric properties of an oil slick resulting in a substance that has a dielectric value between that of pure crude oil and pure sea water depending on the volume of sea water present within an emulsion. In this thesis, we first apply a two-scale theoretical backscattering model to quad-polarimetric Radarsat-2 data of verified oil slick acquired during oil-on-water exercises conducted in the North Sea between the years of 2011-2013, acquired under varying wind conditions and incidence angles. The results showed realistic values for the dielectric constant given auxiliary information on the state of the slicks. However, no in-situ information was available to verify the model. A unique set of data was then acquired during the NORSE2019 oil-on-water experiment by DLRs F-SAR instrument in full quad-polarimetric X-, S- and L-bands. This data set was used to verify the model approach used in this thesis as well as to investigate the time variability of the discharged slicks using a stability measure in conjunction with a novel polarimetric feature that exploits the multifrequency aspect of the data set. The work presented in this thesis sheds light on the on-going discussion on the use of SAR for marine slick characterization.

Acknowledgements

The great English poet John Donne delivered a sermon in St. Pauls Cathedral in 1624 beginning with the words, 'No man is an island entire of itself…'. The sermon was ment to be a lesson on the nature of human connectedness and how important connection is for the well-being and survival of any individual. This is especially true when facing the rigors of academia. The following is my testament to the exceptional people I was privileged to meet during my time in CIRFA and who were always willing to help me when required.

Firstly, an enormous debt of gratitude must be paid to my two supervisors, Camilla Brekke and Torbjørn Eltoft. Over the course of the last three years they have afforded me a great deal of their time, energy and support. This came in the form of allowing me to attend conferences and summer schools in exotic locations, constantly offering me feedback on all manuscripts I produced, as well as offering suggestions whenever I hit a brick wall in the research. Most importantly though, they showed a great degree of patience with me and thus created a fantastic learning atmosphere. I am immensely grateful for these wonderful opportunities they have afforded me. I hope one day I can return the favor.

I must also acknowledge Veronique Miegebielle and Robert Bridges from Total, our industrial partner, who provided the funding for this thesis. I was very impressed by their level of support and by the degree to which they wished to be involved in my work. I greatly enjoyed our meet-ups in Tromsø and Paris and I sincerely hope that I may have the pleasure of working with them again.

My old Masters thesis supervisor, Anthony Doulgeris, needs to be thanked as well. I am very grateful for his attentiveness in trying to help me with any issues I had, particularly in relation to anything related to Matlab and programming. Likewise, our resident 'computer whisperer' Thomas Kræmer deserves immense praise. I have never been more impressed by a persons working knowledge of anything computer related than him.

Martine Espeseth, a fellow PhD student and later Postdoc here in CIRFA, has helped me out on numerous occasions and was always willing to lend me her ear and to act as a sounding board for any ideas I had. While she is now working with Kongsberg Satellite Services, another one of our industrial partners, I hope our future collaborations will prove to be just as fruitful.

Fellow PhD students and Postdocs in CIRFA who have helped me out on a variety of topics whenever I happened to knock on their doors include Malin Johansson, Johannes Lohse and Jakon Grahn. Their kindness was greatly appreciated.

I would also like to thank Geir Antonsen who works in the administration side of the Physics Department for his help in any non-physics related issues. In addition, I would like to thank our project coordinator Andrea Schneider for all the help and assistance she has given me.

I came to Tromsø in January 2015 to simply do a Masters degree, but have received much more than I deserved. I am eternally grateful to all who are listed here and it is my hope that I may return the kindness I have received.

Cornelius Quigley
Tromsø, January 2021

Contents

List of Figures

List of Tables

List of Abbreviations

AIRSAR	Airborne Synthetic Aperture Radar
A-PTSM	Anisotropic Polarimetric Two-Scale Model
BAOAC	Bonn Agreement Oil Appearance Code
CIRFA	Centre for Integrated Remote Sensing and Forecasting for Arctic Operations
DLR	Deutsches Zentrum für Luft- und Raumfahrt
DWH	Deepwater Horizon
EM	Electromagnetic
ESA	European Space Agency
fBm	fractional Brownian motion process
F-SAR	Large-scale airborne SAR facility
IFO	Intermediate Fuel Oil
IR	Infrared
NCA	Norwegian Coastal Administration
NESZ	Noise-Equivalent-Sigma-Zero
NOFO	Norwegian Clean Seas Association for Operating Companies
NORSE2019	Norwegian Radar Oil Experiment 2019
NSR	Northern Sea Route
PSD	Power Spectral Density
PTSM	Polarimetric Two-Scale Model
PRF	Pulse Repetition Frequency
RAR	Real Aperture Radar
RMS	Root Mean Square
SL	Stability Level
SNR	Signal-to-Noise Ratio
SPM	Small Perturbation Model
UAVSAR	Uninhabited Aerial Vehicle Synthetic Aperture Radar
WTO	World Trade Organization

Nomenclature

a, b	Facet slopes in azimuth and range directions respectively
B	Bandwidth of transmitted pulse
$C_{k,n-k}^{pq}$	Series expansion coefficients
$C_{2way,el}(v)$	Two-way antenna pattern in elevation
$C_{2way,az}(\phi_i)$	Two-way azimuth antenna pattern as a function of azimuth angle
c_0	Speed of light
D	Fractal dimension
D_A	Antenna length
D_R	Antenna width
E_x	X component of Jones vector
E_y	Y component of Jones vector
$\boldsymbol{E}$	Jones vector
e	Eulers number
F	Handedness of a polarized wave
f	Frequency of radiation
G_R	Antenna gain in reception
G_T	Antenna gain in transmission
H	Horizontal polarization
H_t	Hurst coefficient
h	Height of the sensor above the ground
$h_{surface}$	Small-scale roughness variance
I_0	Measure of the total amount of energy contained in a wave
k	Wave number
L	Synthetic aperture length
L_p	Profile length
m_s	Backscatter amplitude
N	Number of points in a profile
N_{az}	Number of integrated pulses during the azimuth compression
P_{av}	Average transmit power
P_n	Equivalent receiver noise power
$P(\beta)$	Distribution of angles the Bragg coherency matrix is rotated in the XBragg model
Q	Measure of a waves polarization tendency to be more vertical
R	Slant range
R_{co-pol}	Co-polarization ratio
R_p	Bragg scattering coefficient parallel to the plane of incidence
R_s	Bragg scattering coefficient perpendicular to the plane of incidence
$\mathbf{S}$	Scattering matrix
S_0	Quantity related to the roughness variance
S_{0_n}	Facet-size-dependent constant
S_{pq}	

	Complex elements of the scattering matrix that describe the phase and amplitude of the p-transmit and q-receive wave
s	Standard deviation of the surface facet slopes in the PTSM
s_h	Standard deviation of the surface height
s_{rms}	Root mean square height
$\boldsymbol{T}$	Coherency matrix
U	Expresses the tendency of a wave to be polarized at ±45º
V	Vertical polarization
v	Beam steering angle
vol	Oil content in terms of volume of an oil-water mixture
W	Power spectral density of the small-scale roughness
y_i	Height of the surface profile at a point number i
Z	Platform velocity
$z(\mathbf{r})$	Surfaces stochastic corrugations at a point **r**
α	An empirical parameter which describes the distribution of relaxation times
β	Angle the Bragg coherency matrix is rotated in XBragg model
β_1	Width of distribution $P(\beta)$
Γ^0	Fresnel reflectivity coefficient at nadir
Γ_h	Fresnel coefficient for the horizontal component of the radiation
Γ_v	Fresnel coefficient for the vertical component of the radiation
δ	phase difference between the vertical and horizontal components of the wave
δ_{az}	Azimuth resolution of the sensor
δ_{ground_range}	Ground range resolution of a SAR
δ_p	Penetration depth of incident wave
δx	Shift distance
ε	Complex dielectric constant
ε_{eff}	Effective complex dielectric constant of a water oil mixture
ε_{oil}	Complex dielectric constant of pure crude oil
ε_s	Static dielectric constant
ε_w	Complex dielectric constant of pure sea water
ε_0	Permittivity of free space
ε_∞	Dielectric constant of infinite frequency
η	Local incidence angle corresponding to the signal;
θ	Incidence angle
θ'	Angle of transmission into a medium
θ_l	Local incidence angle
λ	Wavelength of the sensing radiation
μ	Magnetic permeability
σ^0	Backscattering coefficient
σ^0_{VV}	Backscattering coefficient in VV polarimetric channel
σ	Ionic conductivity
τ_r	Relaxation time
ϕ	Azimuth angle
ω	Angular frequency

1 Introduction

1.1 Motivation

Throughout the latter half of the 20th century up, specifically after the end of the second world war until the present point in time, the world has seen an unprecedented rise in trade between nations as a consequence of globalism and emerging markets being able to offer products and services overseas. A clear manifestation of the global community's commitment to peaceful trade among nations occurred in 1 January 1995 when the World Trade Organization (WTO) officially convened for the first time for the purposes of moderating trade among nations, specifically in regards to the regulation of tariffs across international borders. Current studies have shown that with the presence of the WTO, international trade has increased, and that barriers to trade would be more significant without the organization [WTO, 2015].

As a result of the increase in nations trading, the number of ships traveling on the open seas has increased. According to a UN report [UNCTAD, 2019], between the years of 1980 and 2018 the amount of cargo being transported went from just under 4 billion tons to just under 12 billion tons per year. The same report also predicts that between the years of 2019 to 2024, international maritime trade will expand at an average annual growth rate of 3.5%. According to [Carpenter, 2015], in Europe alone, 22,752 merchant ships operated in European waters in the year of 2008, resulting in over 694,500 movements into ports.

This poses a particular problem to the global maritime ecosystem. According to [Alpers et al., 2017], most of the anthropogenic oil pollution encountered at sea does not originate from ship or oil rig accidents, but is a result of routine ship operations like tank washing and engine effluent discharges (sludge). It is estimated that at least 3000 illegal mineral oil incidents occur within European waters alone each year, amounting to between 15,000 to 60,000 tons of mineral oil being discharged illegally in the North Sea each year alone [Carpenter, 2015].

This has profound consequences for the Arctic. According to [Ho, 2009], due to the effects of climate change, an ice-free Arctic, during the summer months, is expected by the mid-century. This is supported by [Galley et al., 2016] who states that between 1979 and 2015 the mean September Arctic sea ice extent decreased by 13.4% per decade. The authors of this study also report that, in addition to this, thicker multiyear ice that inhabits the Arctic, is being replaced by thinner first year ice, due to the fact that sea ice that grows is showing a trend of not surviving one melt season. This change in the composition of Arctic sea ice, due to the onset of climate change, is providing opportunities for maritime transit and exploration. One notable aspect of the longer melt season is the opening up of the Northern Sea Route (NSR). In 2009 two merchant ships were able to transit the NSR for the first time departing from Ulsan in South Korea and sailing to Rotterdam in the Netherlands bypassing the Suez Canal and the strait of Malacca, thus saving fuel and money in operating costs [Ho, 2009].

Given that the Arctic sea ice extent, as of 2017, was 13.83 million square kilometers [NSIDC, nd], a vast area is expected to open up for human exploitation. This will offer the possibility for more efficient exploitation of natural resources, like oil and gas, and thus increasing the possibility of major spill events occurring in the high north.

According to [Coleman, 2003] when spill events occur, they may have acute effects that may be of short-term and of limited impact or can have long-term population or community level

impacts, which will depend on the timing and duration of a spill. It is generally agreed that mineral oil can kill micro-organisms and reduce their fitness through sublethal effects [Coleman, 2003] and can have disastrous consequences for ecologically sensitive wetlands, coral reefs and fishing grounds. Heavily oiled birds can also die from hypothermia or from a loss of buoyancy. Marine animals can also die from hypothermia or become easy prey. Oil spills in coastal waters can also directly have negative impacts on local economies which depend on industries such as fishing, boating or tourism [Caruso, 2013]. While these effects are well understood from laboratory studies, the long-term, more subtle effects of exposure to mineral oil on the marine ecosystem are not yet well understood, and are difficult to study for ethical reasons [Coleman, 2003].

Given, the immediate threats oil spill events can have on the economic interests of a state or region, continued surveillance is required to enforce legislation in regards to ethical industrial practices and to respond efficiently to such events. Given that the Arctic is remote, prone to cloud cover and experiences darkness for much of the year, spaceborne Synthetic Aperture Radar (SAR) has proven itself to be an effective surveillance technology for these purposes. Currently there is a large international effort to develop methodologies that rely solely on SAR that can determine key physical features of an oil spill, to aid the response of first responders. These are namely the extent of a discharge, determination of the physical distribution of oil on the sea surface in relation to the location of zones of variable thickness and oil concentration within slick, rates of spreading and transport, and the volumetric amount of oil spilled [ITOPF, 2011 (a)].

An example of the central role SAR has played in a major oil spill event in recent years occurred during the destruction of the Deepwater Horizon platform in the Gulf of Mexico on 20 April 2010. Throughout the incident, SAR imagery was used to establish the extent of the spill as well as its trajectory. According to [Caruso, 2013], between the period of 23 April and 15 July 2010, when the well was successfully sealed, more than 700 satellite passes, amounting to roughly 1400 scenes spanning the Gulf of Mexico to the Florida Straits were analyzed and delivered to responders.

The need for emergency preparedness in Norwegian waters is high due to the high volume of oil production that occurs. Norway has suffered a number of oil spill events due to offshore industrial petroleum activities. This includes an explosion at the EKOFISK oil field in 1977 which resulted in an estimated 20,000 tons of oil being discharged into the sea. There have also been numerous ship accidents that resulted in spill events. This includes the bulk carrier the MV SERVER which ran aground approximately 30 nautical miles north of Bergen in 2007 which resulted in approximately 375 tons of Intermediate Fuel Oil (IFO) 180 being discharged. In 2009 the bulk carrier FULL CITY grounded in Langesund, south of Oslo, which subsequently contaminated approximately 100 km of shoreline. The container ship GODAFOSS ran aground in southern Norway in 2011, 10 km from the Swedish border, resulting in 120 tons of IFO 380 being discharged into the sea and resulting in an estimated 500 sea birds being oiled [ITOPF, 2018].

The work presented in this thesis is funded by the Centre for Integrated Remote Sensing and Forecasting for Arctic Operations (CIRFA) in partnership with Total E&P Norge AS. This thesis concerns itself with the remote sensing of surface dwelling mineral oil slicks via the use of SAR. Specifically, the goal of this thesis is to develop methodologies that will allow a user to determine the absolute value of the complex permittivity $|\varepsilon|$ of oil slick. This quantity is

dependent on the volumetric content of water in oil and can act as a proxy for the concentration of oil within slick. This will be explained in greater detail in Chapter 3.

The work presented in this thesis was conducted with the aim of offering a possible way to characterize oil slick when spill events occur for the purposes of directing clean-up and recovery efforts. In Norway, the organization that is responsible for the emergency response to acute pollution due to ship related spill events is the Norwegian Coastal Administration (NCA) while the Norwegian Clean Seas Association for Operating Companies (NOFO) directs clean-up efforts related to oil and gas production. These departments are responsible for preventing and identifying acute pollution and ensuring that the responsible parties or local municipality implements the necessary response measures. As part of their response measures, they make use of spaceborne radar satellites operated by Kongsberg Satellite Services (a CIRFA partner) to provide information on substantial oil spills within 2 hours of a satellite overpass.

The main contributions of the work presented in this thesis are as follows:

- A methodology for determining $|\varepsilon|$ within a SAR scene is developed. The main emphases is on the development of a procedure to be applied to spaceborne SAR data, i.e. for the case when only the co-polarization channels are available (Paper 1).

- The viability of this inversion method (i.e. retrieving values of $|\varepsilon|$ using only the co-polarization ratio which is referred to as Method 1 in Paper 2) is then tested against inversion results obtained when the full suite of polarimetric information is utilized (i.e. retrieving values of $|\varepsilon|$ using both the co- and cross-polarization ratios which is referred to as Method 2 in Paper 2). To do this, a unique data set of airborne SAR data, which was acquired in X-, S- and L-bands, and which have relatively favourable noise characteristics, was used. The results found that both methods were correlated for low dielectric values, i.e. the areas of a slick with the highest concentration of oil (Paper 2).

- The potential for determining areas with a higher concentration oil within slick using multifrequency airborne SAR, as well as investigating the potential of exploiting the temporal aspect of a time series of such multifrequency SAR acquisitions was investigated. This is achieved via the implementation of a new feature we call the *incidence angle normalized sum of co-polarization ratios.* This feature simultaneously removes the incidence angle dependence inherent to SAR data (specifically in the co-polarization ratio) and combines the result in multiple frequency bands. This feature was then fed into a stability level algorithm. Zones within slick that were consistently stable over the length of time the time series was acquired were determined (Paper 3).

1.2 Thesis Outline

- **Part I chapters 2-5:**

Chapter 2 will introduce the reader to the SAR instrument. Several key characteristics of this type of sensor will be highlighted that are directly relevant to the research presented in this thesis. The most relevant aspects for the reader will be a discussion on the noise characteristics of SAR as well as a brief discussion on the differences between airborne versus spaceborne SAR. More fundamental information relating to the instrument is also presented, to provide a brief, yet rounded introduction to SAR for the reader.

Chapter 3 will provide the reader with a brief summary on the physics underpinning the dielectric constant as well as providing an explanation on the role surface roughness plays in scattering problems. This chapter will conclude with a brief review of various common surface scattering models that can be found in the literature.

Chapter 4 will outline some important concepts relating to the remote sensing of oil slicks that will be encountered in the papers to follow. This chapter will begin with a brief overview of the various anthropogenic pollutants that can be encountered in the marine environment as well as the numerous phenomena that can appear similar to oil within SAR imagery. A key aspect of the information contained in this chapter is to provide the reader with a sense of the difficulty in engaging in the field of oil spill remote sensing, as well as to highlight the challenges the field can face due to the existance of look-alike phenomena.

Chapter 5 contains a short summary of the publications that are included in this thesis.

- **Part II chapter 6-8:**

These chapters contain the publications that contain the research components of this thesis.

- **Part III chapter 9:**

A discussion on the research presented in the three papers is included as well as directions for future research.

2 Remote Sensing via SAR

The following chapter is designed to provide the reader with a basic insight into the SAR technique. Each SAR sensor will have different design considerations based their mission objectives but the underlying operational principles are the same. An in-depth review is beyond the scope of this thesis but the interested reader is referred to [Elachi and van Zyl, 2006] and [van Zyl and Kim, 2010] for a more thorough treatment.

2.1 Basic Overview of SAR

SAR is a side-looking imaging radar that can be mounted on a moving platform, usually a spaceborne satellite or an aircraft. A SAR antenna is rectangular in shape and has dimensions of 10 m – 15 m × 1 m approximately (15 m × 1.37 m for the case of Radarsat-2 [Canadian Space Agency, nd]). The longest side of the antenna is aligned with the ground track of the orbit with the radar beam emanating from the side of the platform. The result is a two-dimensional image. The dimension of the image that runs across the track is referred to as the range direction and the dimension of the image that runs along the track is referred to as the azimuth direction.

2.2 SAR Geometry

Figure 2.1 shows the sensing configuration of a side-looking radar, such as a real aperture radar (RAR) or SAR. The sensor is placed on a moving platform, usually a satellite or an aircraft and records the backscattered radiation from a footprint area which is later processed to form a 2D SAR image. The radar measures distances in the range direction in the radial line of sight (slant range). The ground range distance is the true horizontal distance on the ground which corresponds to each point measured in the slant range [Brekke, 2008].

Sensors of this kind retrieve measurements of the reflectivity of a scattering surface, also referred to as the backscattering coefficient σ^0 and provide information about the physical composition of the scatterers. In other words, each pixel of a SAR image represents a measurement, and so is interpretable based on underlying physical processes. It should be noted that σ^0 is a fraction that describes the amount of average backscattered energy compared to the energy of the incident field [Barrett et al.,2009].

The sensor travels in the azimuth direction with the side-looking antenna pointing, and transmitting electromagnetic (EM) pulses, in the slant range direction. The amount of surface that is imaged is indicated by the swath width of the antenna.

2.3 Spatial Resolution

The term spatial resolution provides an indication of the minimum distance between two points on a surface that can be separated. The following subsection will outline the two types of spatial resolution that can be encountered within SAR imagery, the first being in the range direction, i.e. ground and slant range resolution, and the second being in the azimuth direction, i.e. azimuth resolution. The following explanation for these two concepts can be found in [Elachi and van Zyl, 2006].

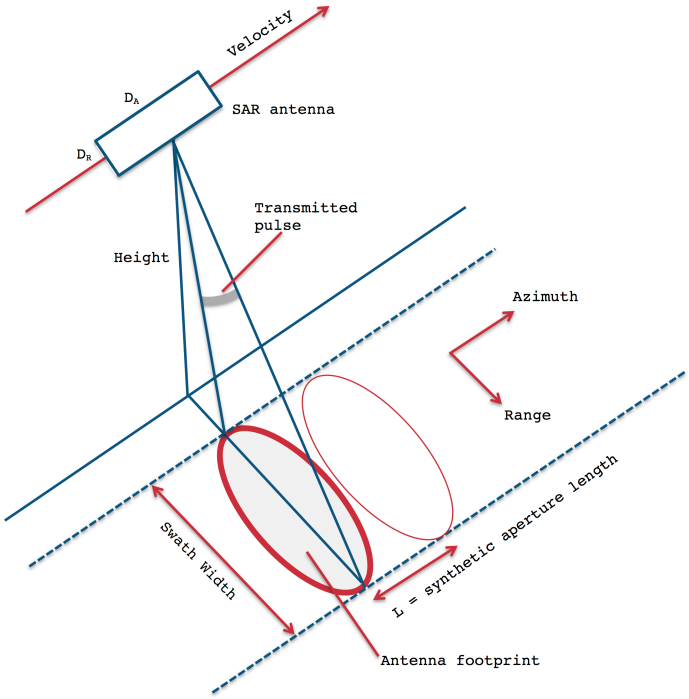

Figure 2.1: A basic overview of SAR geometry. Taken from Figure 2.1 in [Espeseth, 2019] which was adapted from [Curlander and McDonough, 1991]. As can be seen D_A and D_R represent the length and width of the antenna respectively.

2.3.1 Resolution in the Range Direction

The ground range resolution of a SAR is defined as

$$\delta_{ground\_range} = \frac{c_0}{2Bsin\theta} \tag{2.1}$$

where c_0 is the speed of light, B is the pulse bandwidth and θ is the incidence angle. A finer ground range resolution can be achieved by using a shorter pulse length. This can only be achieved within specific engineering design considerations however, so the SAR range resolution depends instead on the type of pulse coding and the method in which the return from each pulse is processed. Explicitly stated, frequency modulated chirp pulses with a large pulse bandwidth B is applied in order to achieve a high degree of spatial resolution. For more information on the technical aspects of the SAR system signal processing the reader is directed to [Curlander and McDonough, 1991].

2.3.2 Resolution in the Azimuth Direction

The azimuth resolution of a real aperture radar (RAR) is defined as

$$\delta_{az} = \frac{h\lambda}{D_A cos(\theta)} \tag{2.2}$$

Where h is the height of the sensor above the ground, λ is the wavelength of the sensing radiation and D_A is the length of the antenna in azimuth direction. The azimuth resolution is inversely proportional to the length of the antenna which indicates that a finer resolution can be achieved with a longer antenna. In the case of SAR, the fine resolution that is achieved is a result of synthesizing a larger antenna. This is achieved by having the SAR sensor in motion while transmitting the pulses. After applying signal processing techniques using the Doppler

and phase history of the backscattered pulses, the azimuth resolution of the SAR sensor becomes

$$\delta_{az} = \frac{D_A}{2} \tag{2.3}$$

As can be seen from this equation, a smaller antenna can result in a finer resolution.

2.4 Frequency and Polarization

The frequency of the sensing radiation is an important factor for Earth Observation purposes as it determines the scale in which EM waves will interact with a target. For this reason, the choice of frequency that is employed is largely determined by the nature of the SAR mission at hand.

Table 2.1 shows various frequency bands that are commonly employed for SAR remote sensing. The frequency bands that are explored in this thesis are X-, C-, S- and L-bands. It should be noted that for spaceborne SAR, the highest frequency band that is employed is X-band, as Ka- and Ku-bands tend to be attenuated by the atmosphere due to their short wavelength.

The polarization of an EM can be thought of as the locus that the tip of the electric field would trace over time at a fixed point in space [van Zyl and Kim, 2010]. SAR sensors are generally designed to transmit EM radiation either vertically polarized (V) or horizontally polarized (H) with the antenna also designed to receive backscattered energy in horizontally polarized or vertically polarized configurations. For the case of quad-polarimetric SAR, the antenna can simultaneously transmit and receive radiation in both H and V polarizations. This indicates that we can have four polarization combinations, HH, HV, VH and VV, where the first letter indicates the polarization of the transmit radiation and the second letter indicates the polarization of the received radiation. Given that various objects modify the degree of polarization differently, the four "polarimetric channels" can indicate complimentary information on the nature and state of a scattering target.

Table 2.1: Microwave frequency bands [Chuvieco and Huete, 2010].

Frequency band	**Ka**	**Ku**	**X**	**C**	**S**	**L**	**P**
Frequency [GHz]	40-25	17.6-12	12-7.5	7.5-3.75	3.75-2	2-1	0.5-0.25
Wavelength [cm]	0.75-1.2	1.7-2.5	2.5-4	4-8	8-15	15-30	60-120

2.5 Stokes Vector and the Scattering Matrix

In order to mathematically describe a polarized wave, we can use two components of the electric field vector, E_x and E_y, which can be combined to represent the Jones vector

$$\boldsymbol{E} = \begin{pmatrix} E_x \\ E_y \end{pmatrix} \tag{2.4}$$

However, it is not always possible to measure the components of the electric field vector directly [Woodhouse, 2006]. In the early days of polarimetric research, the polarization of an EM wave vector was determined via more deductive approaches where the intensity of a wave was measured after it passed through a linear polarizing filter that was orientated at certain angles.

In 1852 the Irish physicist George Gabriel Stokes introduced four specific parameters that allow for a complete description of a polarized wave based on optical experiments. These four parameters are usually represented in a vector format for the purposes of making them easier to work with. This Stokes vector is composed of the four terms I_0, Q, U and F. The first term, I_0, is a measure of the total amount of energy contained in a wave which does not say anything about the polarization of a wave and is given by

$$I_0 = \langle E_y^2 + E_x^2 \rangle = \langle E_y^2 \rangle + \langle E_x^2 \rangle \tag{2.5}$$

The brackets $\langle ... \rangle$ denote an averaging operation over time which is required when the wave is not completely polarized. The other three terms describe the state of polarization.

$$Q = \langle E_y^2 \rangle - \langle E_x^2 \rangle \tag{2.6}$$

is a measure of a waves polarization tendency to be more vertical i.e. $Q > 0$, or horizontal $Q < 0$. The third and fourth terms jointly represent the phase difference, δ, between the vertical and horizontal components of the wave. Here, the third term is given as

$$U = 2E_y E_x cos\delta = 2ReE_y E_x^* \tag{2.7}$$

and expresses the tendency of a wave to be polarized at ±45°, i.e. $U > 0$ for 45° or $U < 0$ for -45°. The superscript * denote the complex conjugate of a number here.

The handedness of the wave is described by the fourth term and is given by

$$F = 2E_y E_x sin\delta = 2ImE_y E_x^* \tag{2.8}$$

Where $F > 0$ implies left-handedness polarizations and $F < 0$ implies right-handedness polarizations.

When working with SAR sensors, the Stokes vector is not the most effective way of characterizing data as there are two measurements of polarization to quantify, one for each of the orthogonal transmitted pulses, which means that two Stokes vectors would be required. In order to effectively characterize the data that is measured by a SAR, the scattering matrix has proven to be useful. The advantage of this matrix is that it describes the relationship between incident and scattered wave fields where

$$\begin{pmatrix} E_v^s \\ E_h^s \end{pmatrix} = \begin{pmatrix} S_{VV} & S_{VH} \\ S_{HV} & S_{HH} \end{pmatrix} \begin{pmatrix} E_v^i \\ E_h^i \end{pmatrix} \tag{2.9}$$

Where each of the elements S_{pq} are complex numbers that describe the phase and amplitude of the p-transmit and q-receive wave. When the subscripts are the same, the measurement is

referred to as co-polarized and when they are different the measurement is referred to as cross-polarized. In general, p and q can be any pair of orthogonal polarizations, i.e. R and L circular [Woodhouse, 2006]. Any radar system that measures the phase and amplitude of these four terms is described as *fully polarimetric*. In contrast, any system that measures only a subset of these is referred to as *partially polarimetric* (commonly referred to as *single* or *dual polarimetric SAR* depending on the receiving capabilities of the instrument).

In terms of Earth observation applications, the principle of reciprocity is usually implied which states that $S_{VH} = S_{HV}$. This is a practical convenience as these polarimetric channels will contain signal of lower intensity than the co-polarization channels and will be influenced more by internal system noise or other factors [Woodhouse, 2006].

It should be noted that the Stokes vector provides the polarimetric state of an EM wave while the scattering matric indicates the targets ability to transform the state of the EM wave in the scattering process.

2.6 Sources of Noise within SAR Imagery

There are many various forms of noise artifacts that can be encountered within SAR imagery. Such artifacts include cross-talk and channel imbalance, aliasing, effects from sidelobes and quantization degradation. A discussion on these artifacts is beyond the scope of this thesis but further information can be found in [Espeseth, 2019]. In this section the two forms of noise that are relevant for this thesis will be discussed, i.e. the inclusion of speckle in SAR imagery and thermal noise.

2.6.1 Speckle

One common aspect of SAR imagery is the presence of speckle, also referred to as salt and pepper noise. This is a result of constructive and destructive interference between backscattered waves from within individual resolution cells [Lee and Pottier, 2009]. Its presence is a direct

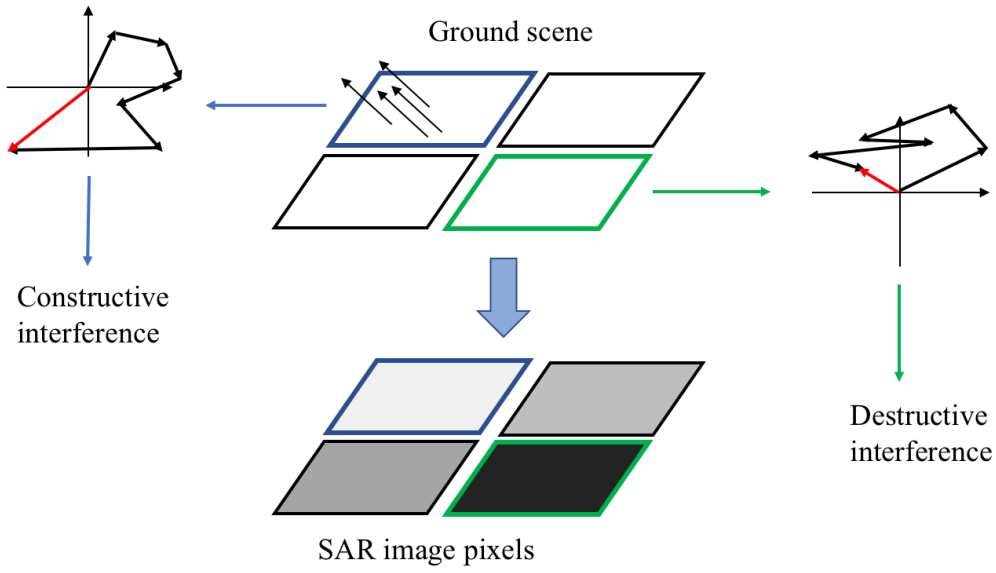

Figure 2.2: Demonstration of how speckle occurs within a SAR image. Phases of the radiation fronts can interfere constructively of destructively resulting in darker or brighter pixels within a scene.

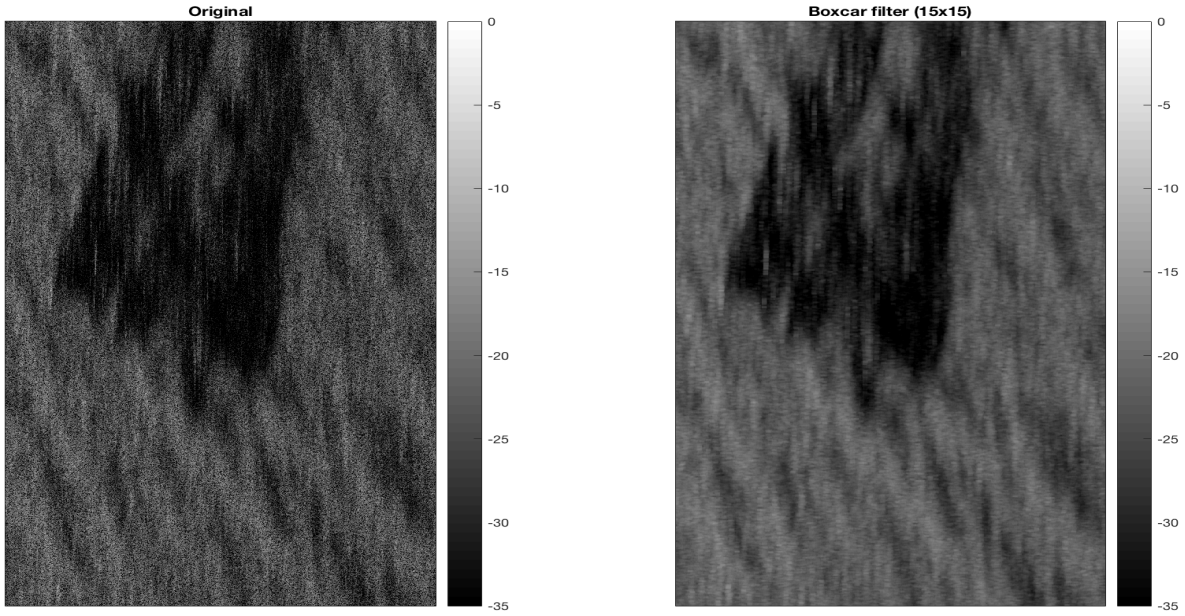

Figure 2.3: σ^0_{VV} images of an oil spill from the NORSE2019 oil-on-water experiment. Left: S-band F-SAR acquisition of mineral oil slick taken during the NORSE2019 oil-on-water experiment in the North Sea as seen before before multilook averaging was performed. The speckle pattern is apparent over the ocean areas. Right: Scene after multilook averaging is applied. The F-SAR data and Products

result of the fact that SAR systems are monochromatic. It is a multiplicative phenomenon, meaning that the amount of speckle present increases with the average intensity. It should be noted that while the presence of speckle is disruptive it is not strictly speaking a type of noise but rather a characteristic of the measurement made.

Figure 2.2 shows a typical setup where radiation that is incident upon the ground is being backscattered towards the SAR. The individual scatterers within each resolution cell result in radiation waves with different phases. The waves interfere either constructively or destructively resulting in a SAR image with pixels of varying brightness.

Figure 2.3 illustrates this concept on one of DLRs Large-scale airborne SAR facility (F-SAR) scene containing mineral oil emulsion taken from the NORSE2019 oil-on-water experiment. As can be seen, the panel to the left shows the scene before multilooking averaging is performed, while the panel to the right shows the scene after multilooking averaging is performed. The grainy appearance of the speckle is apparent before multilooking is performed.

2.6.2 Additive Noise

Additive noise is generally found within all SAR imagery and is unavoidable. The components of additive noise are thermal noise which arises as a result of the operation of the sensor and in some cases quantum degradation. This additive power is contained within the Noise Equivalent Sigma Zero (NESZ) and is defined as the value for which the backscatter coefficient has an equal strength to the background noise [Espeseth, 2019, and references therein].

According to [Younis et al., 2009] the NESZ is a measure of the sensitivity of the radar to low areas of backscatter and corresponds to the value of the backscatter coefficient that corresponds to a SNR of 1. The NESZ is a function of the slant range *R* and is given by

$$NESZ(R) = \frac{2(4\pi)^3 P_n \cdot PRF}{c_0 \lambda^2 P_{av} G_T G_R} \frac{N_{az} sin(\eta)}{\delta_{az}} \frac{1}{\left| C_{2way,el}(v) \cdot \Sigma_{i=1}^{N_{az}} \left(C_{2way,az}(\phi_i) / R^2(\phi_i, v) \right) \right|^2} \quad (2.10)$$

where P_n represents the equivalent receiver noise power; P_{av} is the average transmit power; G_T, G_R are the antenna gain in transmission and reception, respectively; λ is the radar wavelength; c_0 the speed of light; δ_{az} is the azimuth resolution; $N_{az} = \lambda R \cdot PRF / 2\delta_{az} \cdot Z$ is the number of integrated pulses during the azimuth compression, where PRF indicates the pulse repetition frequency and Z is the platform velocity. η is the local incidence angle corresponding to the signal; v is the beam steering angle; ϕ the azimuth angle. $C_{2way,el}(v)$ represents the two-way antenna pattern in elevation and $C_{2way,az}(\phi_i)$ is the two-way azimuth antenna pattern as a function of azimuth angle.

As can be seen in Figure 2.4 the NESZ varies as a function of slant range primarily due to the antenna elevation pattern. A notable aspect of the NESZ, as can be seen in this image, is that it can vary depending on the sensor that is used, the sensing mode employed and even the sensing radiation that is utilized. This image shows the NESZ curves for the two sensors that are pertinent to this thesis, i.e. Radarsat-2 and F-SAR. As can be seen, the airbourne F-SAR instrument provides lower noise floor (another name for NESZ) values than the spacebourne SAR instrument making it ideal for experimentation.

As can be seen in (2.10), the NESZ is inversely proportional to the wavelength of the sensing radiation. This indicates that SARs that operate with shorter wavelength should exhibit noiser characteristics than SARs that operate at longer wavelengths. This can be seen in Figure 2.4 below.

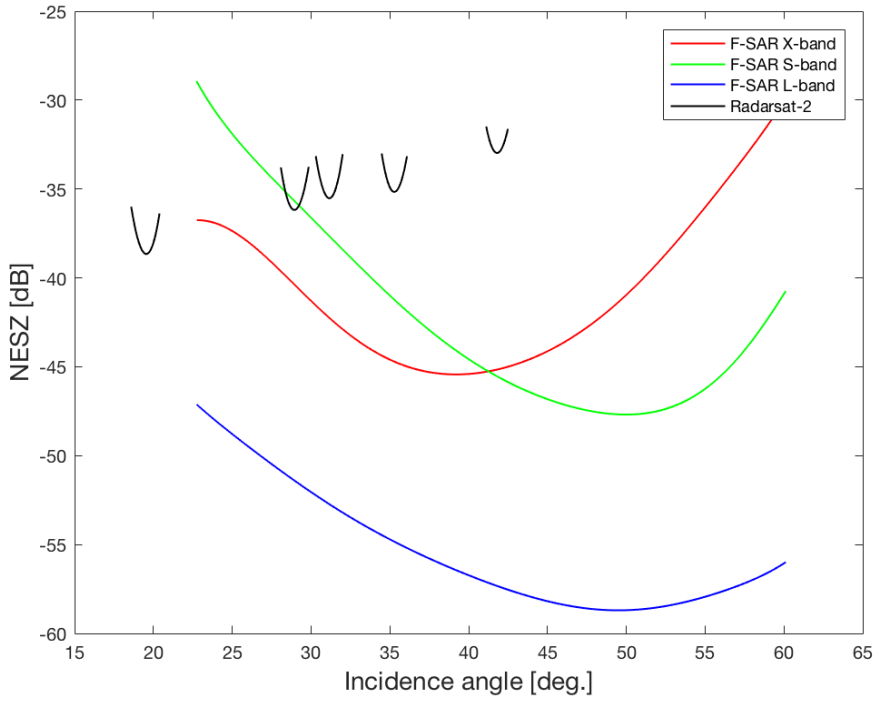

Figure 2.4: NESZ curves vs. incidence angle for F-SARs X-, S- and L-band sensors. NESZ curves for various Radarsat-2 (C-band) acquisitions are also shown.

One conclusion that can be drawn from Figure 2.4 is that while a trend can be seen in the NESZ curves for the F-SAR instrument, the NESZ curves for Radarsat-2 have higher average values despite the fact that it is a C-band sensor.

2.7 Airborne vs. spaceborne SAR

As already stated, an imaging radar may be carried on either an airborne or spaceborne platform. There are generally benefits and downsides to the use of both platforms. As already illustrated in section 2.3, the advantage of SAR is that the spatial resolution of the sensor is independent of platform altitude meaning that a high degree of resolution can be achieved from both platforms.

Despite this, the viewing geometry and swath coverage can be significantly influenced by the altitude of the sensor. If a SAR is mounted on an airplane, the radar must cover a wide range of incidence angles in order to achieve a large swath width. Since it is well known that the incidence angle affects the amount of backscatter returned to the sensor, the appearance of features in an image will be affected.

Spaceborne SARs are able to mitigate these imaging problems as they operate at altitudes significantly higher than airborne radars. At the altitude that spaceborne radars operate, imagery spanning the same swath widths with much narrower range of incidence angles can be achieved providing more uniform illumination. These effects however are not as relevant for ocean remote sensing.

Despite this, airborne radar systems can be more flexible in their ability to collect data from various look directions and angles. As well as this, an airborne instrument has the ability to be deployed at will, as long as flying conditions permit. Spaceborne instruments are not subject to this degree of flexibility as their data acquisition schedule and viewing geometry is controlled by the orbit it inhabits. Despite this, satellite borne SARs have the advantage of being able to collect data faster over larger areas and provide more consistent viewing geometry.

3 Surface Scattering and Scattering Models

There are a number of factors which can affect the backscatter to the SAR which can be broadly split into two categories. The first relates to the sensor characteristics. These are the frequency of the radiation, the polarization of the radiation as well as the incidence angle of the incoming radiation. The second category relates to the physical characteristics of the scattering medium. For the case of marine remote sensing, these are the surface geometry, i.e. surface roughness of the scattering medium, as well as its dielectric constant. These two factors will be discussed in the upcoming subsections. It should be noted that the dielectric properties of a material are frequency dependent. The associated mathematics are outside the scope of these thesis, but a qualitative explanation for this frequency dependence aspect is included. A brief overview of some common surface scattering models that are commonly cited in the literature are also included in later subsections. In order to set up what will come in later sub-sections the first subsection in this chapter will provide a brief historical perspective on the surface scattering problem.

3.1 A Brief Historical Perspective on the Surface Scattering Problem

During the World War II, radar was developed for the purpose of detecting enemy aircraft [Plant, 1990]. When this newly developed tool was put to use for detecting targets on or near the ocean surface, targets were often obscured by strong echos from the ocean itself. This 'sea echo' was a considerable nuisance to those engaged in the war effort, so research was commissioned to try to determine the nature of this unwanted return [Plant, 1990].

Early theoretical work attempted to try to explain the echo in terms of return from the sea itself, or from the spray and bubbles residing on the surface. Specular reflection was found to reliably explain the characteristics of sea echo for small incidence angles but not for larger ones [Plant, 1990]. The standard approach at first focused on applying the 'Kirchoff principle' which assumed that the surface is smooth in the sense that the radius of curvature is larger compared to the EM wavelength. However, this method was unable to account for the observation that vertically polarized return was generally stronger than horizontal polarization at higher incidence angles (This is demonstrated Figures 9.1 – 9.4). In addition, proposed models were unable to explain the frequency dependence of sea echo. A key observation was that the observed return from the ocean surface decreased with the wavelength of the EM wave, λ, at rates slower than λ^{-4} while proposed theories predicted rated between λ^{-4} and λ^{-6}. Explanations were put forth that necessitated the presence of larger bubbles to be present on the ocean surface to overcome the observed discrepancies. However, this seemed unlikely as large polarization differences were present in the echo at very low wind speeds and sea states [Plant, 1990]. By 1951 no satisfactory explanation had been put forth to explain the sea echo phenomenon at large incidence angles.

In 1951 [Rice, 1951] published a theoretical investigation into the scattering of EM waves from 'slightly rough surfaces'. Rice characterized the surface as a small perturbation of a smooth surface. The result of his calculation indicated that the scattered return was proportional to the Fourier transform of the surface roughness at a wavenumber which depended on radar parameters [Plant, 1990]. Thus, the amplitude and frequency dependence of the returned signal depended on those of a particular Fourier component of the surface roughness [Plant, 1990].

The applicability of the theory put forward by [Rice, 1951] to sea scatter return at microwave frequencies, where the sea surface displacement was large when compared to the incoming EM wavelength, remained questionable until the late 1960s [Plant, 1990]. At that time, independent research in the U.S. and Soviet Union published results confirming the applicability of perturbation theory to very small disturbances [Wright,1966], [Bass et. al,1968 (a)] which was immediately followed by papers proposing support for a composite surface theory to explain the scattering of microwaves from a realistic ocean surface [Wright,1968], [Bass et. al,1968 (b)].

These papers postulated that the longer waves on the ocean surface could be treated using a tangent plane approximation while the shorter waves on the surface did the scattering. In this way, the large-scale ocean surface was approximated by an array of plane surfaces, each of which was tilted due to the long waves of the ocean surface where each plane surface has dimensions that are a fraction of the long wavelength. The first-order perturbation theory is then applied to each of the small surface planes to yield the scattered signal from it [Plant, 1990]. These studies showed that the frequency, incidence angle and polarization dependence of the sea echo was explained well by the composite theory.

It should be noted that Perturbation-type scattering has come to be referred to as ‘Bragg scattering’ after a similar diffraction-type scattering which occurs when solids are illuminated by X-rays. This is a process that was first observed by W.L. Bragg in 1913 [Plant, 1990].

[Plant, 1990] explains that Bragg scattering theories, i.e. slightly rough and composite, can explain most of the overall properties of microwave backscatter from the sea/air interface at intermediate incidence angles. The theories are approximations which can be derived from Maxwells equations by matching boundary conditions at the interface. However, as approximations these models cannot account for backscatter from every individual realization of a random ocean surface.

3.2 Surface Scattering Mechanism: Dielectric properties

The electrical characteristics of a scattering surface has a significant impact on the backscatter returned to the SAR. The ability of a substance to store and transmit electrons is indicated by the *dielectric constant* and is closely related to the conductivity of the material [Chuvieco and Huete, 2010]. All natural materials have an associated complex dielectric constant ε:

$$\varepsilon = \varepsilon' + i\varepsilon'' \tag{3.1}$$

Where the imaginary part corresponds the materials ability to absorb the EM wave and transform its energy into another type of energy, i.e. heat for example [Elachi and van Zyl, 2006]. In short, the real part of the dielectric constant signifies the efficiency of dielectric material to store electrical energy and the dielectric loss indicates the loss of electrical energy in the form of heat energy. The dielectric constant can be thought of as a measure of the electric response of matter [Shivola, 2008], specifically it describes the tendency of a material to polarize in response to an applied electrical field.

A brief summary is given as follows. Matter is on average electrically neutral, but is composed of charged elements. In the atomic model, electrons contain a negative charge which surrounds a positively charged nucleus. When matter is an ideal dielectric, its electrons are not allowed to be carried around by an applied electric field. Instead, an applied electric field displaces the electrons from their equilibrium positions while a restoring force tries to return the electrons to their undisturbed locations. The result of these two forces applied to these charges is a net displacement of positrons in the direction of the electric field and a net displacement of electrons in the direction opposite to the direction of the electric field. The result is a dipole moment that is proportional to the electric field. However, matter can be composed of charge distributions in many various ways, indicating that its response to electric excitation can be classified into different types of polarization [Shivola, 2008].

It should be noted that there is a nuanced difference between dielectric materials and insulators. Insulators do not allow for the flow of charge. Dielectric materials can be thought of as insulators that become polarized in the presence of an external electric field.

3.2.1 Electronic polarization

This type of polarization is caused by the displacement of the electron cloud with respect to the nucleus and can be observed undisturbed in the noble gasses [Shivola, 2008]. A rough description of this polarizability can be calculated by considering the disturbed electrons to be elastically bound to their undisturbed positions and who respond to an applied electric field like harmonic oscillators [Shivola, 2008]. Because of the light mass of electrons, this type of polarization manifests itself at optical and ultraviolet frequencies, as electrons are able to respond quickly to fast-varying excitation.

3.2.2 Atomic and Ionic polarization

When atoms form molecules, they will not always share their electrons symmetrically. The irregular distribution of the electron cloud leads to situations where the atoms in the molecule acquire charge. When an external electric field is then applied, the effect is to displace atoms or groups of atoms thus creating dipole moments [Shivola, 2008].

Ionic polarization occurs in a similar manner to atomic polarization but the molecules that are displaying this behavior are bound together by ionic bonds. These types of polarization manifest themselves at optical and infra-red frequencies [Shivola, 2008].

3.2.3 Oriental polarization

When atoms form molecules, situations may arise where the molecule has a dipole moment, even in the absence of an applied electric field. An example of this is a water molecule that has a permanent dipole moment due to the presence of two hydrogen atoms and one oxygen atom. The hydrogen atoms tend to be more electropositive than the oxygen atoms. This configuration results in the molecule suffering a torque when an external electric field is applied [Shivola, 2008]. This orientational polarization is induced at lower frequencies, i.e. optical waves do not contribute to this phenomena [Shivola, 2008]. It should be noted that thermal motion is a force that tends to preserve the randomness of molecules when an electric field is applied.

3.2.4 Penetration Depth and Mixing Formulas

The dielectric properties of a material, as well as the frequency of the radiation, determine the penetration depth the incident wave. This quantity is the depth in which an EM wave will be attenuated to $\frac{1}{e}$, where e is Eulers number, and is given by

$$\delta_p = -\frac{\lambda}{2\pi\left|Im\left(\sqrt{\varepsilon}\right)\right|} \tag{3.2}$$

where λ is the wavelength of the incoming radiation and $Im(\cdot)$ denotes the imaginary part of ε, as defined in equation (3.1).

This effect can be seen in Figure 3.1. This image shows two σ^0_{VV}F-SAR images, operating at S- and L-band (top left and top right, respectively) of discharged soybean oil acquired during the NORSE2019 oil-on-water experiment. The L-band radiation was approximately 22 cm while the S-band radiation was 9 cm approximately. As can be seen, the L-band image (top right) appears to show a greater degree of penetration into the soybean oil material than the S-band image. However, as will be explained in section 3.2 and 3.3, the modification of the radiation returned to the SAR can be dependent on both the small-scale roughness characteristics as well as the dielectric properties of the scattering surface. Section 4.3.4 will introduce the co-polarization ratio which is the ratio between the intensities of the VV channel and the HH channel. A key characteristic of this parameter is that it is primarily dependent on the dielectric properties of the material (this parameter also depends on other factors such as incidence angle which will not be discussed here) as the small-scale roughness parameters cancel out in the division.

The co-polarization ratio imagery for the S- and L-band acquisitions can be seen in the bottom left and bottom right panels of Figure 3.1, respectively. As can be seen, a high degree of contrast can be seen in the S-band co-polarization ratio image between the slick filled areas and open ocean. In the L-band co-polarization ratio image, very little contrast can be seen between the slick filled areas in contrast to the open ocean. The discrepancy is most likely due to the S-band radiation having a higher change of being modified by the bulk of the soybean oil material whereas the L-band radiation has a higher probability of being modified by the underlying ocean due to the higher penetration ability of L-band radiation.

According to [Minchew et al.,2012, Brekke et al., 2014] mineral oils, as well as natural biogenic slicks, have relatively low dielectric constants, with real parts ranging between 2.2 to 2.3 and with imaginary parts having a value equal to 0.02 approximately, over the frequency ranges of 0.1 to 10 GHz. The dielectric constant of sea water falls in the range above 60 with a value for the imaginary part above 40 for the same frequency range.

As will be outlined in section 4.3.1 when mineral oil is inserted into the marine environment emulsification occurs whereby the pollutant absorbs sea water. The result is a scattering surface with dielectric values between that of pure mineral oil and pure sea water.

In order to model the change in dielectric values of the scattering surface, mixture formulas are used [Angelliaume et al., 2018]. One mixture model that is commonly cited is the linear mixture model which is given below.

$$\varepsilon_{eff} = vol \cdot \varepsilon_{oil} + (1 - vol)\varepsilon_{w} \tag{3.3}$$

where vol, ranges from 0 to 1 and is an indication of the oil content, in terms of volume, of the oil-water mixture, and ε_{oil} and ε_{w} are the relative dielectric constants of pure seawater and pure mineral oil, respectively. The Bruggeman mixing formula, given as

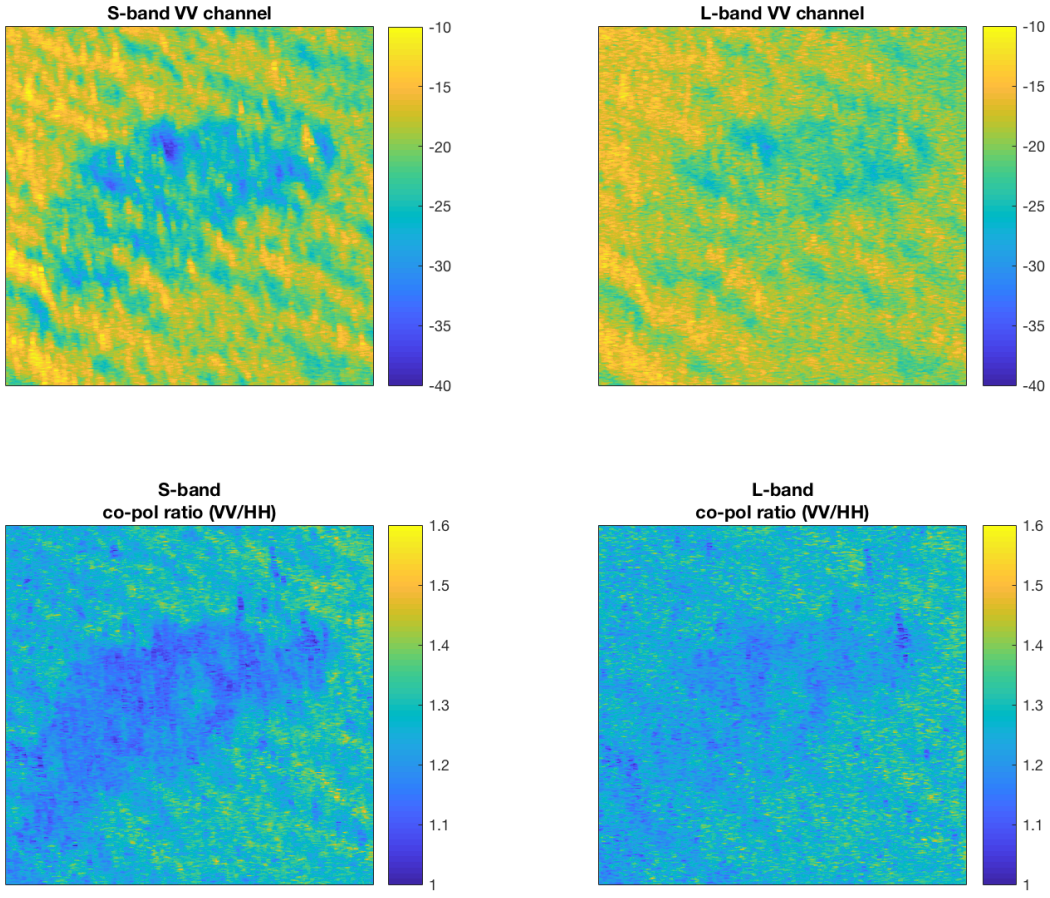

Figure 3.1: Top Left: S-band σ^0_{VV} F-SAR image of mineral oil emulsion slick acquired during flight 1 shortly after release during the NORSE2019 oil-on-water experiment. Top Right: The corresponding L-band image. Bottom Left: Co-polarization ratio image in S-band. Bottom right: Co-polarization ratio image in L-band. The F-SAR data and Products

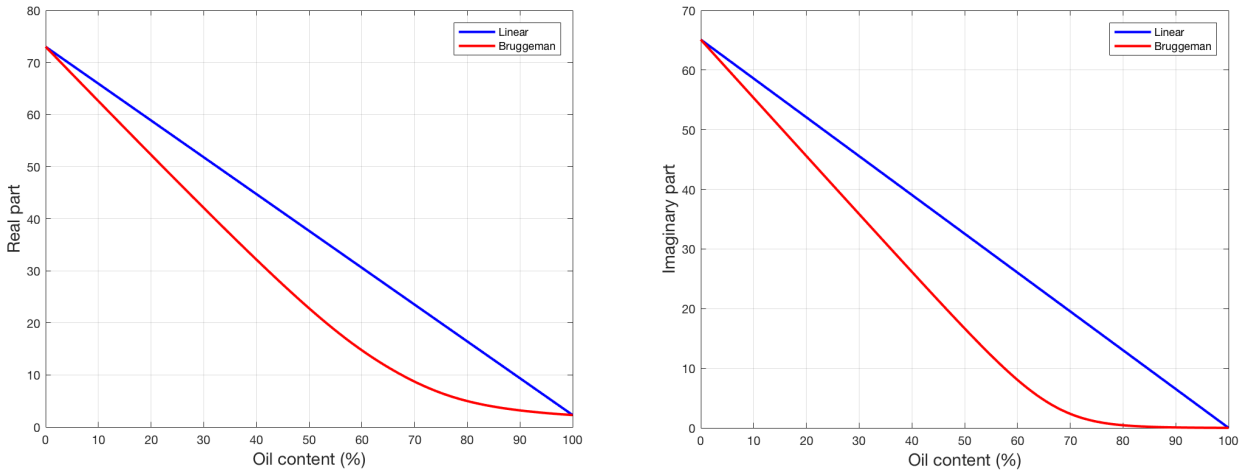

Figure 3.2: Plots of volumetric mixing models. Left: Real part of effective dielectric constant of oil-in-water mixture plotted against volumetric oil content for the linear model (blue) and Bruggeman model (red). Right: Corresponding plot for imaginary part.

$$\varepsilon_{eff} = \frac{1}{4}\Big\{\varepsilon_w - (1 - 3 \cdot vol)(\varepsilon_{oil} - \varepsilon_w) + \sqrt{[\varepsilon_w - (1 - 3 \cdot\ vol)(\varepsilon_{oil} - \varepsilon_w)]^2 + 8\varepsilon_w \varepsilon_{oil}}\Big\} \tag{3.4}$$

is also cited in the literature as a more relevant approach which comes from the Effective Medium Theory [Shivola, 2008]. [Angelliaume et al., 2018] used this model to determine the volumetric fraction of oil within verified oil slick discharged during the NOFO 2015 oil-on-water exercise conducted in the North Sea.

Figure 3.2 shows the real and imaginary parts of the effective dielectric constant of an oil-in-water emulsion for both these functions plotted as a function of oil content (percentage) for both the linear model (blue curves) and the Bruggeman formula (red curves). As can be seen, a strong over prediction can be observed in the real and imaginary parts with the linear model when compared with the Breggeman formula. This is more pronounced for a high concentration of oil, i.e. low values of ε_{eff}. These two models were plotted for ε_{oil} and ε_w having values of 73.0 + 65.1i and 2.3 + 0.01i (L-band), respectively.

It should be noted that these two mixing formulas belong to a family of such models. The reader is directed to [Shivola, 2000] for a more thorough treatment.

3.2.5 Temperature and Salinity Dependence of Sea Water

According to [Klein and Swift 1977] and [Brekke et al., 2014] the complex permittivity of sea water is depenant on temperature and salinity for a given frequency by:

$$\varepsilon(\omega) = \varepsilon_\infty + \frac{\varepsilon_s - \varepsilon_\infty}{1 + (i\omega\tau_r)^{1-\alpha}} - i\frac{\sigma}{\omega\varepsilon_0} \tag{3.5}$$

Where $\omega = 2\pi f$, f is the frequency of radiation, ε_∞ is the dielectric constant of infinite frequency, ε_s is the static dielectric constant, τ_r is the relaxation time (measured in seconds), σ

is the ionic conductivity (measured in mhos/m), α is an empirical parameter which describes the distribution of relaxation times and $\varepsilon_0 = 8.854 \times 10^{-12}$ is the permittivity of free space (measured in farads/m).

The dependence on temperature and salinity of sea water is given through ε_s, τ and σ. Figure 3.3 shows estimations for the complex relative permittivity of sea water for a range of salinity and temperature values taken from [Brekke et al., 2014]. The graphs were plotted for a radar frequency of 1.257 GHz (L-band). As can be seen, the real part decreases with increasing temperature and with an increase in salinity. The imaginary part becomes more negative with an increase in temperature and an increase in salinity. This is associated with an increase in conductivity [Brekke et al., 2014].

3.3 Surface Scattering Mechanism: Roughness

When an interface between two media of different electric and magnetic properties is present, EM waves that are incident upon it will be affected. The way in which they will be affected is as follows.

Consider a plane EM wave travelling in a vacuum half-space (Earths atmosphere behaves the same way as a vacuum when dealing with the frequencies used for spaceborne radars) and incident upon a dielectric half-space with dielectric constant of ε. The EM radiation will cause the atoms of the dielectric to oscillate which will in turn radiate waves in all directions. Some of this radiated energy will be directed upwards and some downwards [Elachi and van Zyl, 2006].

If the surface is flat, the impinging wave will cause the atoms in the material to oscillate at a relative phase such that the resulting field consists of two reradiated waves, one in the upper half-space and one in the lower half-space. The one in the upper half-space will be reradiated at an angle equal to the incidence angle θ, the one in the lower half-space will be radiated into the bulk material at an angle

$$\theta' = arcsin\left(\frac{\sin\theta}{\sqrt{\varepsilon}}\right) \tag{3.6}$$

Figure 3.4 (left panel) shows a schematic of a plane EM impinging upon a perfectly flat surface and another plane wave being reflected at a reflection angle equal to the angle of incidence, i.e. the specular direction.

If the interface between the two half-spaces is roughened, some of the energy will be radiated in all directions. This is referred to as the scattered field. The amount of energy that is scattered in all directions is dependent on the amount of roughness of the interface relative to the wavelength of the incident radiation [Elachi and van Zyl, 2006]. Figure 3.4 (center panel) shows the situation when the surface is slightly roughened. As can be seen, some of the radiation will still be reflected in the specular direction while some will become diffuse. When the surface is very rough, as can be seen in Figure 3.4 (right panel) the backscattered signal will be completely diffuse and a high degree of depolarization will occur [Espeseth, 2019].

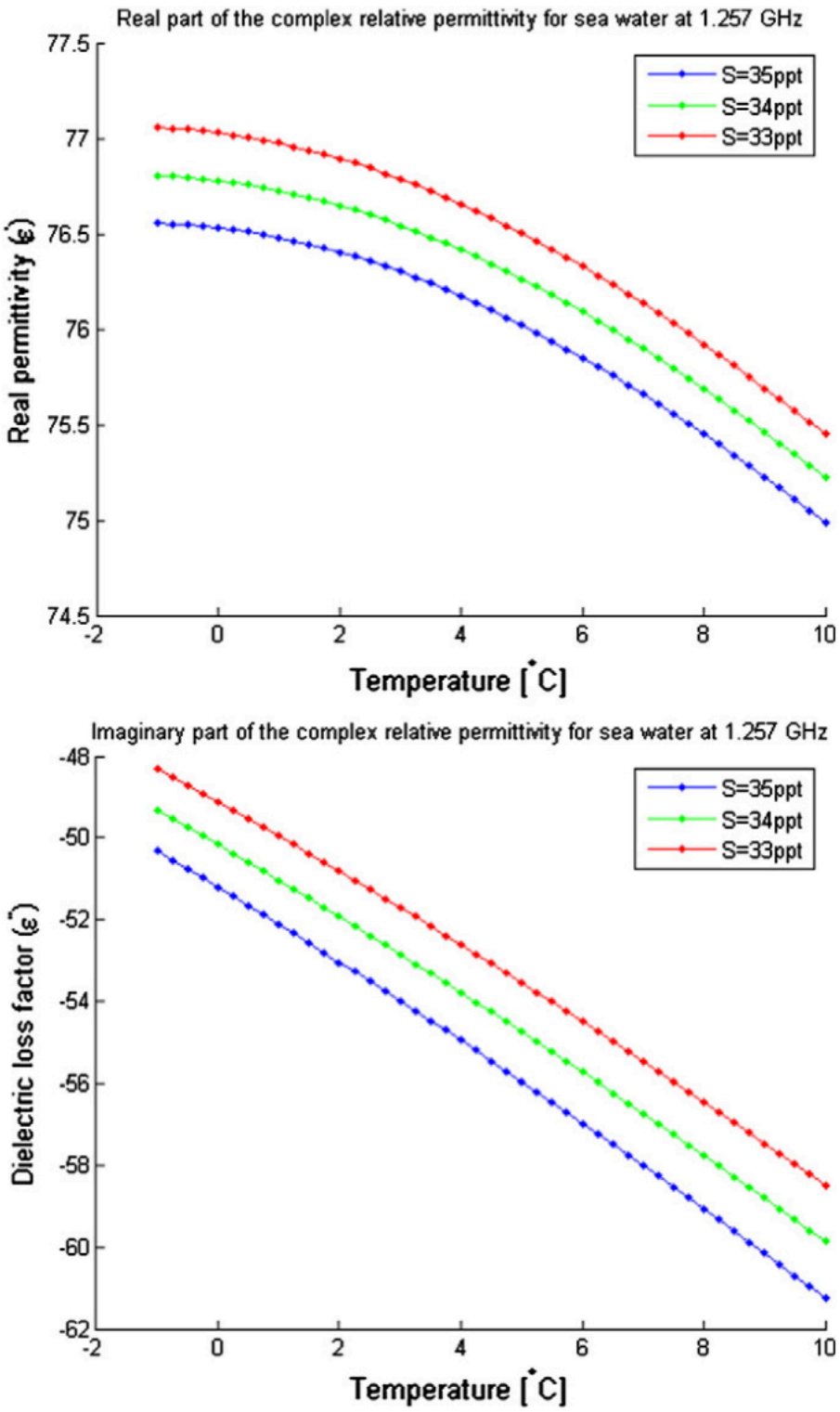

Figure 3.3: The complex relative permittivity of seawater plotted as a function of salinity and temperature. Ppt: parts per thousand (‰). Graphs are plotted for a frequency of radiation of 1.257 GHz (L-band). Real part is shown in the top panel while the imaginary part is shown in the bottom panel. Figure is reproduced from [Brekke et al., 2014].

The surface roughness can be related to the wavelength of the incident wave via the Rayleigh criterion. This criterion states that a surface can be considered to be rough, in reference to the wavelength of the incoming radiation, if

$$s_h = \frac{\lambda}{8}\cos(\theta) \tag{3.7}$$

where, s_h is the standard deviation of the surface height, λ is the wavelength of the incoming radiation and θ is the incidence angle of the radiation.

Quantifying the degree of surface roughness present on a surface can be difficult. For this purpose, various parameters are employed for this task. [Gadelmawla et al., 2002] illustrated 59 distinct roughness parameters that are generally grouped into three distinct categories; amplitude parameters, spacing parameters and hybrid parameters.

Amplitude parameters are used to measure the vertical characteristics of surface deviations and are considered the more important of the collection of surface parameters to characterize surface topography [Gadelmawla et al., 2002]. Spacing parameters are those which measure the horizontal characteristics of surface deviations. These type of surface parameters are relevant for industrial production [Gadelmawla et al., 2002]. Hybrid properties contain a combination of the two previous types of surface parameter. These types of parameters are relevant for engineering studies [Gadelmawla et al., 2002].

In the following, a brief discussion on three roughness parameters that are relevant to the scattering models outlined in this thesis are included. These are the *auto correlation function* (ACF), *correlation length* (β) and *power spectral density* (PSD).

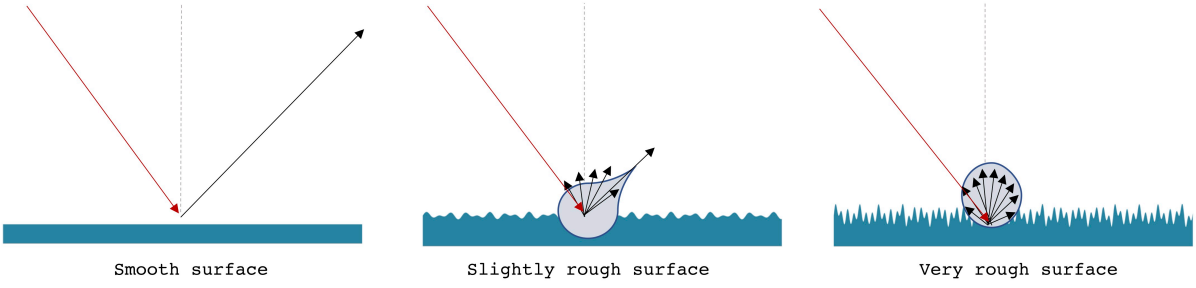

Figure 3.4: Scattering from an interface with differing degrees of roughness. Taken from [Espeseth, 2019].

3.3.1 Autocorrelation Function

According to [Gadelmawla et al., 2002] the Autocorrelation function can be estimated as

$$ACF(\delta x) = \frac{1}{L_p}\int_0^{L_p} y(x)\, y(x+\delta x)dx \tag{3.8}$$

$$ACF(\delta x) = \frac{1}{N-1}\sum_{i=1}^{N} y_i y_{i+1} \tag{3.9}$$

Where δx is the shift distance and y_i is the height of the surface profile at a point number i, L_p is the profile length and N the number of points in a profile. The first expression is a mathematical expression for the ACF while the second expression is a numerical expression.

The explanation of this quantity is succinctly provided by [Park N.L., 2014] and intuitively explains the equations above. The autocorrelation function is a measure of how random or periodic a surface is. This quantity is found by creating a duplicate surface and then sliding the duplicate relative to the original in all directions. At each point that the duplicate is moved, the two data sets are multiplied together and the result is integrated and then normalized to the value found for zero shift.

If the ACF is normalized, values can range from 1 (indicating correlation) to -1 (indicating no correlation). For a completely flat, infinite surface, the normalized ACF will stay at 1. For a random surface, the normalized ACF will dampen to 0 quickly as individual regions are as likely to align as not. In this way, the normalized ACF is a measure of how similar the texture is at a given distance from the original location [Park N.L., 2014].

3.3.2 Correlation Length

The correlation length is a measure of the distance over the surface such that the new location will have minimal correlation with the original location. The direction over the surface that is chosen to find the correlation length is the direction that will give the lowest value [Park N.L., 2014].

This parameter is used to outline the correlation characteristics of the ACF. Points that are on the surface but separated by more than the correlation length can be considered as uncorrelated. As an example, if we have a periodic waveform, the correlation length is infinity while the correlation length for a completely random waveform is 0 [Gadelmawla et al., 2002].

3.3.3 Power spectral density

The following explanation for the Power spectral density was taken from [Park N.L., 2014]. According to Fourier analysis, the texture that a surface has is composed of a series of sine waves that are orientated in various directions with different spatial frequencies and amplitudes.

The power spectrum is a measure of the amplitude of each sine wave for a particular spatial frequency along a given direction. The spatial frequency being 1 divided by the wavelength. Thus, the power spectrum would be a 3-dimensional function where the X and Y axes represent the spatial frequencies in a given direction. The Fourier transform of the autocorrelation function is the power spectral density.

3.4 Overview of Surface Scattering Models

The logic of developing theoretical scattering models is summed up succinctly by [Fung, 1994]. Here, the authors state that theoretical modeling deals with either the radar cross section or the scattering coefficient of a target. In defining these quantities, the effects of antenna pattern and range have been removed so that these quantities are only influenced by the target and the exploring EM wave parameters, and are independent of the particular system used to perform the measurement. Explicitly stated, some of the reasons we may want to develop theoretical scattering models is as follows

1. To aid data interpretation by illustrating a relationship between a measured quantity as a function of the geometric and electromagnetic parameters of the target.
2. To investigate the sensitivity of a measured quantity to the target parameters of interest.
3. To create simulated data for simulation studies or for the training of neural networks.

It should be noted however, that this list is not exhaustive.

This section will serve to outline some of the work that is done in the development of theoretical scattering models (note, for completeness non-theoretical scattering modes are also included) in the context of remote sensing as well as outlining the model that is used in this study, the Polarimetric Two-Scale Model (PTSM). This section of the thesis is not designed to provide a comprehensive and exhaustive account of the field, but to give a brief overview, and to provide motivation for choosing the PTSM as well as providing a reference to the reader for the theory illustrated in the papers.

3.4.1 Idealized Scattering: Fresnel Reflectivity

As a starting point, we can consider an idealized situation where we have a perfectly smooth interface with radiation impinging upon it at an angle of incidence θ and an angle of reflection θ'. Both the upper and lower mediums are considered uniform with differing refractive indices. Such a situation can be seen in Figure 3.4 (Left panel).

In this case, the characteristics of reflection can be described by Fresnel Reflectivity where the Fresnel coefficients are given by

$$\Gamma_v(\theta) = \frac{\varepsilon \cos\theta - \sqrt{\mu\varepsilon - sin^2\,\theta}}{\varepsilon \cos\theta + \sqrt{\mu\varepsilon - sin^2\,\theta}} \tag{3.10}$$

$$\Gamma_h(\theta) = \frac{\mu \cos\theta - \sqrt{\mu\varepsilon - sin^2\,\theta}}{\mu \cos\theta + \sqrt{\mu\varepsilon - sin^2\,\theta}} \tag{3.11}$$

Where Γ_v and Γ_h are the Fresnel coefficients for the vertical and horizontal coefficients of the radiation, μ is the magnetic permeability of the material. Note, for non-ferromagnetic media, such as natural surfaces, μ is always equal to 1. The angle under which the transmitted wave is completely absorbed by the dielectric medium is referred to as the Brewsters angle.

As an example, equations (3.10) and (3.11) were plotted for a ε value equal to 5, a typical value for glass. The Brewsters angle can be seen at a value of 65.9° approximately. The reflectivity decreases for increasing incidence angle.

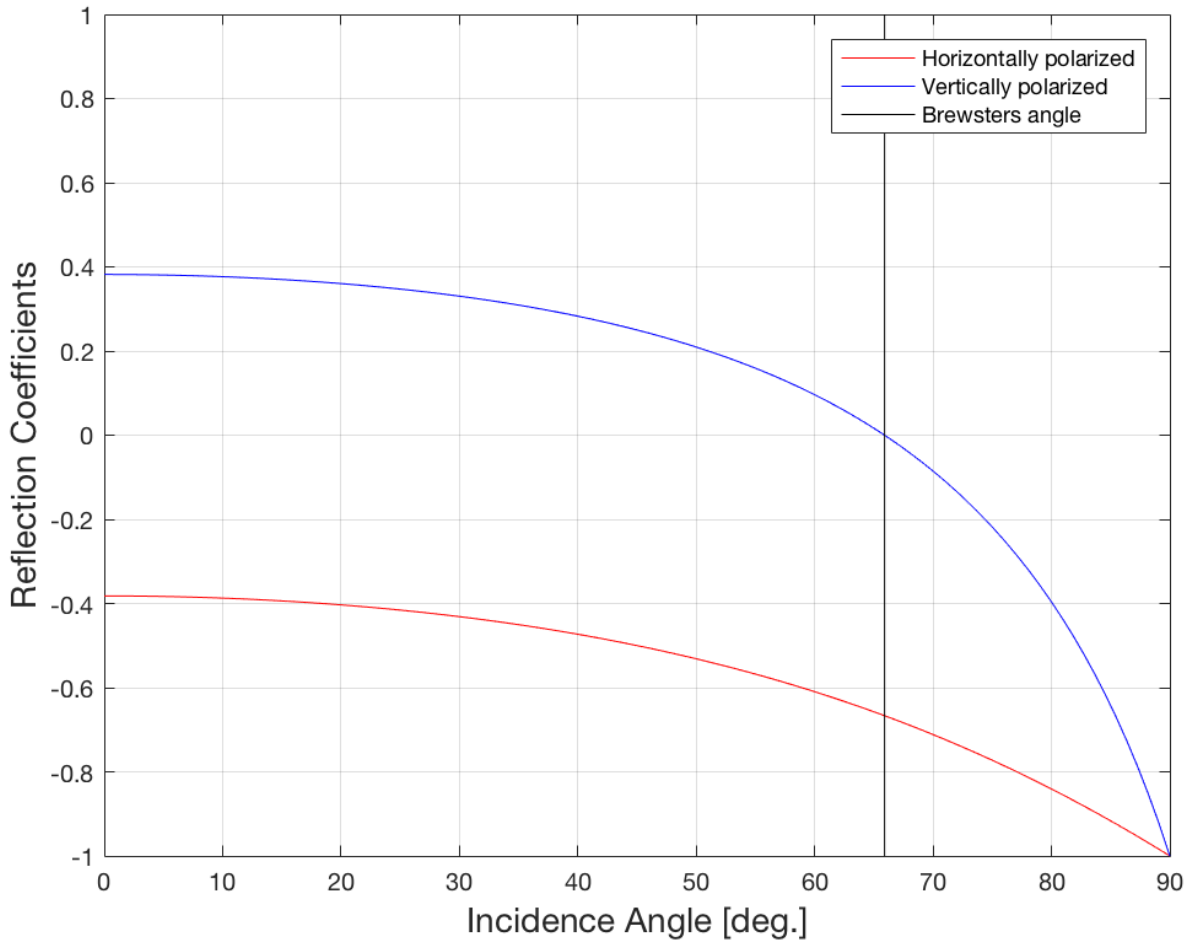

Figure 3.5: Graph showing the Fresnel reflectivity coefficients plotted for various incidence angles. The Brewsters angle is also indicated.

3.4.2 Empirical Scattering Models

Empirical or semi-empirical approaches are grounded in theoretical models that are extended or modified according to empirical observations or physical considerations [Hajnsek, 2001]. The purpose is to increase the performance of a model in order to extract relevant information from experimental data. In this section, two empirical models are presented, which themselves are extensions to the Small Perturbation Model (SPM) (which will be presented in the next subsection). The benefit of these models is that they extend the range of validity in regards to surface conditions and thus resulting in a higher estimation accuracy of key parameters. The drawback is that they were developed for use on soil moisture estimation (at least the ones that will be discussed in the coming subsections) and are probably inapplicable to ocean surface remote sensing. The following discussion however is useful in illustrating work conducted in the field.

3.4.2.1 The Oh Model

This model was developed based on measurements made by a truck mounted scatterometer operating at three frequencies (1.5, 4.5 and 9.5 GHz) in a fully polarimetric mode with incidence angles ranging between 10° and 70° [Hajnsek, 2001]. On the basis of these scatterometer measurements and ground measurements, empirically determined functions for the co- and cross-polarized backscatter ratios, p and q respectively, were proposed.

$$p = \frac{\sigma^0_{HH}}{\sigma^0_{VV}} = \left(1 - \left(\frac{2\theta}{\pi}\right)^{\frac{1}{3\Gamma^0}} . e^{-ks_{rms}}\right)^2 \tag{3.12}$$

$$q = \frac{\sigma^0_{HV}}{\sigma^0_{VV}} = 0.23\sqrt{\Gamma^0}(1 - e^{-ks_{rms}}) \tag{3.13}$$

Where θ is the incidence angle, k is the wave number, s_{rms} is the root mean square (RMS) height and Γ^0 is the Fresnel reflectivity coefficient at nadir, i.e. $\theta = 0$.

$$\Gamma^0 = \left|\frac{1 - \sqrt{\varepsilon'}}{1 + \sqrt{\varepsilon'}}\right|^2 \tag{3.14}$$

ε' is the relative dielectric constant. At specific angles of incidence, (3.12) and (3.13) constitute a system of two non-linear equations with two unknowns, i.e. s_{rms} and ε'.

In this model, the co-polarized ratio always has values lower than unity for all local incidence angles, values for ε' and surface roughness parameters. This can be seen in Figure 3.6. It was determined that this model is more appropriate for lower frequencies, i.e. S-, L- and P-bands.

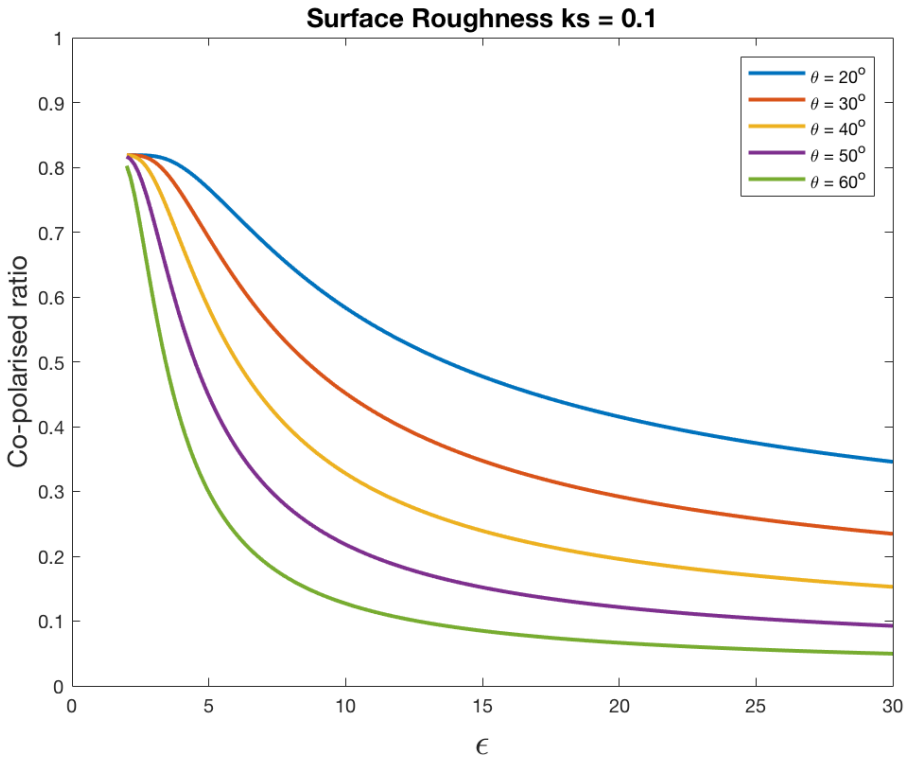

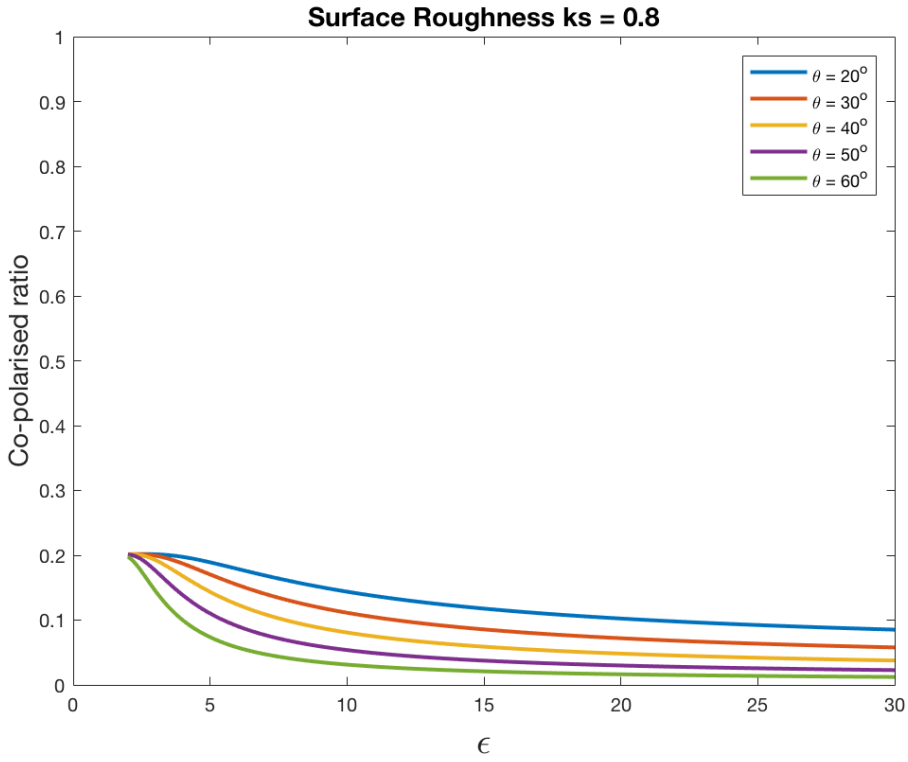

Figure 3.6: The co-polarization ratio as calculated by the Oh model for a range of roughness values.

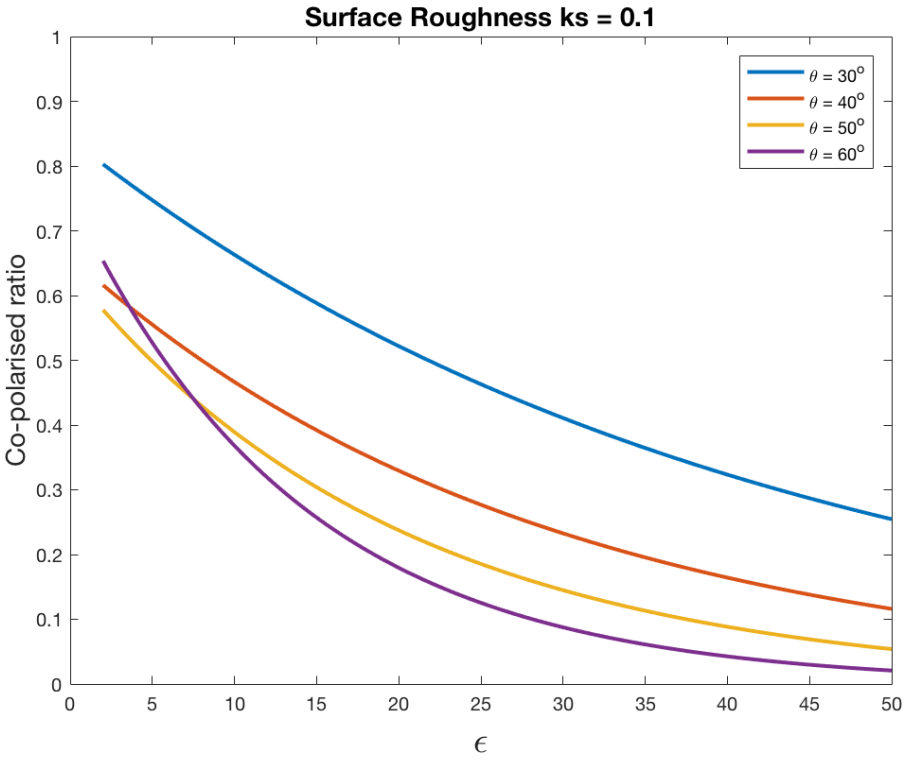

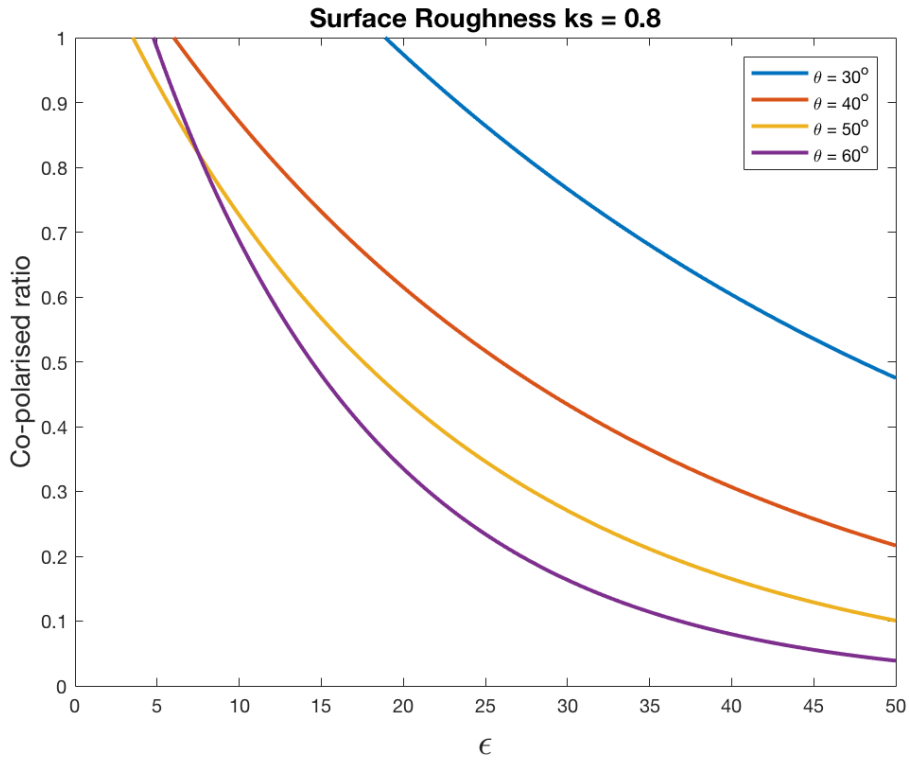

Figure 3.7: The co-polarization ratio as calculated by the Dubois model for a range of roughness values.

3.4.2.2 The Dubois Model

This model is a simplification of the aforementioned Oh model and addresses only the co-polarised backscatter [Hajnsek, 2001]. The model was originally developed with scatterometer measurements operating at frequencies ranging between 2.5 to 11 GHz and later applied to AIRSAR and SIR-C (both SAR instruments) for the purposes of determining its robustness.

The derived model equations for the co-polarized backscatter is given as follows

$$\sigma^0_{HH} = 10^{-2.75} \frac{cos^{1.5}\theta}{sin^5\theta} \, 10^{0.028\varepsilon' tan\theta} (ks_{rms} \cdot \sin\theta)^{1.4} \lambda^{0.7} \tag{3.15}$$

$$\sigma^0_{VV} = 10^{-2.37} \frac{cos^{3}\theta}{sin^3\theta} \, 10^{0.046\varepsilon' tan\theta} (ks_{rms} \cdot \sin\theta)^{1.1} \lambda^{0.7} \tag{3.16}$$

The model parameters have the same meaning as the ones in the Oh model. Similar to the SPM, which will be discussed in the next section, the Dubois model predicts the backscatter coefficient will decrease with increasing local incidence angle and/or with decreasing surface roughness [Hajnsek, 2001]. This can be seen in Figure 3.7.

These empirically determined expressions predict that the co-polarization ratio $\sigma^0_{HH}/\sigma^0_{VV}$ is roughness dependent and will increase with increasing surface roughness.

3.4.2.3 Comparison between models

In recent years, a great deal of work has been conducted on comparing these empirical backscattering models between each other and also evaluating them against theoretical backscattering models for the purposes of soil moisture estimation.

[Panciera et al., 2013] for example compared the Oh model, the Dubois model and the Integral Equation Model (a theoretical backscattering model) against each other using L-band airborne SAR data and found the Oh model to be the more accurate among the three. [Baghdadi et al., 2006] did the same but using X-band data. They found that the Oh model correctly simulates the co-polarized ratio (3.12) but systematically overestimated the cross-polarization ratio (3.13). They found the Dubois model underestimated the backscatter-coefficient for surfaces with low levels of roughness and overestimated the backscatter-coefficient for larger surface roughness conditions. Intermediate roughness conditions were modeled correctly according to the authors.

[Choker et al., 2017] performed a comparison between these three models using data from 9 SAR sensors spanning X-, C- and L-bands. The results again showed that the Oh model gave the best fit of the backscattering coefficients HH and VV polarizations than the Dubois model. The authors of this study also note that the performance of the Oh model over the Dubois model was better in X- and C-bands than L-band.

3.4.3 Theoretical Scattering Models

The behavior of EM waves scattering from rough dielectric surfaces has been an active area of research for many years. Despite the attention this area of research has received, the general scattering problem has proven analytically, not completely solvable. Because of this, a host of approximate solutions have been put forward with the drawback being restricted applicability or being too general to be of practical use. The following is a brief overview of theoretical scattering models relevant to this thesis. The theoretical models discussed in this subsection are not the only ones cited in the literature, but are chosen for discussion here as they build on one another.

3.4.3.1 Small Perturbation Model

When the surface roughness is small in comparison to the incoming wavelength, the method of small perturbation is applicable to determine the backscattering coefficient. In this model, the model is characterized by the surface height standard deviation, s_h, its correlation length, L, and the surface roughness spectrum, or in an equivalent sense, the surface correlation function [Fung, 2010].

As can be seen in Figure 3.4 (Left panel), a perfectly smooth surface has zero backscatter at oblique incidence angles. In the Bragg scattering region, where the surface height variation is small in comparison to the wavelength, i.e. when $ks_h << 0.3$, the inclusion of surface roughness can be thought of as a perturbation of the smooth scattering problem. The backscatter coefficients can be obtained directly from Maxwells equations [Grahn, 2018].

According to this model, the random surface is decomposed into its Fourier spectral components where each component corresponds to an idealized sinusoidal surface. The scattering that occurs is primarily due to the spectral component of the surface which is in resonance with the incident wavelength at a specific incidence angle [Hajnsek, 2001]. The scattering matrix for a Bragg surface has the form

$$[\boldsymbol{S}] = \begin{bmatrix} S_{HH} & S_{HV} \\ S_{VH} & S_{VV} \end{bmatrix} = m_s \begin{bmatrix} R_s(\theta, \varepsilon) & 0 \\ 0 & R_p(\theta, \varepsilon) \end{bmatrix} \tag{3.17}$$

Where m_s is the backscatter amplitude which contains information relating to the roughness of the surface, R_s and R_p are the Bragg scattering coefficients both perpendicular and parallel to the plane of incidence respectively. Both of these quantities are functions of the complex permittivity ε and the incidence angle θ, and are given as

$$R_s(\theta, \varepsilon) = \frac{\cos\theta - \sqrt{\varepsilon - \sin^2\theta}}{\cos\theta + \sqrt{\varepsilon - \sin^2\theta}} \tag{3.18}$$

$$R_p(\theta, \varepsilon) = \frac{(\varepsilon - 1)\left(\sin^2\theta - \varepsilon(1 + \sin^2\theta)\right)}{\left(\varepsilon\cos\theta + \sqrt{\varepsilon - \sin^2\theta}\right)^2} \tag{3.19}$$

A highly relevant aspect of the SPM states that the co-polarization ratio, R_s/R_p, depends only on ε and θ and is independent of surface roughness.

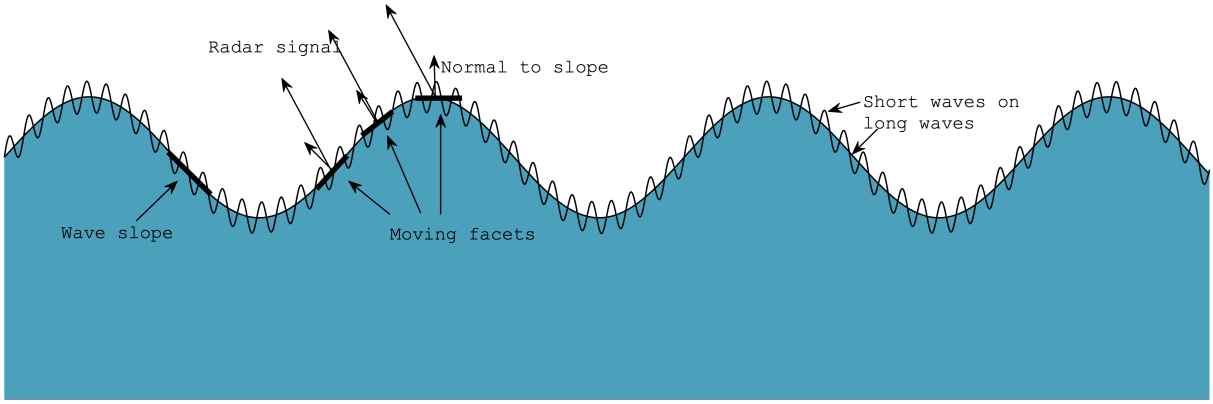

Figure 3.8: Illustration showing the large- and small-scale ocean roughness features. Surface facets are superimposed on the large-scale surface undulations upon which small-scale roughness undulations are imposed [Espeseth, 2019].

Given that the ocean surface will not be a slightly roughened surface but is composed small-scale surface undulations superimposed on large-scale surface undulations, the validity range of the SPM is too strict to be of any practical importance. This can be seen in Figure 3.8. Because the model does not account for these large-scale undulations, cross-polarization and depolarization effects are not accounted for.

In order to model this, two-scale approaches have been put forward which have different approaches to modelling the tilts, slopes and/or rotation of the surface facets [Espeseth, 2019].

3.4.3.2 XBragg Model

In order to extend the Bragg scattering model to a wider range of roughness conditions, two effects need to be introduced, non-zero cross-polarized backscattering and depolarization. [Hajnsek et al.,2003] proposed the Extended Bragg model (XBragg) to account for these terms. The departure of this model from conventional two-scale models was the introduction of the depolarization effects [Hajnsek et al.,2003]. The following is an account of that model.

In an effort to introduce a roughness disturbance, the surface is modeled as a reflection symmetric depolarizer via a rotation of the Bragg coherency matrix $[T]$ about an angle β in the plane perpendicular to the scattering plane and performing a configurational averaging over the distribution $P(\beta)$ of β. The resulting $[T]$ is given as

$$[T] = \int_0^{2\pi} [T(\beta)] P(\beta) \mathrm{d}\beta \tag{3.20}$$

The width of the distribution corresponds to the degree of roughness disturbance of the modelled surface [Hajnsek et al.,2003]. If we assume that $P(\beta)$ is a uniform distribution about zero with a width of β_1, then

$$P(\beta) = \begin{cases} \dfrac{1}{2\beta_1} & |\beta| \leq \beta_1 \\ 0 \leq \beta_1 \leq \dfrac{\pi}{2} \end{cases} \tag{3.21}$$

The equation for $[T]$ represents the coherency matrix of an extended Bragg surface that is characterized by cross-polarized energy and with a polarimetric coherence less than 1. Explicit equations can be found in [Hajnsek et al.,2003].

3.4.3.3 Polarimetric Two-Scale Model

[Iodice et al., 2011] provides the following interpretation. The scattering surface can be considered to be composed of randomly tilted rough facets that are large with respect to the wavelength but that are small with respect to the resolution of the sensor. The scattering from each of these facets can be determined by employing the SPM, but the random tilt of the facet causes a random variation of the local incidence angle θ_l with respect to the look angle as well as a random rotation β of the incidence plane around the line of sight.

The PTSM is the model that was implemented in paper 1 and paper 2 of this thesis. A full derivation can be found in [Iodice et al., 2011] and will not be included here. However, for completeness the expressions modelling the co- polarization and cross-polarization channels is given as

$$\begin{cases} \langle \sigma^0_{HH} \rangle_{/a,b} = \frac{4}{\pi}\left[C^{HH}_{0,0} + \left[C^{HH}_{2,0} + 2\frac{Re\{C^{HV}_{0,0}\} - C^{HH}_{0,0}}{sin^2\theta} + C^{HH}_{0,2}\right]s^2\right] \\ \langle \sigma^0_{VV} \rangle_{/a,b} = \frac{4}{\pi}\left[C^{VV}_{0,0} + \left[C^{VV}_{2,0} + 2\frac{Re\{C^{HV}_{0,0}\} - C^{VV}_{0,0}}{sin^2\theta} + C^{VV}_{0,2}\right]s^2\right] \\ \langle \sigma^0_{HV} \rangle_{/a,b} = \frac{4}{\pi}[C^{HH}_{0,0} + C^{VV}_{0,0} - 2Re\{C^{HV}_{0,0}\}]\frac{s^2}{sin^2\theta} \end{cases} \quad (3.22)$$

where s^2 is a measure that indicates the large-scale roughness. The angle of incidence of the incoming radiation is given by θ. The terms $C^{pq}_{k,n-k}$ are the series expansion coefficients of the function $(k\ cos\ \theta_l)^4 W R_p R^*_q$ and has the form

$$C^{pq}_{k,n-k} = \frac{1}{n!}\binom{n}{k}\frac{\partial^n\left((k\ cos\theta_l)^4 W R_p R^*_q\right)}{\partial a^k \partial b^{n-k}}\Big|_{a=b=0} \quad (3.23)$$

R_p and R_q are the Bragg coefficients where the subscripts and superscripts p and q indicate send and receive polarizations, respectively. The quantity W is the power spectral density (PSD) of the small-scale roughness, with a roughness variance of ${s_h}^2$ [Quigley et al., 2020] [Iodice et al., 2011]. In the PTSM, an assumption is made that the small-scale roughness variance $h_{surface}(x, y)$ is a band-limited *fractional Brownian motion* (fBm) process. This will be explained in the next subsection.

3.4.3.4 Scattering from Fractional Brownian Surfaces

[Franceschetti and Riccio, 2007] provide an in-depth overview of the physical modelling of scattering from natural surfaces. The following explanation in regards to the fractal description of natural media and the scattering modelling of EM radiation from natural media is taken from that reference.

A key point that needs to be made when scattering occurs from natural media is that natural surfaces are not man-made. As a result, they lack the clear-cut geometric properties that are typical of man-made objects. Thus, it is generally difficult to generate a reasonably accurate model for the scattered field and an accurate model or the surface. The geometric modelling of natural surfaces is conducted via the implementation of fractal geometry.

If we consider a stochastic description of rough surfaces, the shape may be modelled via a stochastic process of two independent space variables

$$z(\mathbf{r}) = z(x, y) \tag{3.24}$$

$$\mathbf{r} \equiv \mathrm{x}\hat{\mathbf{x}} + y\hat{\mathbf{y}} \tag{3.25}$$

Here, $z = 0$ is the mean plane and the values for $z(x, y)$ describe the surfaces stochastic corrugations.

The EM field that is scattered from natural media, that can be analytically evaluated in a stochastic manner, can be given in stochastic terms. According to [Franceschetti and Riccio, 2007] the power spectrum can provide an alternative popular representation for a stochastic process and can be applied to describe both the scattering roughness and the scattering field. This can be given as

$$W(K) = \frac{S_0}{K^{(2+2H_t)}} = s^2 \frac{S_{0n}}{K^{(2+2H_t)}} = s^2 W_n(K) \tag{3.26}$$

Where $K = \sqrt{K_x^2 + K_y^2}$ and K_x^2 and K_y^2 are the Fourier mates of x and y, respectively. H_t is the Hurst coefficient, a quantity that is related to the fractal dimension D by $D = 3 - H_t$ and has a value $0 < H_t < 1$. S_0 is a quantity that is directly related to the roughness variance ${s_h}^2$ via the dimensional facet-size-dependent constant S_{0_n} and $W_n(K)$ is the normalized PSD. According to [Iodice et al., 2011] employing a description of the small-scale roughness as a fBm is appropriate as there is a wide consensus that fBm is a proper model for natural surfaces as previously stated. It is assumed that the equation above is valid for ocean surfaces with H_t ranging from approximately 0.65 to 0.95 [Stiassnie et al., 1991].

A discussion on fractal geometry is outside the scope of this thesis. The reader is directed to [Franceschetti and Riccio, 2007] for a more thorough treatment.

4 Marine Imaging with Synthetic Aperture Radar

4.1 Anthropogenic Pollutants

The following list is designed to illustrate some common sources of pollutants that are manmade in origin. The list is not exhaustive and is designed to illustrate some pollutants that can be observed within SAR imagery. Some sources of pollution not mentioned here are water-based or oil-based drilling mud, drain water and seepage from old ship wrecks.

- ***Accidental discharges or spills from ships or oil rigs:*** This is the most typical source of anthropogenic pollutants in the ocean environment. Ships can flush oil into the ocean when they want to clean their engines/tanks instead of docking in harbor. The logic being that they don't have to spend time and money on harbor facilities. Oil rig disasters have also been the source of pollutants into the ocean environment. The most famous case being that of BPs Deep Water Horizon (DWH) drilling rig in the Gulf of Mexico which occurred on 20 April 2010.

- ***Produced water from oil platforms:*** This is water that is intentionally and legally discharged onto the ocean surface. This water is a byproduct of oil and natural gas extraction, i.e. it is water that can be found in a reservoir with hydrocarbons. It is first treated before it is discharged onto the ocean surface. Images of produced water being discharged can be seen in Figures 4.2 and 4.3.

4.2 Oil Spill Look-Alikes

- ***Grease Ice:*** Sea ice also has the ability to dampen ocean surface waves in its early stages of growth. Under calm atmospheric conditions, long thin crystals tend to form into a thin, smooth layer of ice at the water-air interface. As this soupy layer of ice congregates on the ocean surface, slicks form that can have an appearance similar to that of oil slick in SAR imagery. Figure 4.1 shows such slicks of grease ice that were acquired by Radarsat-2 in the Kara Sea. As can be seen, an area of older, rougher ice is also present to the upper right corner of the image.

- ***Internal waves:*** Internal gravity waves can also manifest themselves in SAR imagery. These internal waves are a result of the stratification of the water column and can propagate themselves both vertically and horizontally through a fluid [Sutherland, 2014]. The radar image of internal waves consists of adjacent bright and dark bands. The wavelength of internal waves can typically be on the scale of several kilometers [Brekke, 2008]. Figure 4.2 shows an example of what could be internal waves imaged in the Brage oil field off the coast of Norway, seen as a faint wave like pattern in the top right of the image.

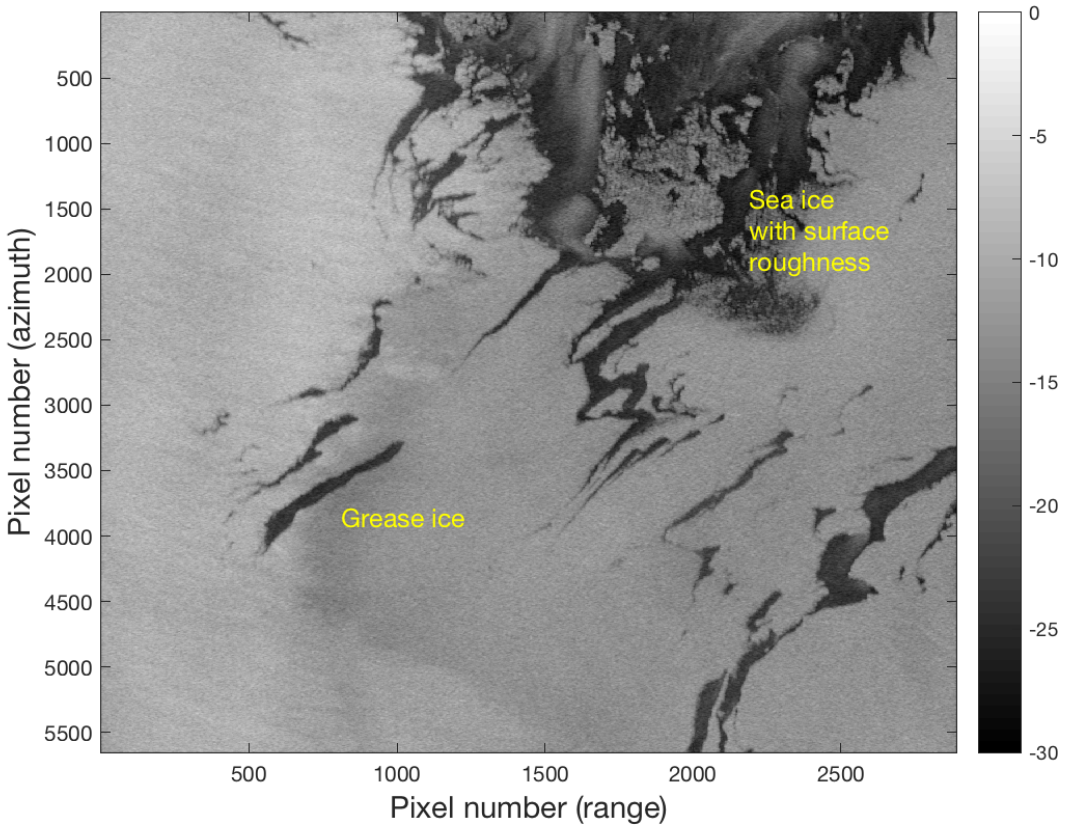

Figure 4.1: Radarsat-2 σ^0_{VV} fine quad-pol image of grease ice in the Kara sea. The Radarsat-2 data and Products © MDA LTD. 2018 – All Rights Reserved

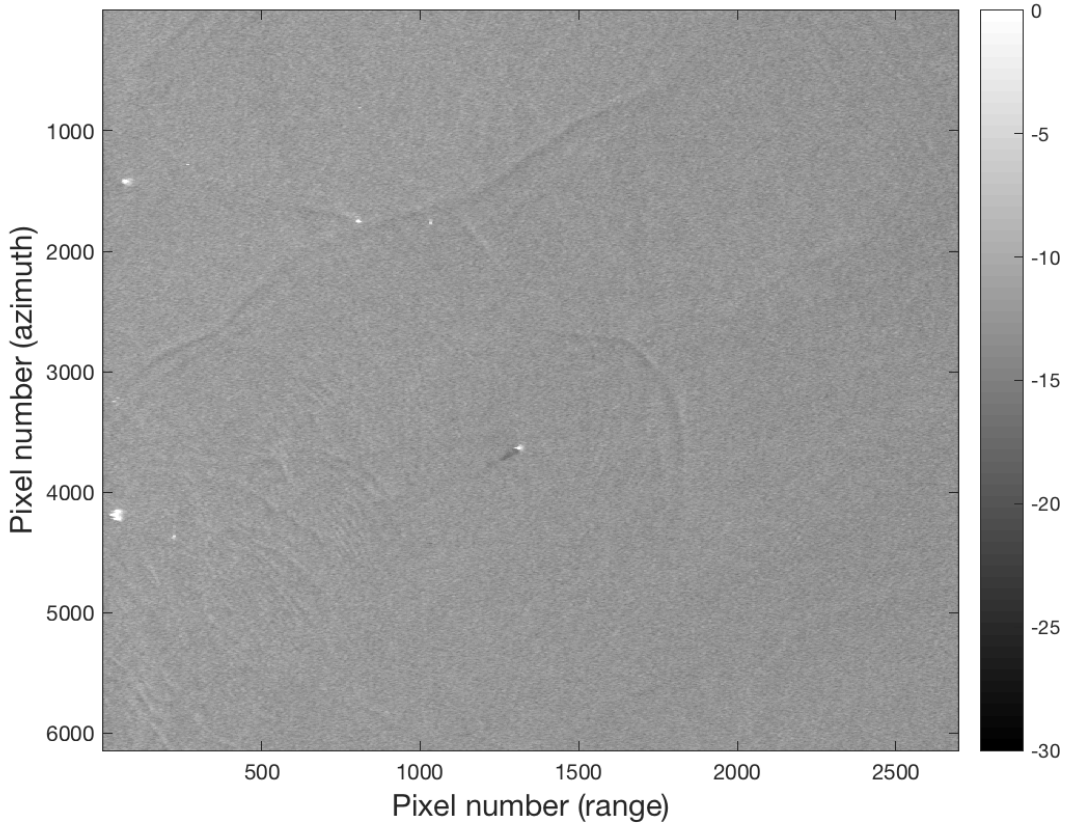

Figure 4.2: Radarsat-2 σ^0_{VV} fine quad-pol image of the Brage oil field. What is believed to be internal waves can be seen in the upper right corner of the image. Sheer zone areas can be seen around the oil platforms and ships (bright points). The Radarsat-2 data and Products © MDA LTD. 2018 – All Rights Reserved

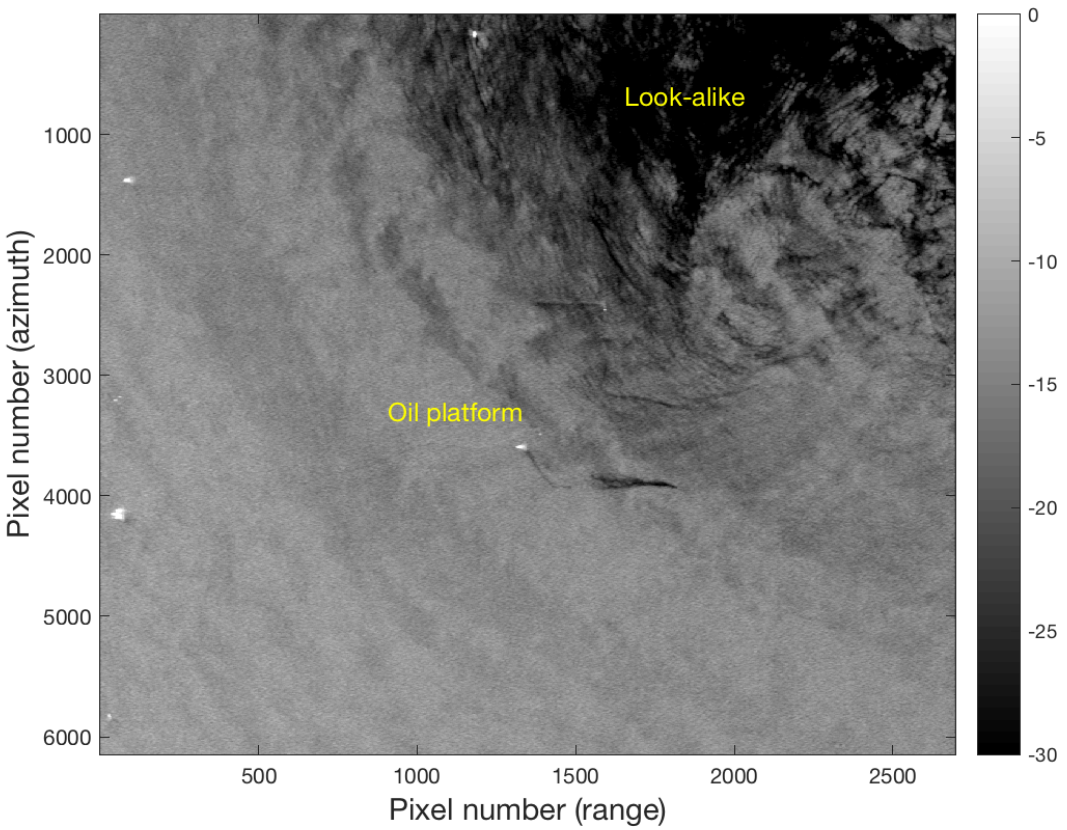

Figure 4.3: Radarsat-2 σ^0_{VV} fine quad-pol image of the Brage oil field. Produced water can be seen emanating from the platform in the center of the image. To the upper right of the image, a look-alike, most likely a biogenic slick of some origin, can be seen.

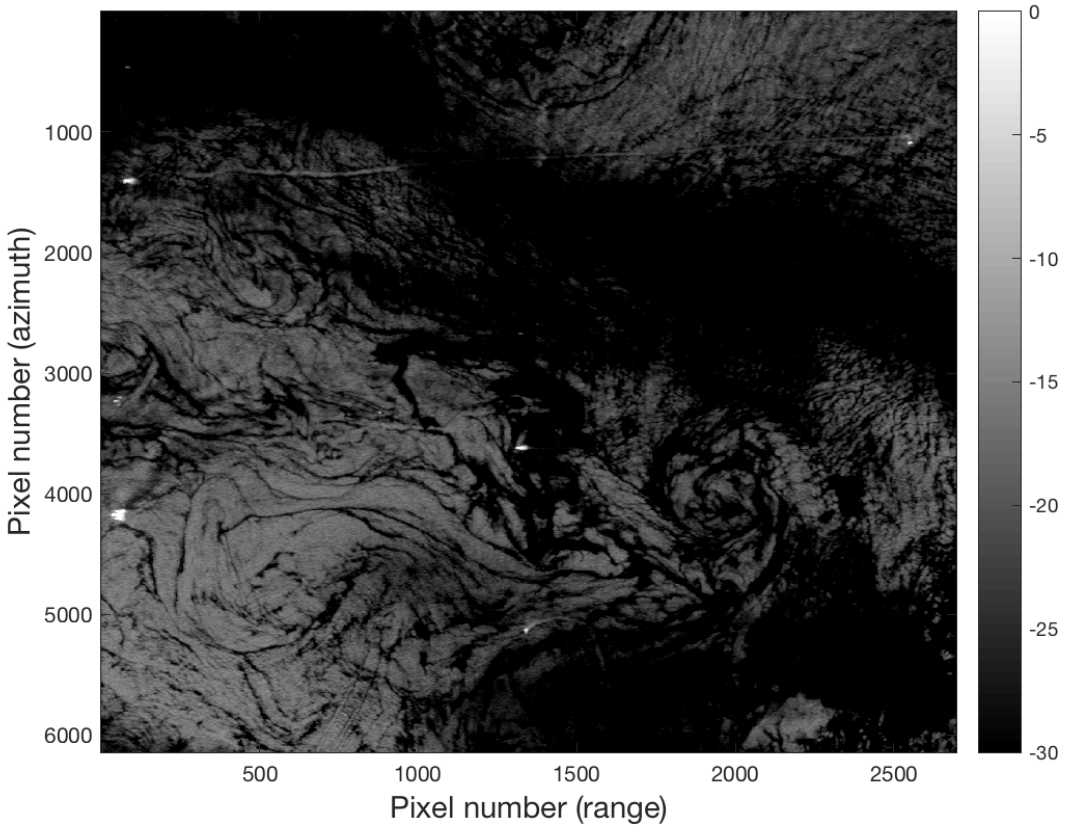

Figure 4.4: Radarsat-2 σ^0_{VV} fine quad-pol image of the Brage oil field completely infested with an oil spill look-alike, most likely biogenic material. The problem that look-alike phenomena can pose is evident.

- ***Natural biogenic slicks:*** Natural biogenic slicks are composed of substances that are released by plankton and fish and which accumulate at the ocean surface. These substances can accumulate in convergent zones by internal waves and current fields but will be mixed into the upper ocean and can rapidly disperse and disappear under wind action [Brekke, 2008]. This biogenic material can be problematic for the purposes of oil slick remote sensing. As an example of the effect these substances have on SAR imagery, Figures 4.3 and 4.4 shows two images of the Brage oil field. In the first image an oil platform can be seen in the center with produced water protruding from it. In the upper right of the image an area of what is believed to be biogenic slick. As an extreme example, Figure 4.4 shows the same scene that is completely infested with biogenic material on the ocean surface. As can be seen, deriving qualitative information form the scene with this level of look-alike present can be challenging under these circumstances. Given the ambiphilic structure of these natural compounds, a monomolecular layer is expected at the ocean surface [Hühnerfuss, 2006]. This indicates that they affect only the surface roughness of the ocean surface leaving the effective dielectric properties of the scattering surface unaltered.

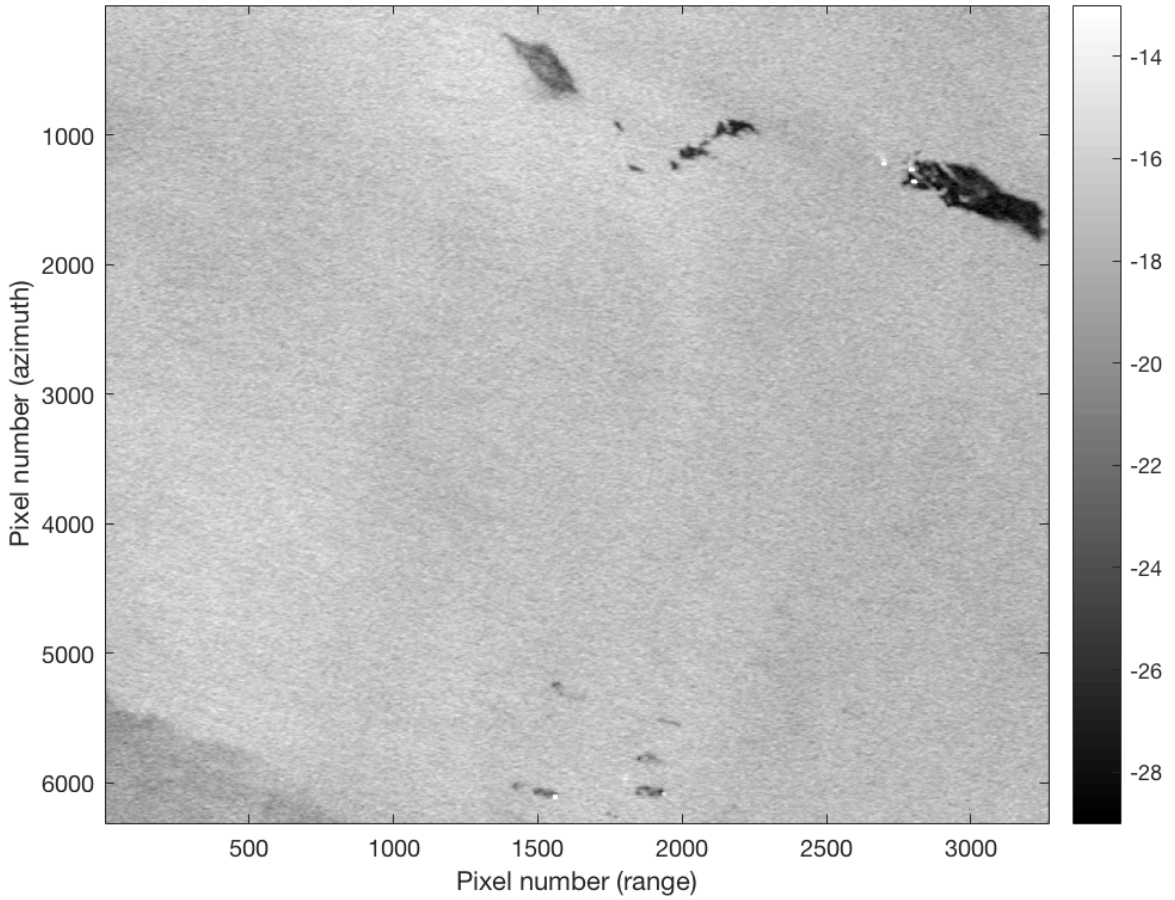

Figure 4.5: Radarsat-2 σ^0_{VV} fine quad-pol image of the 2011 oil-on-water exercise. To the upper right corner, the three slicks of discharged material (plant oil, mineral oil emulsion and pure crude oil as seen from left to right) can be seen. To the lower left, a dark area that is believed to be a region of low wind can also be seen. To the center foreground, what is believed to be fish oil from industrial activity can also be seen. The Radarsat-2 data and Products © MDA LTD. 2011 – All Rights Reserved

- ***Low Surface winds:*** In order for the radiation to be scattered back towards the SAR, there must be a degree of surface roughness present on the scale of the incoming radiation. In the case of the ocean surface, this roughness undulation is caused by the wind driven surface roughness. If there are areas on the ocean surface that do not have wind present, then forward scattering increases and that part of the imaged ocean surface can appear as a dark area. These dark areas can typically be seen on the leeward side of islands or other landmasses. An example of this type of look-alike can be seen in Figure 4.5, in the lower left of the image. This image was taken from the 2011 oil-on-water exercise conducted in the North Sea and shows the three discharged slicks in the top left of the image (more information about this can be found in paper 1). The lower left corner is believed to be an area of low wind due to the fact that wind speeds were measured to be between1.66 – 3.3 m/s.

- ***Rain cells:*** Rain cells may alter their appearance in SAR imagery via three distinct mechanisms. Firstly, there may be attenuation of the radiation in the rain column which may diminish the return to the sensor. There may also be an addition to scattering from the ocean surface that is roughened by the falling rain as well as there may be scattering from the rain itself. Finally, there can be an impact of the downward draft associated with the rainfall on the ocean surface. This increased near surface wind will act to modulate the ocean surface roughness and thus the backscattered signal [Kasilingam et al., 1997]. C-band tends to be affected more by rain volume scattering while L-band sensors are more sensitive to Bragg wave dampening by the rain [Brekke, 2008].

- ***Sheer zones:*** These are narrow, bright or dark features that can appear in SAR imagery. These features can appear in areas where there is strong current [Brekke, 2008]. Again, it is believed that Figure 4.2 is showing these sheer zone areas in the vicinity of the oil rigs which are seen as bright areas in the image.

These look-alike phenomena are dependent on specific atmospheric conditions. Table 4.1 shows the various wind conditions that need to be present in order for these features to manifest themselves as well as typical values for a reduction in returned backscatter due to damping that they can cause.

Table 4.1: Atmospheric conditions needed for the presence of low-backscattering look-alike phenomena. Taken from [Brekke, 2008].

Phenomenon	Weather limitations	Damping [dB]
Oil slick	Wind Speed <= 15 m/s	0.6 – 13.0
Biogenic film	Wind Speed <= 7 m/s	0.8 – 11.3
Grease ice	Cold temperatures and close to ice edge	14.0 –19.0
Area of low wind	Wind Speed <= 3 m/s	9.6 – 18.5
Sheer zones	Wind Speed <= 10-12 m/s	1.4 –6.2
Internal waves	Wind Speed <= 8 m/s	0.8 – 6.0

4.3 Oil Slick Weathering Processes and Characterization: Brief Overview

The following subsections will provide the reader with a brief overview of the entire field of oil slick characterization. First the processes that crude oil undergoes when subjected to the marine environment, collectively referred to as weathering will be discussed. This is then followed by current methods and trends in which oil slick is characterized and detected in SAR imagery.

4.3.1 Weathering

Weathering refers to the processes that crude oils will undergo when released into the marine environment. Such processes include evaporation, emulsification, spreading, dissolution, dispersion, oxidation and biodegradation. These processes alter the physical and chemical characteristics of the slick. Other factors such as the type of oil present and ocean water conditions have an effect of the weathering process also. The relative contribution of each mechanism tends to change with time. In the following, the most relevant processes that are pertinent for the papers presented in this thesis are presented.

Emulsification is the formation of various states of water-in-oil mixtures. As the water content of the oil increases, the density and viscosity also increase. The amount by which the viscosity can increase can be of orders of magnitude. The processes of emulsification contributes to the persistence of oil slicks in the marine environment [ITOPF, 2002].

Spreading refers to the process by which freshly spilled oil moves over the ocean surface. Oil that is freshly spilled will not spread uniformly but will tend to form areas of thinner and thicker regions. This has consequences for the estimation for volumetric oil content after a major spill. A simple heuristic that is often cited is that 90% of the oil is often contained within 10% of the slick [Hollinger and Mennella, 1973]. The viscosity of the oil has an effect on the amount of spreading that will occur. This then can have an influence on the interaction between radiation from the SAR and the scattering surface.

Figure 4.6 illustrates the processes of emulsification that a surface-dwelling slick can be subjected to. Figure 4.7 illustrates the relative importance of each weathering process by the thickness of each band at an approximate point in time, indicated on the x-axis on the top of the image. As can be seen from this image, evaporation and spreading are primary mechanisms that

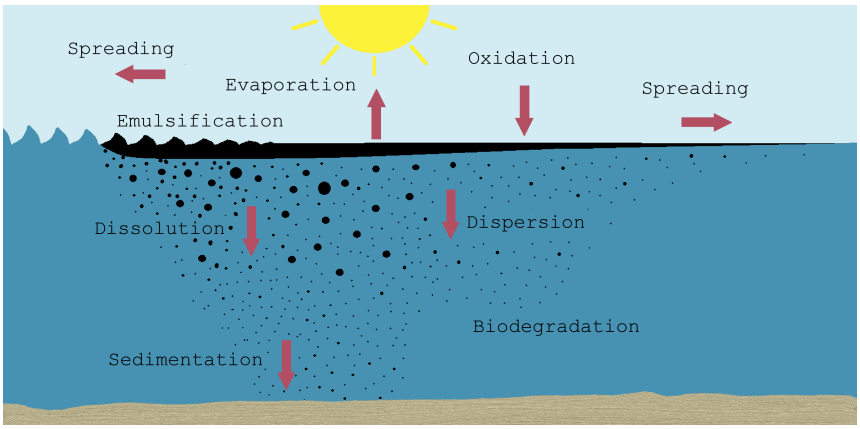

Figure 4.6: The various weathering processes which act on surface dwelling oil slicks. Figure taken from [Espeseth, 2019] and adapted from [ITOPF, 2002].

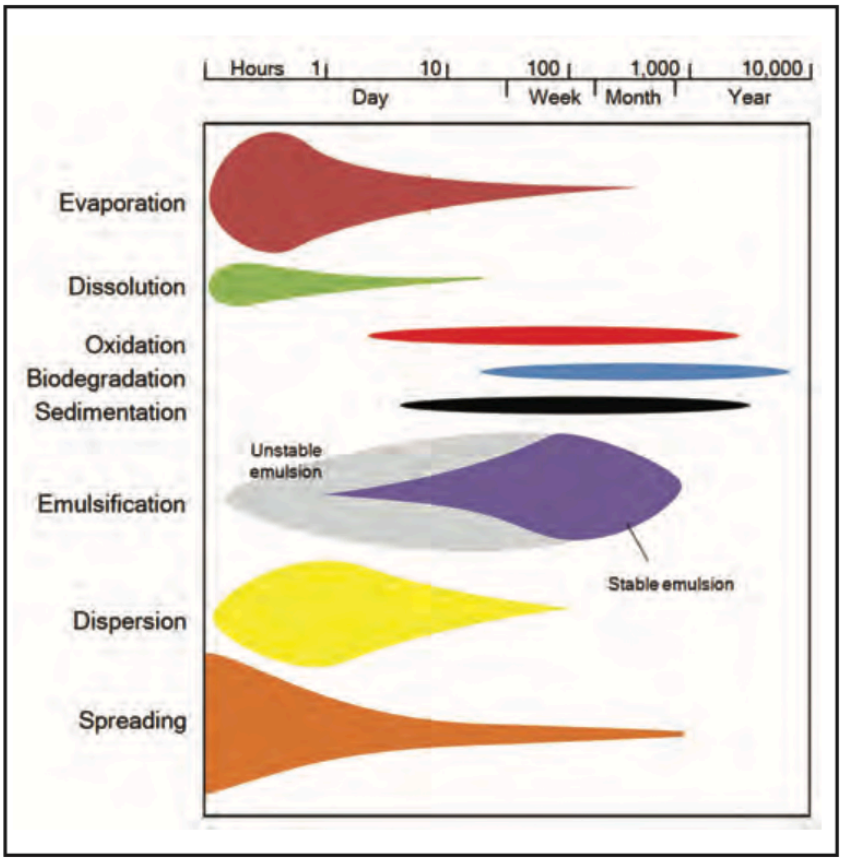

Figure 4.7: Schematic showing the fate of a typical oil spill with time. The width of each band indicates the relative importance of each weathering process over time. Taken from [ITOPF, 2002].

occur in the first hour of a spill, with dispersion and emulsification then becoming the most relevant weathering processes within the first tens of hours of an oil spill.

4.3.2 Bonn Agreement

The Bonn agreement is a European environmental agreement that was established in 1969 for the purposes of responding to pollution in the North Sea and to assure active cooperation and mutual assistance between members. One aspect of the Bonn agreement was the implementation of the Bonn Agreement Oil Appearance Code (BAOAC) which is a series of thickness designations to oil slicks for the purposes of characterization based on their optical appearance. The BAOAC was developed in accordance with scientific literature and is supported by small scale laboratory experiments and mesoscale outdoor experiments and sea trials [Bonn Agreement Secretariat, 2016]. The five levels of oil appearances are detailed below in Table 4.2.

Table 4.2: BAOAC thickness classifications. Taken from [Bonn Agreement Secretariat, 2016].

Code	Description - Appearance	Layer Thickness Interval (µm)	Litres per km^2
1	Sheen (silvery/grey)	0.04 to 0.30	40 – 300
2	Rainbow	0.30 to 5.0	300 – 5000
3	Metallic	5.0 to 50	5000 – 50,000
4	Discontinuous True Oil Colour	50 to 200	50,000 – 200,000
5	Continuous True Oil Colour	More than 200	More than 200,000

It should be noted however that the appearances cannot be related to solely one thickness regime as they are optical effects (codes 1-3) or true colours (codes 4-5) that appear over a range of thicknesses. There is no sharp delineation between one specific designation and another. One effect becomes more diffuse as the other strengthens [Bonn Agreement Secretariat, 2016]. Because of this, a certain degree of subjective interpretation is required when applying the codes.

4.3.3 Polarimetric Features

Currently, operational services rely heavily on single polarization SAR imagery for identifying and characterizing oil spills. For this purpose, auxiliary features such as shape and geometry of a slick, the oil to sea contrast, wind information, relative position of ships and oil rigs and texture are used to infer information of an oil spill event [Brekke and Solberg, 2005]. However, over the last decade and a half, multipolarimetric SAR data has been extensively investigated for oil spill research [Skrunes et al., 2017].

As already stated, oil slicks appear as dark patches in SAR imagery. The contrast between slick and open water is controlled by various factors relating to sensor properties like frequency, polarization, incidence angle, oil slick characteristics, weathering processes and environmental conditions [Espeseth, 2019]. The two primary characteristics of the ocean surface that are affected by the presence of oil are the small-scale surface roughness and dielectric properties. Both factors can result in a reduction of backscatter to the SAR. For the purposes of deriving more quantitative information about the internal conditions of oil slicks, polarimetric features have proven useful. [Espeseth, 2019] provides a brief yet comprehensive literature review on the use of polarimetric features in SAR remote sensing in recent times.

4.3.4 Co-polarization Power Ratio

The co-polarization power ratio, R_{co-pol}, forms a significant basis for the work presented in this thesis and so will be outlined here. According to [Skrunes et al., 2014] this feature is the ratio between the mean squared amplitudes (mean intensities) of the complex scattering coefficients in the VV and HH channels and is defined as

$$R_{co-pol} = \frac{\langle |S_{VV}|^2 \rangle}{\langle |S_{HH}|^2 \rangle} \tag{4.1}$$

See section 2.5 for a more thorough treatment on the scattering matrix. In two-scale surface scattering models, the co-polarization ratio is independent of the damping of gravity-capillary waves by oil and is only a function of the dielectric properties, the slope of the scattering facets which are modulated by the large-scale ocean roughness (this is unaffected by oil) and the incidence angle of the sensing radiation. The effect of oil slick on the short-scale roughness undulations of the ocean surface can be seen in Figure 4.8. As can be seen, the variations of the large-scale roughness between open water and oil slick are largely preserved.

For this reason, a reduction in backscatter from oil-infested regions is partially due to differences in the dielectric properties of the scattering surface [Minchew et al.,2012]. [Skrunes et al., 2017] compared C-band RISAT-1 SAR data with thermal IR data collected from an aircraft operated by the Finnish Border Control during an oil-on-water exercise in the North Sea in 2016. They found that the IR data, specifically internal areas that were observed to be

Figure 4.8: Image showing the change in surface roughness between areas of open ocean and slick infested areas. As can be seen, small-scale undulations are less prevalent within the slick but large-scale surface undulations are preserved across both scattering surfaces. Taken from [ITOPF, 2011 (a)].

thicker, correlated well with the co-polarization ratio. This indicates that the co-polarization ratio may be able to detect internal areas that are thicker/more concentrated with oil.

5 Overview of Publications

This chapter will serve to provide an overview of the three publications presented in chapters 6-8.

5.1 Paper I

C. Quigley, C. Brekke, T. Eltoft, **"Retrieval of Marine Surface Slick Dielectric Properties from Radarsat-2 Data via a Polarimetric Two-Scale Model",** *IEEE Trans. Geosci. Remote Sens.*, vol. 58, no. 7, pp. 5162-5178, July 2020.

This paper presents a methodology for estimating $|\varepsilon|$ the absolute value of the dielectric permittivity of oil slick via the use of a Polarimetric Two-Scale Model (PTSM). The model was chosen as it builds upon other, well established models used for the purposes of volumetric moisture content of a scattering surface, e.g. the XBragg model. Details about the PTSM and the XBragg can be found in chapter 3.4.3.

In this paper, Radarsat-2 data (four scenes in total containing nine individual slicks of biogenic simulator and oil emulsion/crude oil) from three oil-on-water exercises, conducted in the North Sea during the summer months of 2011, 2012 and 2013 are presented and inverted into their $|\varepsilon|$ values. Other studies [Skrunes et al., 2014], explicitly demonstrate that the cross-polarization channels within Radarsat-2 data are not applicable for marine satellite remote sensing given the highly non-depolarizing nature of the ocean surface and the relatively high noise floor of the spaceborne sensor. The result is two polarimetric bands (HV and VH) that are highly corrupted with internal system noise. For this reason, only the two co-polarization channels are utilized in the inversion procedure.

The co-polarization ratio is employed resulting in an equation that is primarily dependent on two unknowns, i.e. $|\varepsilon|$ and a large-scale roughness descriptor (in reality the model equation describing the co-polarization ratio are dependent on four unknowns, the two already cited, the incidence angle of the radiation and the Hurst coefficient, a quantity related to the fractal dimension of the scattering surface. However, the incidence angle can be determined from the header file accompanying the data and so does not need to be estimated. The Hurst coefficient has been shown to not have a strong effect on the model by [Iodice et al., 2011] and so can be substituted with a nominal value.)

A method for determining the large-scale roughness descriptor is presented in this paper and is based on using the surrounding areas of clean open ocean, immediately adjacent to the slick.

While there is no in-situ ground truth data with which to compare the inversion results against, the results are as expected and are realistic based on the individual times and atmospheric conditions the slicks were acquired at, i.e. all slicks showed a majority of pixels around the 2.3 value (the theoretical dielectric value for pure crude oil.)

One notable issue was the apparent underestimation of some pixels below the value of 2.3. This indicates that the model is able to only approximate accurate values for $|\varepsilon|$.

5.2 Paper II

C. Quigley, C. Brekke, T. Eltoft, "**Comparison Between Dielectric Inversion Results from Synthetic Aperture Radar Co- and Quad-Polarimetric Data via a Polarimetric Two-Scale Model",** *IEEE Trans. Geosci. Remote Sens.*, 2020, (in Early Access).

This paper is a direct continuation from the work presented in Paper I. In this paper, data from the NORSE2019 oil-on-water experiment is presented in the form of fully quad-polarimetric SAR data acquired with F-SAR, an airborne instrument which acquired data in X-, S- and L-bands.

Given that this is an airborne instrument with a relatively low noise floor, data in the cross-polarization channels should not be corrupted by sensor noise and be available for use. A noise analysis presented in this paper showed that only the L-band data contains a majority of pixels available in the cross-polarization channels and so only the L-band acquisitions were used in the analysis of this paper.

Given that the cross-polarization information is available, this presents an opportunity to apply the PTSM by utilizing the co-polarization channels in conjunction with the cross-polarization channels. By doing this, a series of look-up tables can be constructed, and simultaneous values for $|\varepsilon|$ and the large-scale roughness descriptor, s, can be determined in a pixel-wise fashion. This method is assumed to be more accurate than the method presented in Paper I as assumptions about the large-scale roughness descriptor don't have to be made and can be determined numerically.

In this paper, two L-band acquisitions taken by the FSAR instrument during the NORSE2019 campaign are inverted into $|\varepsilon|$ values, first by using only the co-polarization channels, and then by using the co-polarization as well as the cross-polarization channels. The inversion results are compared against each other and show that the two methods are equivalent for low values of $|\varepsilon|$. The results are compared to photographs taken both from the aircraft carrying the F-SAR instrument as well as from the research vessel that discharged the mineral oil emulsion.

5.3 Paper III

C. Quigley, C. Brekke, T. Eltoft, **"Analysis of the Dielectric Retrieval Capabilities of Simultaneous X- S- and L-band Airborne Synthetic Aperture Radar for Oil Spill Monitoring Applications ",** *IEEE Trans. Geosci. Remote Sens,* 2020, (Manuscript submitted).

As already stated, in order to derive estimates of $|\varepsilon|$ for an oil slick, the co-polarization ratio has proven to be of immediate interest. In this paper we investigate the dielectric retrieval abilities of the F-SAR instrument which acquired multifrequency and multitemporal SAR data in X-, S- and L-bands. The noise characteristics of each frequency band are analyzed where it was found that X-band is not suitable for this application due to noise corruption of the data.

A new polarimetric feature we call *the incidence angle normalized sum of co-polarization ratios* is also proposed in this paper which aims to combine the dielectric information contained in the co-polarization ratio from each frequency band, while also removing the variation in of the proposed feature due to incidence angle across the range direction. The result is an oil concentration map which provides an indication of the areas within slick that contain a greater amount of oil in contrast to other areas. The multitemporal aspect of this data set is then

exploited by applying a stability measure to this feature. The result is a map which shows areas within the slick that consistently contain more oil over time.

We conclude this paper by making recommendations to the oil spill contingency community and emphasize the benefits of simultaneous S- and L-band airborne SAR for this application, but recommend that the experiment is performed again using simultaneous C-, S- and L-band.

Chapter 6

Paper 1:

Retrieval of Marine Surface Slick Dielectric Properties From Radarsat-2 Data via a Polarimetric Two-Scale Model

Chapter 7

Paper 2:

Comparison Between Dielectric Inversion Results From Synthetic Aperture Radar Co- and Quad-Polarimetric Data via a Polarimetric Two-Scale Model

Chapter 8

Paper 3:

Analysis of the Dielectric Retrieval Capabilities of Simultaneous X- S- and L-band Airborne Synthetic Aperture Radar for Oil Spill Monitoring Applications

Analysis of the Dielectric Retrieval Capabilities of Simultaneous X- S- and L-band Airborne Synthetic Aperture Radar for Oil Spill Monitoring Applications

Cornelius Quigley, Camilla Brekke, *Member, IEEE*, Torbjørn Eltoft, *Member, IEEE*

***Abstract*— In addition to the incidence angle, the co-polarization ratio is a quantity that depends primarily on two unknowns, the first being the relative permittivity of the scattering surface and the second being the standard deviation of the distribution of surface facet slopes, which are an indicator of the large-scale roughness of the ocean surface in the tilted Bragg model. By investigating the co-polarization ratio, and deriving estimates for the electric permittivity of the scattering surface via the application of theoretical backscattering models, an indication of the volumetric content of oil within a pixel can be determined. In this study we examine a time series of data acquired using airborne multifrequency synthetic radar acquired in X-, S- and L-band. We provide an in-depth analysis on the dielectric retrieval capabilities of each polarimetric band and demonstrate that X-band is inadequate for this application in an operational setting primarily due to noise corruption. We then propose a polarimetric feature that is capable of combining the co-polarization ratios into one product, which is capable of highlighting internal zones of more concentrated oil, better than the application of just one frequency band alone. We conclude the paper by taking advantage of the temporal aspect of the data set and conduct a stability analysis, which relies on a time series of the data, by employing the proposed feature, in order to determine regions within the slick where zones of constant concentration over time are located. We conclude the paper by making recommendations to the oil spill contingency community.**

***Index Terms*—dielectric properties, oil spill, surface slick characterization, synthetic aperture radar**

I. Introduction

Synthetic Aperture Radar (SAR) instruments have become a key operational monitoring tool for the detection and surveillance of marine surface dwelling mineral oil slicks. Currently, operational services who work to detect and characterize mineral oil spills and extract relevant information such as location, extent and the source of oil, if possible, do so by analyzing single polarization SAR imagery [1].

However, methods for quantifying the internal characteristics of oil slick as well as their internal variations are still in their infancy and are not widely adopted by operational services. Current methods that are employed to determine the thickness variations of oil slick when major spill events occur, rely heavily on subjective methods such as the Bonn Agreement Oil Appearance Codes (BAOAC) for aerial observers of oil spills [2]. A major drawback to such methods is that they are subjective in nature and do not provide a wide-scale, synoptic assessment on the state of a slick. Given that some oil spills can be many kilometers in scale, remote sensing technology, both spaceborne and airborne, has proven itself to be a valuable technology for this application.

Current research has hinted at the capability of SAR to discern marine oil slick physical characteristics such as volumetric oil content and thickness. Skrunes et. al. [3] for example, used airborne infrared imagery, which is believed to be sensitive to thickness variations within slick, to suggested that it is correlated with SAR imagery.

Pure mineral oil, before it is subjected to weathering processes, has a relatively low dielectric constant. According to [4] – [6] the value for the real part of the dielectric constant for pure crude oil, over the frequency range 0.1 – 10 GHz can range between 2.2 and 2.35 and with an imaginary part less than 0.02. As oil mixes with sea water, emulsions can form that will have dielectric values intermediate to that of pure crude oil and pure sea water (sea water having a real part of the dielectric constant over 60 for the same frequency range and an imaginary component greater than 40). Therefore, the value of the dielectric constant can serve as an indication for the volumetric content of oil within a pixel and can be inverted via the use of an appropriate mixing model.

Quigley et. al. [7] applied a polarimetric two-scale model (PTSM), developed by [8], to satellite mounted SAR imagery of verified oil slick for the purposes of determining the absolute value of the dielectric constant of oil within slick, $|\varepsilon|$. The model, which is capable of modeling both the co-polarization and cross-polarization channels could only be applied to the data by utilizing the co-polarization ratio, resulting in an equation with two primary unknowns, i.e. $|\varepsilon|$ and s. The quantity s, is the

This work was supported by CIRFA, CIRFA partner Total E&P Norge AS and the Research Counsel of Norway under Grant 237906.

C. Quigley, T. Eltoft and C. Brekke are with the Department of Physics and Technology, UiT – The Arctic University of Norway, NO-9037 Tromsø, Norway (e-mail: cornelius.p.quigley@uit.no, torbjorn.eltoft@uit.no, camilla.brekke@uit.no).

Manuscript received ____

standard deviation of the distribution of the slopes of the surface facets and whose explanation can be found in [7] and [8] and which acts as a descriptor of the large-scale roughness variation of the scattering surface. The co-polarization ratio could not be modeled as the cross-polarization channels were redundant due to noise corruption. Consequently, the *s* values were determined from areas of open ocean immediately adjacent to the slick.

Quigley et. al. [9] conducted a study where they compared the $|\varepsilon|$ values obtained from using the full PTSM model, i.e. by employing both the co- and cross-polarization ratios against the retrieval results obtained by using only the co-polarization ratios. The model was applied to quad-polarimetric data sets acquired by Deutsches Zentrum für Luft- und Raumfahrt (DLR) F-SAR instrument in L-band acquired throughout the NOrwegian Radar oil Spill Experiment in 2019 (NORSE 2019) led by the Centre for Integrated Remote Sensing and Forecasting for Arctic Operations (CIRFA) as an embedded part of the Norwegian Clean Seas Association for Operating Companies (NOFO) annual oil-on-water campaign. The experiment was conducted in the North Sea in June 2019. F-SAR is an airborne instrument that has the capability to acquire data with a low level of noise corruption, resulting in data sets with high signal-to-noise ratios (SNR), thus allowing for the cross-polarization channels to be fully modeled. The authors found that retrieval results for $|\varepsilon|$ were consistent across both methods, i.e. by estimating $|\varepsilon|$ by using only the co-polarization channels, and by estimating $|\varepsilon|$ by using both the co- and cross-polarimetric channels, low values of $|\varepsilon|$ were similar, but differed at higher values. They concluded that the reason was due to uncertainties in estimated *s* values. It should be noted that the F-SAR instrument acquired data in X-, S- and L-bands, but due to the noise characteristics of the data in the cross-polarization channels, only the L-band data was included in their analysis.

In the absence of cross-polarization data, there have been methods presented to attempt to derive numerical values for the dielectric constant by employing the co-polarization ratio in conjunction with the correlation coefficient between the co-polarization channels. Iodice et. al. [10] proposed such a scheme whereby the aforementioned quantities were modelled, and a series of look-up graphs established, whereby both values for the dielectric constant and the large-scale roughness of the scattering surface can simultaneously be determined. The drawback is that complex SAR data is required, which may not always be available.

In this paper, we investigate the viability of using the F-SAR instrument for the purposes of deriving $|\varepsilon|$ values of oil slick. As already hinted, $|\varepsilon|$ can act as a proxy for the volumetric content of oil within a pixel and can provide a synoptic indication about the amount of oil present in a spill event, which is valuable for clean-up efforts and later for legal reasons.

However, given the disparity that can be displayed in backscatter measurements made by SARs of varying wavelengths from the same scattering surfaces, this study will attempt to illustrate the advantages with using multifrequency SAR for operational oil spill monitoring with a particular emphasis on the retrieval of $|\varepsilon|$ values within slick. For this purpose, we will make use of a unique data set, which will be elaborated in in section II, which consists of simultaneous imagery in X-, S- and L-bands. We then make recommendations for the operational oil-spill contingency community based on our analysis. As a second original contribution of this study, we investigate the possibility of deriving volumetric oil concentration maps based on multifrequency airborne SAR imagery. The concentration maps are derived from the co-polarization ratio of the SAR data and are based on a parameter we propose called the *Incidence angle normalized sum of co-polarization ratios*. This parameter combines the information contained in the co-polarization ratios of each frequency band and takes advantage of the fact that radiation with different wavelengths will have varying backscatter responses depending on the thickness of the oil layer being sensed. The proposed parameter is simple and generic enough to be implemented in an operational setting in, in near real time, and requires no specialized knowledge in terms of modelling, in addition to being computationally simple to implement.

A third original contribution of this paper is a stability analysis we present, that is based on the time series of the data, and necessitates the use of the parameter introduced in this study. This is due to the expansive incidence angle range of the F-SAR data as will be shown in section II.

This paper is organized as follows, section II will briefly introduce the data sets collected during the NORSE 2019 oil-on-water experiment, as well a thorough noise analysis that is used to determine appropriate data acquisitions to be used in this study. Section III will introduce the reader to the concept of polarimetric ratios and Section IV will introduce the new feature that is based on the combination of polarimetric ratios from different frequency bands as well as the stability analysis. Section V will conclude the paper with a discussion.

II. Experimental setup and data acquisition

The following subsections provide a brief overview of the data sets used in this study followed by an in-depth noise analysis. For a more thorough treatment on the F-SAR instrument the reader is directed to [9]. For a more in-depth treatment on the NORSE 2019 oil-on-water experiment the reader is directed to [11].

A. Data set

The data used in this paper was acquired during the NORSE 2019 oil-on-water experiment conducted in the North Sea (N 59° 59', E 2° 27') on 12 June 2019. During the campaign 26 separate fully quad-polarimetric acquisitions were made by DLRs airborne F-SAR instrument over the course of 2 flights in X-, S- and L-bands.

The F-SAR instrument is mounted on a Dornier DO228-212 aircraft and can operate in X-, C-, S-, L- and P-bands with bandwidths of 760, 400, 300, 150 and 100/50 MHz, respectively. The total frequency range of the instrument is 0.35-9.6 GHz [12]. F-SAR is capable of transmitting and receiving in both vertical (V) and horizontal (H) polarimetric configurations, resulting in imagery in HH, HV, VV and VH polarization channels, and is capable of acquiring simultaneous imagery within different frequency bands. For regular Earth observation purposes, the radar is capable of acquiring imagery at off-nadir look angles in the ranges between 25° to 60° at

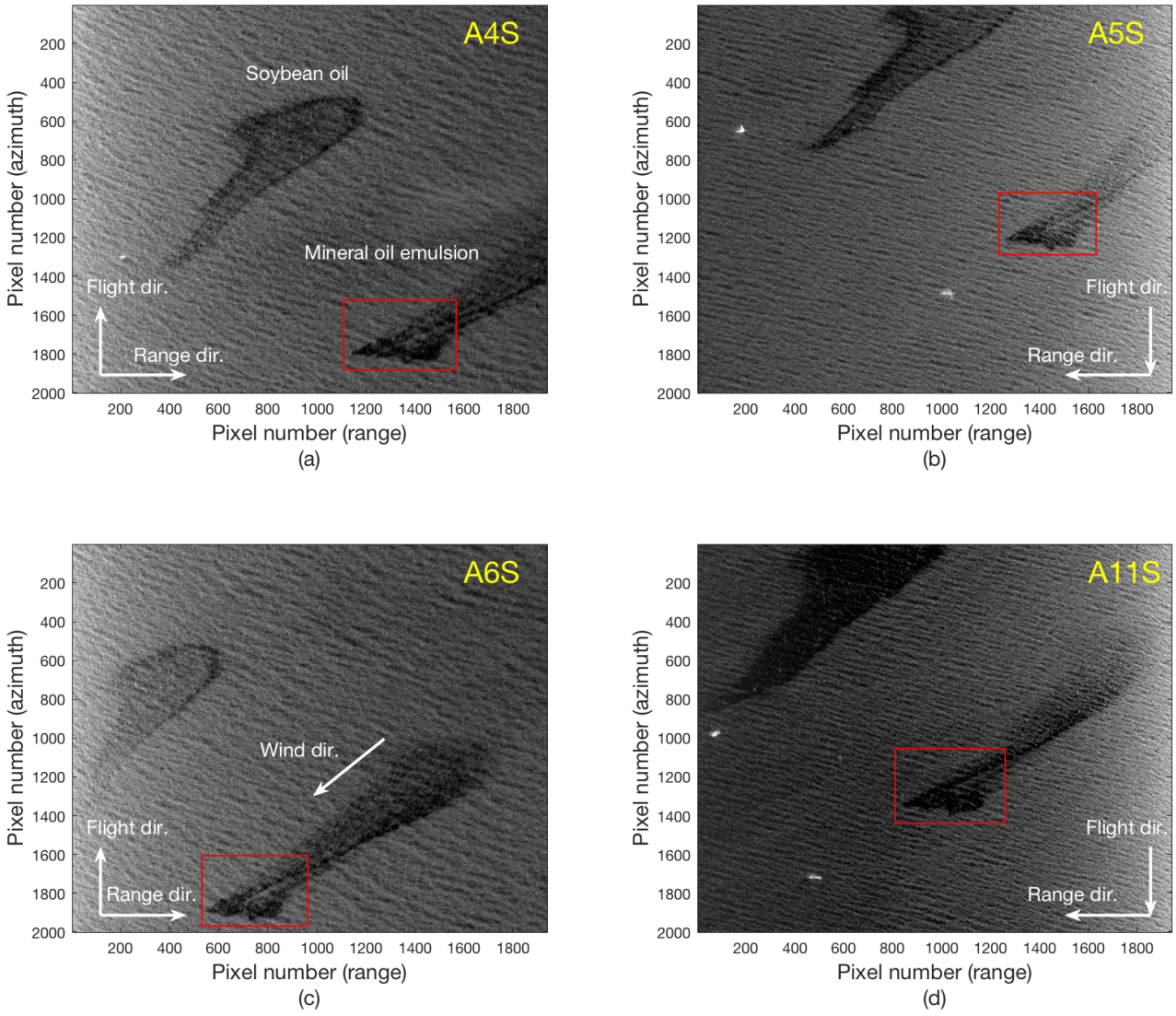

Fig. 1 S-band intensity images ($\sigma_{0VV}\,[dB]$) multi-looked by 9 × 9 window for (a) the A4S acquisition (b) the A5S acquisition (c) the A6S acquisition and (d) the A11S acquisition. The regions of interest that are considered in this study are indicated by a red box.

flight altitudes up to 6000m above sea level. This is the maximum operating altitude of the DO228-212 aircraft [12].

The first flight occurred between 05:12 - 06:33 UTC and acquired 12 acquisitions while the second flight occurred between 10:50 – 12:17 UTC and acquired 14 acquisitions. Fight 1 acquired data while the mineral oil emulsion and soybean oil were actively being discharged at times of 05:30 – 05:54 UTC and 06:20 – 06:37 UTC, respectively. As a result, the mineral oil emulsion and soybean oil are confined to a small area on the ocean surface and are not present in all 12 acquisitions of flight 1, indicating that a time series constructed using data from this flight would be quite restrictive. As a consequence, scenes from flight 1 are not considered for analysis in this study.

In this study we refer to nine acquisitions that were acquired during flight 2. The main criteria for choosing these specific scenes was to choose scenes where the oil slick had an incidence of angle of 35° or greater within the scene. Incidence angles less than 35° are not considered as the sensitivity of the radar to small-scale roughness undulations is low under this threshold. This violates the small perturbation assumption under which many theoretical backscattering models which are used to invert the returned backscatter into values of $|\varepsilon|$, were derived [5], [13], [14].

Note, the actual oil slick observed throughout the exercise was large in extent. In this paper we restrict ourselves to studying the 'head' of the slick, i.e. the portion of the slick where most of the oil congregated directly downwind. In the following, when we refer to the 'oil slick', we are referring to the 'head' of the slick.

Table 1: List of all SAR acquisitions made during flight 2. Acquisitions that had appropriate incidence angle values were chosen for further analysis and are indicated in green. Red indicates acquisitions that were not chosen. Reasons why are also provided. The acquisitions that are displayed in Fig. 1 are indicated by grey shading.

	Chosen for further analysis
A2	Head of slick not visible in co-pol ratio for S-band
A3	
A4	Acquisition not similar to others
A5	Acquisition similar in appearance to A3
A6	Acquisition similar in appearance to A8, A10, A14
A7	
A8	
A9	Head of slick not in acquisition
A10	
A11	Acquisition similar in appearance to A7
A12	Head of slick not in acquisition
A13	Incidence angle of slick head below 35°
A14	
A15	Incidence angle of slick head below 35°

In Table 1, those scenes which satisfy this incidence angle condition are marked in green while those that do not are marked in red. A specific reason for not choosing a particular acquisition is also indicated in Table 1.

It should be noted that 14 scenes were collected in flight 2 but the naming convention begins at 2, i.e. the first data set collected is referred to as data set 2, the second is referred to as data set 3 etc. In order to keep this paper consistent with future publications, the same naming convention that was adopted for the data set collected in flight 2 is applied here. In short, there is no data set 1.

In subsequent sections, the following notation will be adopted. The image of the mineral oil emulsion slick that was acquired first will be referred to as A2 (i.e. Acquisition 2), the second SAR acquisition will be referred to as A3, the third as A4 etc. Specific frequency acquisitions will be delineated with the suffix -X, -S or -L. This indicates that A2X refers to the X-band acquisition of A2, and A3S refers to the S-band acquisition of A3 etc. This is due to the fact that within each acquisition, there are three simultaneous images corresponding to X-, S- and L-band respectively.

Note, to make it easier for the reader, the specific acquisition that each individual image refers to in the following sections is indicated in the corner of each image where applicable.

It should be noted that the A2 acquisition is not included in this study as the co-polarization ratio showed no contrast between slick infested areas and open water in S-band, but did show contrast in the X- and L-bands. This is atypical behavior and will not be addressed in this study.

Information concerning these nine acquisitions as well as in-situ information can be found in the Table 2. Fig. 1 shows the VV S-band imagery for the acquisitions of A4S, A5S, A6S and A11S. Note, the corresponding X- and L-band imagery have the same appearance, and so have not been shown here in order to save space. In these four images, the entire acquisition can be seen, but the region of interest that is addressed in this study,

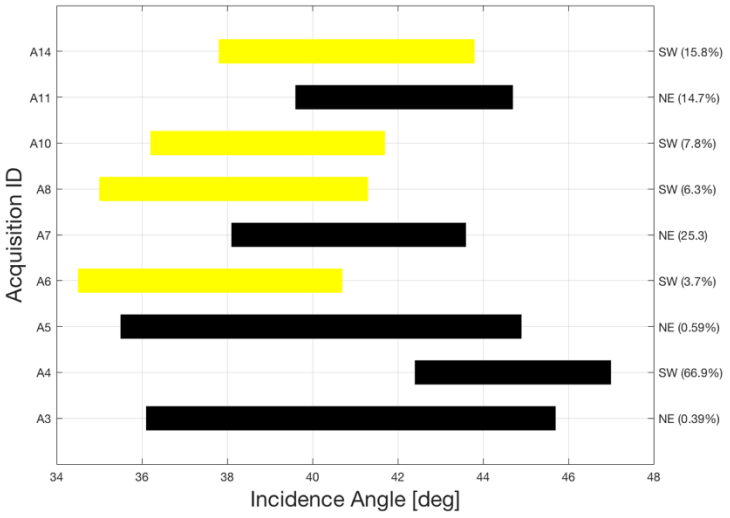

Fig. 2 Graph showing the incidence angle range of each of the acquisitions considered in this study. The flight direction and the proportion of pixels within the entire region of interest with suitable SNR is indicated on the right. The acquisitions highlighted by a yellow bar will be discussed in section II.C.

i.e. the head of the slick of mineral oil emulsion, is outlined by a red box in all four images. The other slick that can be observed is the soybean oil slick. Table 1 indicates the acquisitions that are shown in Fig. 1 as well as the other acquisitions that have a very similar appearance to these acquisitions in terms of the positioning of the mineral oil slick in the range direction. For this reason, those acquisitions that are indicated as having similar appearance to those depicted in Fig. 1 are not shown in order to save space. These 4 acquisitions, as shown in Fig. 1, were chosen to show the difficulty in working with the entire mineral oil emulsion slick. As can be seen in Fig.1(a) and (b) the 'tail' of the slick runs off the image, while the tail lies in a high incidence angle range of the image in Fig.1 (c), indicating it may be too corrupted with noise, and correspondingly lies in a very low incidence angle range of the image in Fig.1 (d) indicating this region of the slick may violate the 35° incidence angle rule previously stated. The wind direction is indicated in Fig.1 (c) but still retains its relative direction in the other three images. Fig. 2 demonstrates the incidence angles over which the regions of interest lie for all 9 acquisitions. As can be seen, some of the scenes have a larger span in incidence angle values than others. The color coding for this graph will be explained in section II.C.

In total, 2 m^3 of mineral oil emulsion was discharged onto the ocean surface. The discharged emulsion was composed of 45% oil (10 parts evaporated Oseberg Blend and 1 part IF0 380) and 55% sea water. The viscosity was between 1500 – 1600 mPa·s. IFO 380 refers to Intermediate Fuel Oil with viscosity ≤ 380 cSt (<3.5% Sulphur) [9].

Table 2: Properties of SAR acquisitions and in-situ information.

Scene ID	**A3**	**A4**	**A5**	**A6**	**A7**	**A8**	**A10**	**A11**	**A14**
Time (UTC) of acquisition	10:57	11:03	11:09	11:16	11:22	11:30	11:42	11:49	12:11
Incidence angle (at emulsion slick)	36.1° - 45.7°	42.4° - 47.0°	35.5° - 44.9°	34.5° - 40.7°	38.1° - 43.6°	35.0° - 41.3°	36.2° - 41.7°	39.6° - 44.7°	37.8° – 43.8°
Sensor velocity [m/s]	90.15	90.64	90.48	89.51	89.91	89.85	90.43	89.83	90.20
Sensor altitude [m]	2496.7	2497.4	2495.9	2497.1	2496.8	2456.3	2500.7	2498.8	2455.3
Flight direction (Cardinal dir. and dir. relative to wind) NE=Northeast, SW = Southwest UW=Up Wind, DW = Down Wind	NE (DW)	SW (UW)	NE (DW)	SW (UW)	NE (DW)	SW (UW)	SW (UW)	NE (DW)	SW (UW)
Age of emulsion at time of acquisition [hours]	~ 5.00 - 5.50	~ 5.15 - 5.55	~ 5.25 - 5.66	~ 5.33 - 5.75	~ 5.47 - 5.87	~ 5.50 - 6.00	~ 5.8 - 6.16	~ 5.92 - 6.32	~ 6.16 - 6.66
Date of acquisitions	12 June 2019								
Resolution (Rg × Az) [m](X-, S-, L-Band)	(0.2 × 0.2), (0.5 × 0.35), (1 × 0.4) *								
Pixel spacing (Rg × Az) [m](X-, S-, L-Band)	(0.60 × 0.18), (0.60 × 0.18), (0.60 × 0.36) *								
Frequency of radiation [GHz](X-, S-, L-Band)	9.6, 3.25, 1.325								
Wind speed [m/s]	12								

*Nominal values for F-SAR taken from **[12]**.

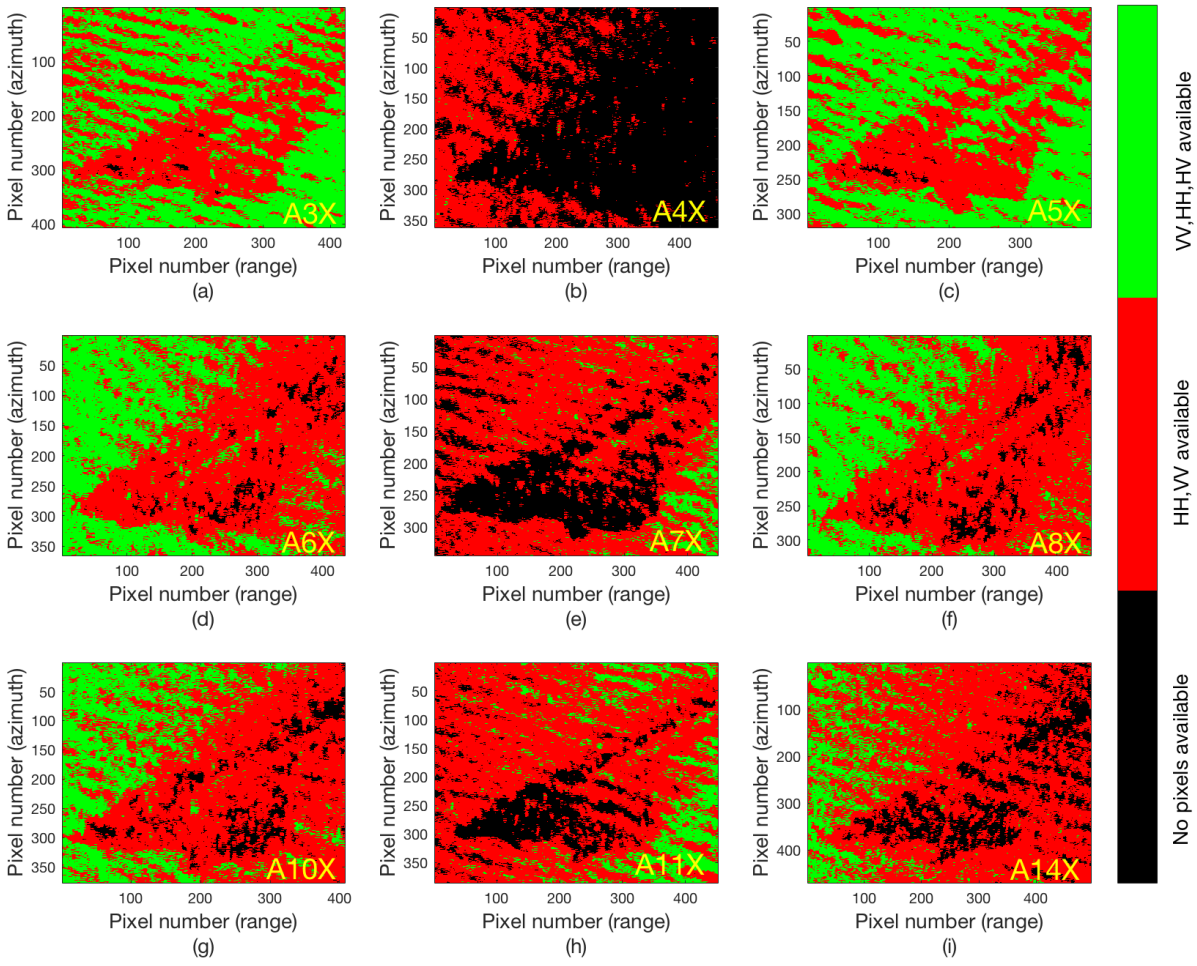

Fig. 3 (a)-(i) Results of noise analysis for the X-band frequency channel in the 9 acquisitions. As can be seen, some amount of noise corruption is present in all data sets indicating that there are some pixels within the slick regions that are unusable.

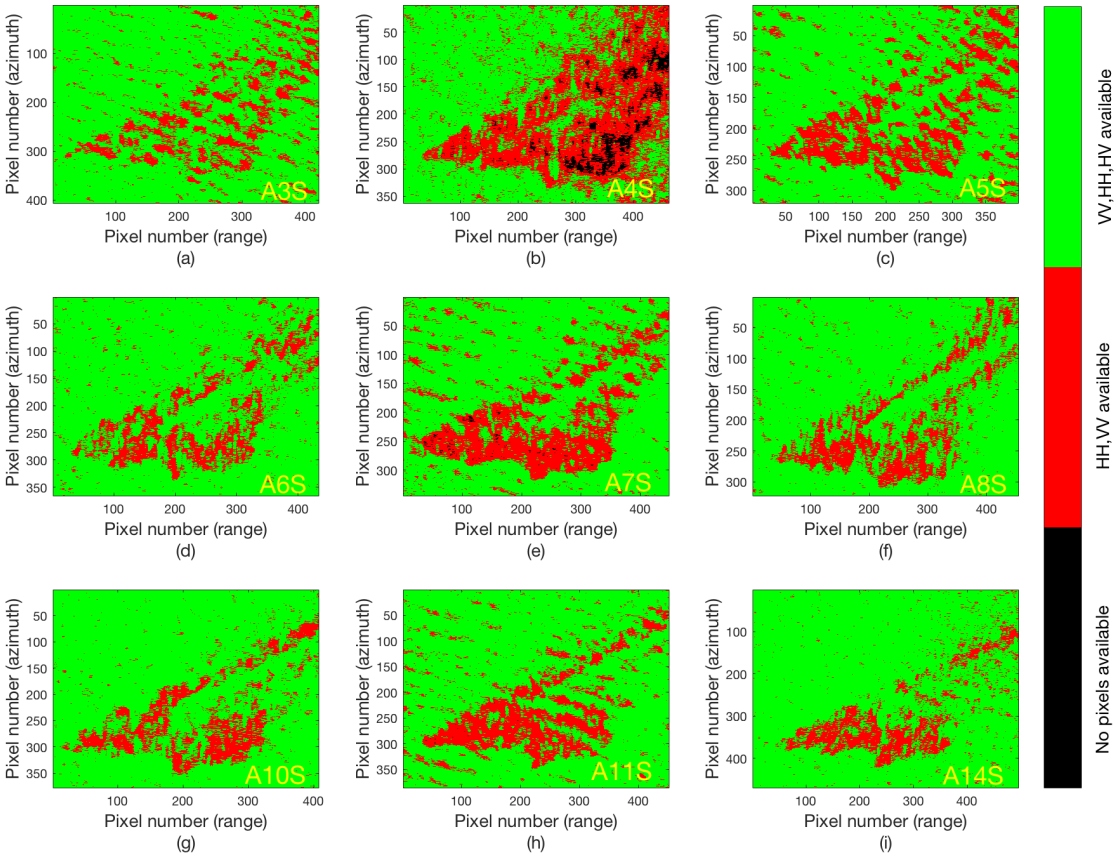

Fig. 4 (a)-(i) Results of noise analysis for the S-band frequency channel in the 9 acquisitions. As can be seen, all pixels are above the 6dB threshold in either all the channels HH, VV and HV (green) or in the dual polarization channels VV and HH only (red). A notable exception however is the A4S acquisition shown in (b).

B. Noise Analysis

Quigley et. al [9] conducted a thorough noise analysis on the F-SAR acquisitions of the NORSE 2019 oil-on-water experiment that were used in that paper. They demonstrated that the L-band acquisitions had significantly lower Noise Equivalent Sigma Zero (NESZ) values ranging between -45 to -60 dB approximately, while both the X- and S-bands had NESZ values ranging between -30 to -45 dB approximately.

In order to determine the feasibility of using the 9 SAR images presented in this study (i.e. the X-, S- and L-band imagery in A3, A4, A5, A6, A7, A8, A10, A11 and A14), the following operations were carried out. Following [5] and [13], a 6 dB threshold was imposed where by pixels (in the VV, HH and HV polarization channels of each acquisition) that were greater than 6 dB above the noise floor, were kept for further analysis, and pixels that were less than 6 dB above the noise floor were discarded. Fig. 3 and 4 show the noise characteristics of the 9 acquisitions for both X- and S-bands. In Fig.3 and 4, these pixels that were kept are color coded as green. This 6 dB threshold was imposed so as to ensure that only pixels that primarily contain signal are included in the analysis.

Next, pixels that were 6 dB above the noise floor in only the VV and HH channels but not the HV channel were kept and the rest were discarded. In Fig. 3 and 4, these pixels are color coded as red.

Pixels that are above the 6 dB threshold in only one polarimetric channel, most likely the VV channel, are color coded as black as well as those pixels that are unusable for further analysis in this study, i.e. pixels that were below the 6 dB threshold in all polarization channels.

The pixels that are color coded as either red of green are of particular interest due to the fact that the co-polarization ratio is required for inversion of the SAR data into values for $|\varepsilon|$. This will be explained in more detail in section III.

As can be seen in this analysis, the X-band acquisitions, as seen in the noise analysis images in Fig. 3, contain a larger number of unusable pixels due to noise corruption (shown in black). The S-band acquisitions have all of their pixels above the 6 dB threshold for either the dual polarimetric channels or for all four polarimetric channels. This can be seen in the noise analysis images in Fig. 4. Note the masks derived from the L-band acquisitions are not included here as all pixels are above the 6 dB threshold in all polarization channels for this frequency band.

It should be noted that this NESZ information was provided by DLR.

C. Noise Characteristics of X-band Imagery

Broadly, speaking a pixel would become noisier, i.e. have a lower SNR, due to one of two reasons, or a combination of both. The first is that the radar return within a pixel is reduced due to a decrease in surface roughness of the scattering surface. Correspondingly a lowering of the electrical permittivity would also affect the return to the radar [5]. The second is that the incidence angle of the scatterer is either too high resulting in a pixel value being too close to the noise floor. In the following, we demonstrate that the SNR in X-band is very sensitive to the incidence angle of the sensor. The reduction in SNR more than likely not a result of geophysical processes occurring, that would reduce the surface roughness of the ocean surface, i.e. emulsification.

As an extreme example of this, the noise profile of the A4 acquisition in both X-band and S-band, as seen in Fig. 3 and 4 (b) respectively show a higher proportion of pixels, internal to the slick, being unusable. This is denoted by the pixels with a black color observed in both images. As can be seen in Fig. 2 and Table 2, this acquisition had the highest incidence angle values of all other acquisitions.

In order to demonstrate the extreme incidence angle dependence of the radar return in X-band, the reader is directed to Fig. 2. This image shows the range of incidence angle values the acquisitions have. Note, we only refer to the region of interest which is the head of the mineral oil emulsion slick, i.e. these are the incidence angles the red boxes in Fig. 1 span. The acquisition ID can be seen at the extreme left of the graph. At the extreme right of the graph, the flight direction (NE or SW (see Table 2)) of the radar, as well as the proportion of non-black pixels in each noise image of Fig. 3 can be seen.

Skrunes et. al [15] examined the effect that imaging geometry has on oil spill observations using polarimetric SAR. The term 'imaging geometry' in their paper referred to the effect of sensor incidence angle and look direction relative to the wind. In their paper, they demonstrate that higher backscatter return is observed when the sensor was pointing in an up-wind direction than a down-wind direction, with the σ^0_{HH} backscatter values showing the greatest sensitivity to the change in look direction.

When we consider the acquisitions that were acquired when the sensor was travelling in a southwest direction (up-wind), i.e. A6, A8, A10 and A14 (minus A4 as explained above) a clear trend can be observed in the number of pixels with satisfactory SNR that are marked in yellow in Fig. 2. As can be seen, as the incidence range angle gradually increases, the number of pixels internal to the slick, that are unusable also increases. This can be observed in Fig. 3 (d), (f), (g) and (i).

The same incidence angle trend can also be observed by looking at the X-band noise profiles of the acquisitions that were taken when the sensor was flying in a Northeast direction (down-wind). As can be seen, the A3 and A5 acquisitions have the lowest amount of corrupted pixels, as seen in Fig. 3 (a) and (c), and also lay in the lowest incidence angle range for all acquisitions taken while the sensor was flying in a Northeast direction. It should also be noted that the region of interest for these two acquisitions span the largest amount of incidence angle values.

The A7 and A11 acquisitions have the highest proportion of their pixels corrupted by noise while also having the incidence angle range with the highest values. As already said, the σ^0_{HH} backscatter values will have lower values when the radar is flying in an up-wind direction (northeast) [15]. The backscatter dependency on flight direction, as well as the incidence angle dependency, increases the probability of a pixel being closer to the noise floor, and thus being colored black in Fig. 3.

III. Polarization Ratios and Oil Concentration

In the field of oil spill remote sensing, single polarimetric SAR systems were first used for monitoring purposes. These systems use only one polarimetric channel to extract information such as the geometry and shape of the patch of oil, the oil-sea contrast, contextual features such as wind history, as well as slick location relative to shore lines, oil rigs and ships [16]. In recent years, there has been extensive research into the use of multi-polarization features for the detection and characterization of low ocean backscatter areas. Some commonly cited studies in regards to this topic can be found in [4] [17] [18].

For the purposes of deriving quantitative information about the dielectric properties of a scattering surface, the co-polarization ratio has proven to be of immediate interest. This polarimetric feature is the ratio of the magnitude of the complex scattering coefficients in the VV and HH channels squared [4], and is defined as

$$R = \frac{\langle |S_{VV}|^2 \rangle}{\langle |S_{HH}|^2 \rangle} \tag{1}$$

In the tilted Bragg model, this quantity is independent of the damping of the wind induced capillary waves which is caused by the presence of oil and is only a function of the relative permittivity of the scattering surface, the large-scale roughness variations, which are unaffected by the presence of oil, and the incidence angle of the incoming radiation. As a consequence, the reduction in backscatter to the SAR is at least partly caused by variations in the dielectric constant of the scattering surface [5]. As already stated in section I, [3] compared C-band RISAT-1 SAR data with thermal IR data collected from an aircraft operated by the Finnish Border Control during an oil-on-water exercise in the North Sea in 2016. They demonstrated that the IR data, specifically in regards to internal areas of the oil slick in that study that were observed to be thicker, correlated well with the damping ratio, indicating that the co-polarization ratio is able to detect internal areas that are thicker/more concentrated with oil.

However, a distinction must be made between the thickness an oil slick obtains and the concentration of oil within the slick. Consider the limiting case of when pure crude oil is spilled on the ocean surface. The slick can be thought of as being composed of 100% oil at the beginning of its life cycle and may only form a thin layer at the ocean surface (Note: this would depend on the viscosity of the oil being spilled which has an impact on the rate of spreading [19]). When emulsification occurs, the volume of the pollutant can increase by a factor of up to 5 [19] and forms most readily when the material has a

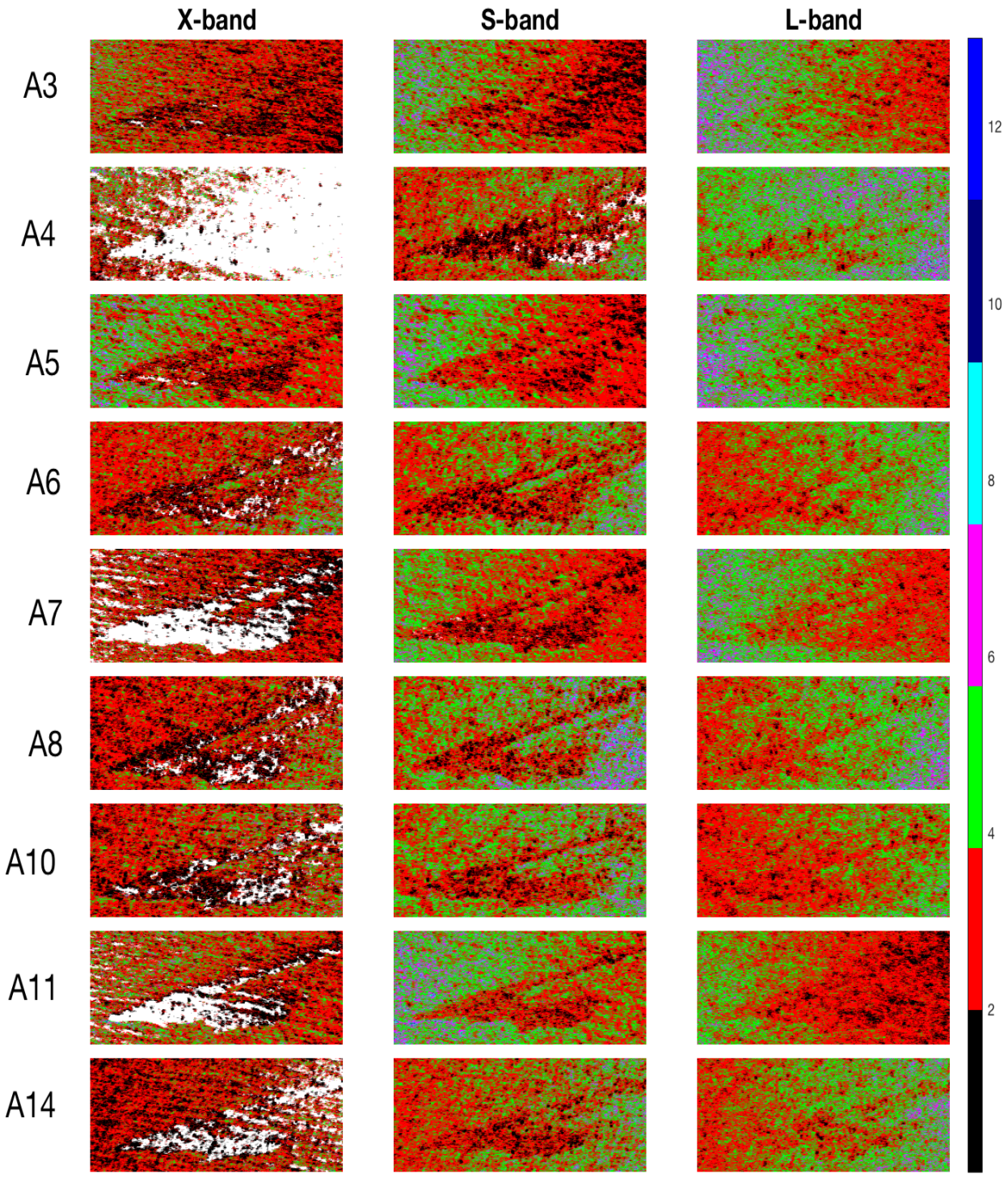

Fig. 5 Co-polarization ratios for each of the 9 acquisitions in all frequency bands calculated using (1). The left most column corresponds to the co-polarization ratios for the X-band acquisitions. The 'white gaps' are regions where pixels didn't contain a sufficiently high SNR in both the VV and HH channels. The middle column corresponds to the co-polarization ratios for the S-band acquisitions. The right most column corresponds to co-polarization ratios for the L-band acquisitions. The disparity between frequency bands is apparent.

combined Nickel/Vanadium concentration greater than 15ppm or an asphaltene content in excess of 0.5% [19]. As emulsification proceeds, the movement of the oil by wave motion can cause the size of the water droplets which have been taken up by the oil to decrease, resulting in a more viscous material. Stable emulsions can form which can be as much as 70 – 80% water and may be semi-solid. Thus, the thickness of the slick can increase, but the concentration of the oil-in-water mixture may decrease. Given this, much has been written about the damping ratio, which is a measure of the contrast between oil slick and the surrounding clean sea. An explanation can be found in [20]. Some studies, specifically [21]-[24], have reported that the damping ratio increases with wavenumber, oil viscosity and slick thickness.

In contrast to this, the permittivity of the oil slick can be directly related to the volumetric concentration of oil within slick. Via the application of an appropriate theoretical scattering model, the effective dielectric constant of the scattering surface can be determined from the co-polarization ratio [25],[26]. Once this is determined, these effective values can be substituted into a mixing model to determine the volumetric content of oil within a pixel. Angelliuame et. al [27] demonstrated that the Bruggeman mixing model was the most appropriate mixing model available in the literature for this task.

Fig. 5 shows the co-polarization ratio images for all acquisitions in the three frequency bands that were calculated using (1). The left column of Fig. 5 shows the co-polarization ratio formed from the 9 X-band acquisitions. As can be seen, the noise degradation in this frequency band serves to reduce the amount of viable information that can be derived. This noise degradation can be seen as white regions in the left column of Fig. 5. These white regions correspond to pixels that did not have sufficient SNR in the co-polarization channels and so have been omitted here. Another aspect of this band is that there is not much variation within slick in terms of internal zoning, i.e. for all 9 acquisitions, the slick filled areas appear to be homogeneously dark. This fact, combined with noise issues indicate that this frequency band is difficult to work with and may not be suited for this application.

The L-band co-polarization ratio imagery, as shown on the right column of Fig. 5, do not show a high degree of contrast between the slick filled areas compared to areas outside the slick. Despite this, internal areas can be distinguished that may be areas indicating the thickest parts of the slick. Given the excellent noise characteristics of the L-band imagery, and its possible ability to determine the absolute thickest parts of the slick, L-band may prove to be beneficial for this application.

The S-band co-polarization imagery, as shown in the center column of Fig. 5, show a good compromise between the penetration ability of the sensing radiation used, and the noise characteristics of that band. Internal areas of more concentrated oil can be seen internal to the slick, which can indicate to first responders which areas should be targeted first.

IV. Combination of the Co-polarization ratio

In the previous section, we demonstrated how the penetration ability of the sensing radiation, versus the dielectric characteristics of the scattering surface, can affect the appearance of oil slick in the co-polarization ratio imagery.

In the next subsection we demonstrate a method of combining the co-polarization ratios from different frequency bands into one product that is capable of providing a heuristic based assessment of where there is a greater concentration of oil within slick. We call this quantity *the incidence angle normalized sum of co-polarization ratios*. This quantity can be calculated instantaneously and requires no modeling of the surface backscatter and so can be applied quickly in-field and requires no estimation of other key geophysical parameters, such as large-scale roughness indicators. An explanation is given in the next subsection.

A. Incidence angle normalized sum of co-polarization ratios

The co-polarization ratio is dependent on a few key quantities and can be expressed as follows

$$R = f(\varepsilon, s, IA) \tag{2}$$

where ε is the electrical permittivity of the scattering surface, s is an indication of the large-scale roughness of the surface scatterer and IA is the incidence angle of the incoming radiation.

When the co-polarization ratio is calculated with the VV channel being divided by the HH channel, the slick filled areas will appear darker than the surrounding ocean areas. In order to derive a normalized measure of the co-polarization ratio, the maximum pixel value at each incidence angle value in the range direction is determined (Note: this requires the open water pixels to be visible). The maximum value that is determined is then divided into the co-polarization ratio pixels at each incidence angle value in range direction. This is given by

$$\gamma_{band} = \frac{R_{band,i}}{max\{R_{band,i}\}} \tag{3}$$

where the subscript 'band' indicates the frequency band the quantity is calculated in, i.e. X-, S- or L-band for this study. The subscript 'i' indicates the column of co-polarization values in azimuth direction for specific incidence angle values in range direction.

The γ_{band} values now found, indicate the relative contribution to the backscatter due to the dielectric properties of the scattering surface across the entire image and will have values between 0 and 1. The low values, i.e. close to zero, indicate more concentrated areas of oil while the high values, i.e. close to 1, will indicate areas of open water. In order to determine agreement between bands, the γ_{band} values, over all frequency bands, are summed together. Pixels that show agreement in terms of low dielectric values will be close of zero in the resulting image. Pixels that show agreement in terms of areas of high dielectric values will have values close to M, where M is the number of frequency bands being considered and will correspond to areas of open water. Areas where pixels do not agree will have intermediate values between 1 and M.

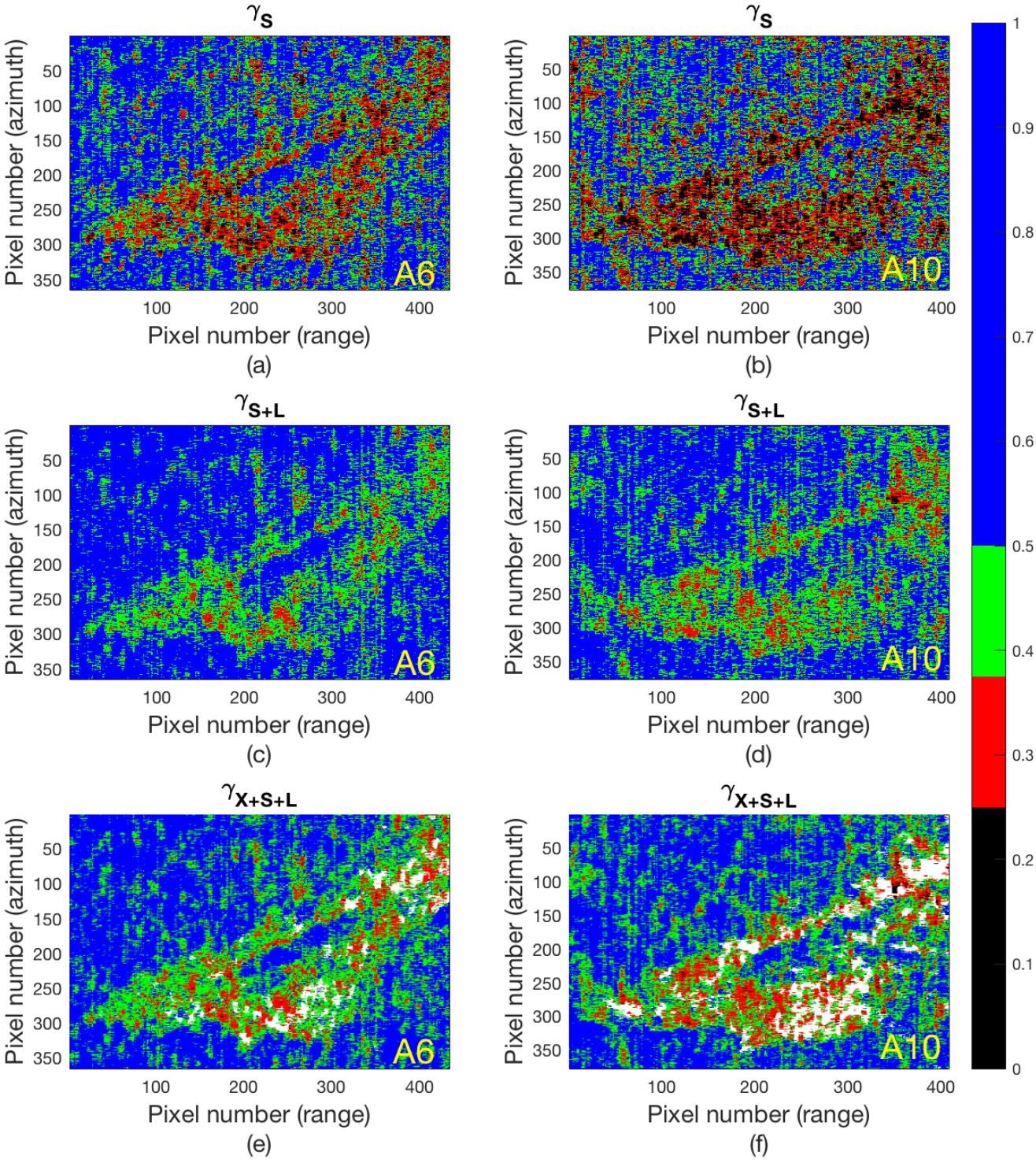

Fig. 6 The proposed feature γ, calculated for (a)-(b) S-band. (c)-(d) A combination of S- and L-band. (e)-(f) a combination of X-, S- and L-band, for both of the acquisitions A6 and A10. As can be seen, γ_{X+S+L} appear to offer the best discrimination of the internal zones within the slick but are hampered by the noise profile of the data.

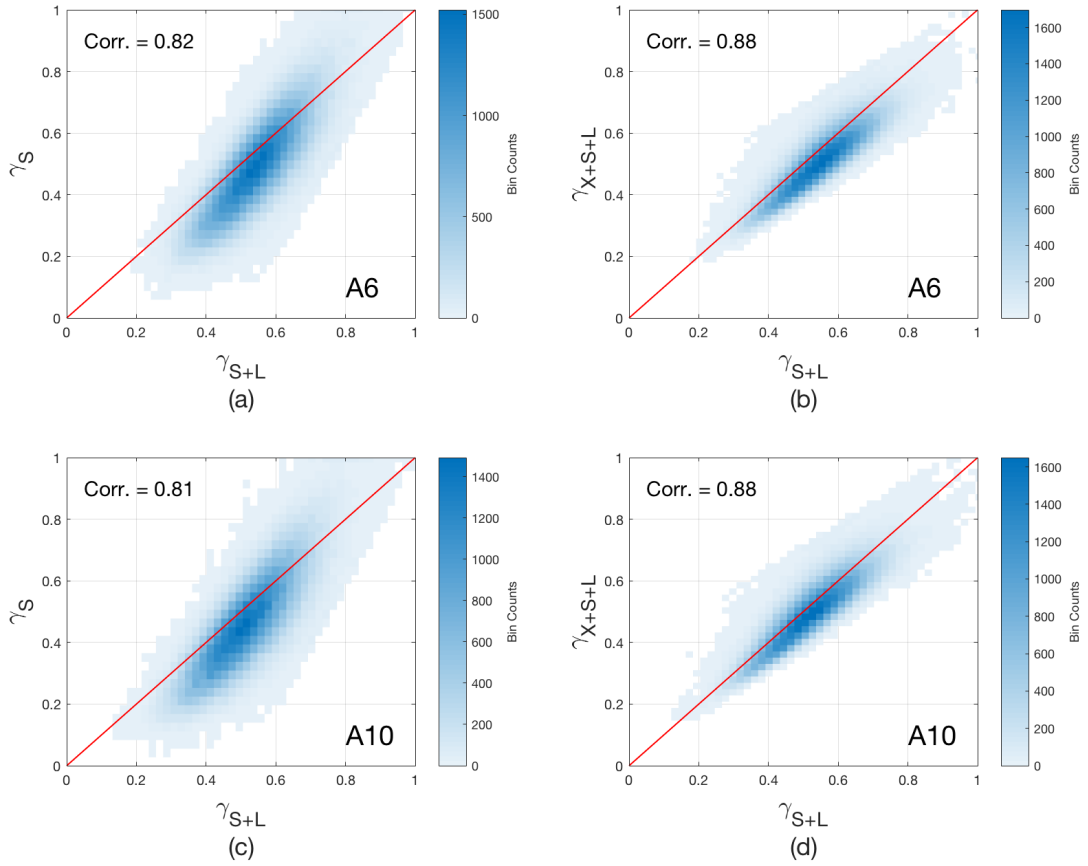

Fig. 7 (a)-(b) Scatter graphs of γ_{S+L}, versus γ_S and γ_{X+S+L} for A6. (c)-(d) Scatter graphs of γ_{S+L}, versus γ_S and γ_{X+S+L} for A10. As can be seen the correlation coefficient is similar across all four scatter graphs.

As can be seen in Fig. 5, the S-band co-polarization ratio images showed the greatest consistency in terms of being able to retrieve information internal to the slick. For this reason, the following analysis will be conducted relative to the S-band acquisitions. The quantities γ_S, γ_{S+L} and γ_{X+S+L} were calculated for the A6 and A10 acquisitions. These two acquisitions were chosen as the noise characteristics in the X-band co-polarization values, as seen in Fig. 5, are minimal and the L-band co-polarization imagery show some degree of contrast within slick, i.e. internal areas can be observed. The 6 resulting images are shown in Fig. 6. The γ_{S+L} and γ_{X+S+L} images were rescaled to lie between 0 and 1 so that an appropriate colormap could be applied to all three. This was to create a common framework in which to compare the three results. Note, the colormap applied to Fig. 6 was chosen to provide the best visual appearance.

As expected, γ_S images for A6 and A10, shown in Fig. 6 (a) and (b), which are based solely on the S-band imagery show the internal areas of the slick which contain more concentrated areas of oil. This is indicated by the black areas internal to the slick. The γ_{S+L} imagery, shown in Fig. 6 (c) and (d), show the more concentrated areas of the slick. As can be seen, these images appear to select the darker areas from the γ_S imagery thus highlighting the areas of the slick which should be addressed first in a clean-up operation. The γ_{X+S+L} imagery, as shown in Fig. 6 (e) and (f) as well highlight the darker areas from the γ_S imagery but do not appear to add a significant amount of information over the γ_{S+L} imagery. This is most likely due to the short penetration depth of the X-band radiation indicating that the entire slick filled area had homogenous normalized values and thus adding no distinctive information in regards to internal zones within slick

In order to compare the results numerically, scatter graphs were constructed where the γ_{S+L} values were placed on the x-axis and both γ_S and γ_{X+S+L} values were paced on the y-axis for both the A6 and A10 acquisitions. This can be seen in Fig. 7.

As can be seen for the γ_{S+L} values versus the γ_S values, as shown in Fig. 7 (a) and (c), the correlation coefficient is high between both sets of values, i.e. 0.82 and 0.81 respectively, this is to be expected as the γ_{S+L} values are derived from the γ_S values. However, the distribution of the scatter appears to be rotated slightly about the red line that denotes a direct correlation between the two sets of values. In Fig. 6 (a) and (c), the values for γ_S that lie below 0.5 approximately are shifted to higher values in γ_{X+S+L}. This can be observed in the

imagery of Fig. 6 (a)-(d) and indicates that new information is present in the γ_{S+L} as opposed to the γ_S imagery.

Fig. 7 (b) and (d) show the scatter graphs for the γ_{S+L} values versus the γ_{X+S+L} values. Again, the correlation coefficient is shown and can be seen as 0.88 for both A6 and A10. This is indicating that the correlation between γ_{S+L} and γ_{X+S+L} is higher than that of γ_{S+L} and γ_S but only by 0.06 and 0.07 respectively. The most apparent feature about the graphs in Fig. 7 (b) and (d) is that that scatter is confined to the red correlation line. This indicates that via the addition of the X-band normalized co-polarization ratio, not a significant amount of new information is generated.

B. Stability Analysis

When many successive SAR scenes of an oil slick are available, we can make use of the temporal aspect of the acquisitions to try to determine which regions within a slick show consistently low values for the co-polarization ratio (it should be noted that this is when the co-polarization is calculated using (1). If the inverse of (1) is employed, we would look for consistently high co-polarization ratio values.) This is done by counting the number of scenes in which the co-polarization ratio is below a certain threshold (T_h). It should be noted that due to the wide range of incidence angles that the data from F-SAR covers (see Fig. 2), it can difficult to assign a relevant threshold for an entire scene. As an example, Fig. 5 shows the co-polarization ratio of all 9 acquisitions in all 3 frequency bands for the data in this study. Consider the case of the A7 S- and L-band imagery here. As can be seen, to the right side of the images, there is a high concentration of pixels with values of 4, whereas to the left side of the images, we have a high concentration of pixels with values of 2. Pixel values intermediate to the two sides of the images display a gradient between these two values.

Because of this, the incidence angle normalized sum of co-polarization ratios is exploited in this section, as a single numerical threshold, representative of the entire scene, can be applied.

The following procedure for determining a measure of stability, the stability level (*SL)*, was developed by [20] for the purposes of determining which areas within a slick, emanating from a sea bed seep source, were consistent across 6 successive SAR scenes, by using the damping ratio calculated using the VV polarimetric channel within L-band Uninhabited Aerial Vehicle Synthetic Aperture Radar (UAVSAR) imagery. Here we adopt the same approach utilizing the feature presented in the previous section in the three forms γ_S, γ_L, γ_{S+L}. A time series of γ_X or γ_{X+S+L} is not considered here due to the noise issues associated with the X-band data. An explanation is as follows.

When acquiring successive SAR imagery of an evolving oil spill event, the most recent acquisition is the most relevant in providing a status update on the condition of the slick. In order to account for this, the SL is calculated by applying successively higher weights to more recent scenes. The input to the SL is a binary image calculated by

$$B_i(x,y) = \begin{cases} 1, \text{if } F_i(x,y) < T_h \\ 0, \text{f } F_i(x,y) > T_h \end{cases} \quad (4)$$

where i = [1,N], F_i is the feature under consideration (i.e. γ_S, γ_L, γ_{S+L} in this case) and which is evaluated for the i^{th} scene, where i = 1 indicates the first scene in a timeseries, and i = N indicates the most recent scene in a time series, (x, y) are the spatial coordinates within a scene. The SL is then calculated as

$$SL_i(x,y) = \begin{cases} B_i(x,y), & i = 1 \\ \alpha B_i(x,y) + (1-\alpha) SL_{i-1}(x,y), & i > 1 \end{cases} \quad (5)$$

where again i = [1, N]. The coefficient α is an indication of the level of the weighting which retains a value between 0 and 1. This value must be chosen a priori. If we choose a high α value, older observations are discounted faster. If the limiting value of $\alpha = 1$ is chosen then $SL_i(x,y) = B_i(x,y)$ and the SL values calculated are equal to the current binary image. If $\alpha = 0$ is chosen $SL_i(x,y) = B_1(x,y)$ which indicates that all new observations are discarded.

In this work, we follow [20] and set $\alpha = 0.5$. In this way, the current observation under review is given an equal weight to that of previous observations combined. The resulting values are weighted between 0% and 100%, where 100% indicates completely stable oil pixels, i.e. the feature value for a given pixel location in the image is above the imposed T_h value throughout the time series. The T_h values are adjustable to cover the range of values within a scene with low value for T_h being used to identify the more oil infested regions of a slick.

It should be noted that in [20], a timeseries of an oil seep event was analyzed in which a fixed point of reference was available for the purposes of georeferencing the timeseries data. In this paper we apply the method to multifrequency SAR data of a freely floating oil slick. In order to create some degree of consistency between images of the time series, the SAR acquisitions were kept in radar coordinates and the same approximate region of interest was chosen, i.e. 'the head' of the slick. This can be seen in the co-polarization ratio imagery of Fig. 5.

Fig. 8 shows the SL maps for γ_S, γ_L and γ_{S+L} made using all the acquisitions presented in this study, minus the A4 acquisition due to the noise issues encountered in the S-band, i.e. 8 scenes were used in this analysis. As stated in [20] the purpose of finding the SL measure is to locate the regions within the slick that have consistently low co-polarization ratio values over a given period of time, with the ultimate goal of being able to reduce the deployment time of first responders to the most relevant parts of an oil slick. Different sets of thresholds were chosen for each of the γ_S, γ_L and γ_{S+L} parameters and can be seen in Fig. 8. As the weighting factor of 0.5 is used, a pixel with an SL value above 50% will indicate the most recent scene and some scenes before the latest scene was acquired had γ values above the designated threshold. Areas that have a high SL value are colored as red to indicate the slick filled areas that are most stable. The more variable areas within slick are colored as black.

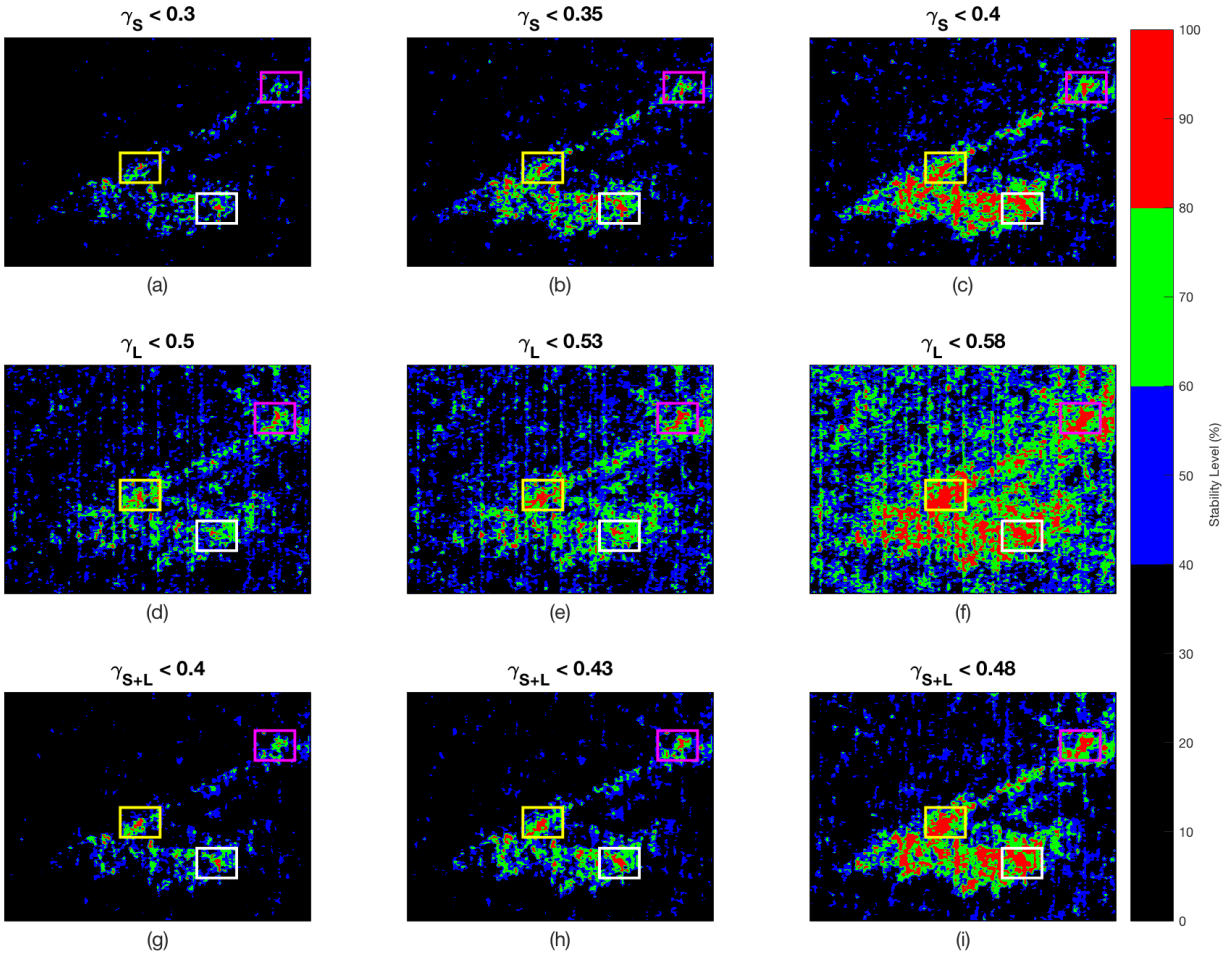

Fig. 8 Images showing the SL for γ_S (a)-(c), γ_L (d)-(f) and γ_{S+L} (g)-(i). Various thresholds were applied in order to emphasis the regions of stability within the slick. Regions that appear constant across images are indicated by the colored boxes.

When applying this measure, we would expect to see the most stable areas of the slick being highlighted when successively lower thresholds are applied. In Fig. 8, we highlight 3 areas of the sick that appear to be consistent irrespective of the threshold applied. This is outlined by the three boxes colored white, yellow and pink that are superimposed on the image. Another expectation is that some degree of consistency should be observed between the stability images for γ_S, γ_L and γ_{S+L}. As can be seen the same areas, outlined by the boxes color coded white, yellow and pink are visible. It should be noted that the threshold that was applied was tuned to the specific image under investigation in order to provide the best visual result.

An interesting result is that the images for SL, obtained using γ_S and γ_{S+L} are similar. This indicates that it may be possible to gain roughly the same quantitative information about the long-term stability within a slick using just γ_S then when the information within L-band is added. The only caveat is that the regions in the γ_{S+L} imagery appear to be slightly more defined and less numerous than in the γ_S imagery. This can be seen when comparing Fig. 8 (a), (b) and (c) and Fig. 8 (g), (h) and (i) above, indicating that applying the stability measure to γ_{S+L} yields slightly better results.

It should be noted that in Fig. 8 different thresholds have been applied to each to the SL values for the parameters γ_S, γ_L and γ_{S+L}. This is was done in order to obtain the best visual result. The reason the same threshold cannot be applied to each of the calculated parameters in Fig. 8 is due to the different penetration capabilities of S- and L-band radiation.

V. Conclusion

In the first part of this paper, we introduced an experimental data set collected during the NORSE 2019 oil-on-water experiment conducted in the North Sea. The data set presented was unique in that it contains numerous multi-temporal and multi-frequency F-SAR acquisitions of a slick of mineral oil emulsion. Comprehensive information in regards to the

discharged material is presented as well as information relating to the atmospheric conditions at the time the experiment took place.

In the second part of this paper, we presented a detailed noise analysis which displayed the individual noise characteristics of the data within each of the frequency bands. The L-band acquisitions had excellent noise profiles, with 100% of their pixels above the noise floor in all four polarimetric channels.

The noise profiles for the S-band acquisitions showed a trend of having 100% of their pixels above the noise floor for the slick-free areas in all four polarimetric channels but only having pixels in the VV and HH channels 6 dB above the noise floor for the slick filled areas. The only exception was for the A4S acquisition where some of the pixels internal to the slick were corrupted by noise in all four polarimetric channels. This however, could be directly related to the high incidence angle that the acquisition acquired under. The X-band acquisitions showed a high degree of noise corruption for pixels internal to the slick for all polarimetric channels. The noise analysis in section II demonstrated that this is most likely due to the incidence angle under which the data was acquired.

Previous studies have attempted to derive quantitative information on the internal state of an oil slick, specifically the volumetric content of oil, by applying theoretical backscattering models. The use of these models necessitates the use of the polarization ratios as the small-scale roughness spectrum in these polarimetric ratios cancels out. Given that the cross-polarization ratio is often unavailable for use due to the highly non-depolarizing nature of the ocean surface, the co-polarization ratio is often employed and was investigated here.

Fig. 5 shows a series of the co-polarization ratio images for each of the acquisitions that were considered in this study. As can be seen, the viability of deriving information in regards to useful quantities such as the dielectric constant of the scattering surface is hampered by, firstly, the noise characteristics of the sensor (as demonstrated by the X-band data) and secondly the penetration ability of the sensing radiation (as demonstrated by the L-band data). The latter can be observed in the far-right column of Fig. 5 where little contrast exists between the slick filled areas and the slick-free areas. The exception is small areas that present as darker in relation the rest of the image. It is assumed that these small areas are regions where the oil was thick on the scale of the incoming radiation to interact with the radiation via the dielectric properties of the scattering surface.

Next, a polarimetric feature was proposed which aimed to combine the co-polarization ratios from each of the frequency bands into one product which would provide the user with an indication of which areas within the slick which contained a greater concentration of oil in contrast to others. The feature, which is referred to here as the *incidence angle normalized sum of co-polarization ratios*, aimed to combine the co-polarization ratios from the S- and L-bands as well as the X-, S- and L-bands. The proposed feature is conceptually simple, does not require any theoretical modelling and is computationally efficient, so can be applied in-field to produce instantaneous imagery. The results show that the combination of all three frequency bands, i.e. γ_{X+S+L}, produced coherent concentration maps but were not significantly different to γ_{S+L}. The γ_{S+L} results here showed the best results in terms of being able to determine areas which had the greatest concentration of oil within slick.

Next, we applied a stability measure to the entire time series of the proposed feature, specifically in regards to γ_S, γ_L and γ_{S+L} and showed that the resulting SL values for γ_{S+L} were best in being able to determine the most stable regions within the slick, however γ_S also appeared to provide sufficient values. The reasoning in applying the stability measure to the proposed feature and not directly to the co-polarization ratio was due to the wide range on incidence angles encountered in the F-SAR data, indicating that the application of an appropriate threshold would be difficult, and would produce unusable results for the stability measure.

Despite the fact that there is an increased interest in being able to derive information relating to oil spill events directly from satellite borne SAR, airborne SAR systems offer a number of advantages. Among these is the fact that airborne SARs can be more flexible in their ability to collect data from various look directions and angles. As well as this, airborne instruments have the ability to be deployed at will, as long as flying conditions permit. However, the most apparent advantage is the ability to acquire simultaneous imagery in multiple frequency bands and with relatively low noise floors.

The analysis presented in this paper however demonstrates that for the purposes of deriving useful information about the internal structure of an oil slick, X-band airborne SAR has proven itself to not be viable operationally. This is mainly due to the noise issues that are associated with this frequency band as well as its sensitivity to look-angle. In addition, the low penetration depth of X-band radiation indicates that little internal contrast within slick can be determined. The combination of L-band and S-band into the aforementioned feature has demonstrated itself to warrant further investigation. Our recommendation is that more emphases is put on collecting in-situ information for verification purposes. In addition, we recommend that the experiment is replicated to incorporate C-band data. The expectation is that C-band radiation might be able to add additional information in regards to the internal state of the slick.

Acknowledgment

The authors wish to thank Veronique Miegebielle from Total E&P. This work is funded by CIRFA through the RCN (grant no. 237906) and CIRFA partners. The authors would also sincerely like to thank NOFO for including our experiment in their exercise. In particular we would like to thank the crew from NOFO onboard R/V Helmer Hanssen and Kristin K. Husebye at NOFO HQ for her efforts in accommodating our numerous requests. We would like to thank DLR and the crew on board the F-SAR aircraft. In addition, we would like to thank Martine Espeseth for her advice in preparing this manuscript.

References

[1] M. M. Espeseth, C. E. Jones, B. Holt, C. Brekke, and S. Skrunes, "Oil- spill-response-oriented information products derived from a rapid-repeat time series of sar images," *IEEE Journal of Selected Topics in Applied Earth Observations and Remote Sensing*, vol. 13, pp. 3448–3461, 2020.

[2] Bonn Agreement Secretariat, "Bonn Agreement Aerial Operations Handbook", London, UK, Tech. Info. Paper, 2016. Available: https://www.bonnagreement.org/site/assets/files/1081/aerial_operations_handbook.pdf, Accessed on: Oct. 27, 2020.

[3] S. Skrunes, C. Brekke, M.M. Espeseth, "Assessment of the RISAT-1 FRS-2 mode for oil spill observation" in *IEEE IGARSS,* Fort Worth, TX, USA, 2017, pp.1024-1027.

[4] S. Skrunes, C. Brekke, T. Eltoft, "Characterization of marine surface slicks by Radarsat-2 multipolarization features", *IEEE Trans. Geosci. Remote Sens.*, vol. 52, no. 9, pp. 5302-5319, Sep. 2014.

[5] B. Minchew, C. E. Jones, and B. Holt, "Polarimetric analysis of backscat- ter from the Deepwater Horizon oil spill using L-band synthetic aperture radar," *IEEE Trans. Geosci. Remote Sens.*, vol. 50, no. 10, pp. 3812–3830, Oct. 2012.

[6] K. Folger, "Bilinear calibration of coaxial transmission/ reflection cells for permittivity measurements of low-loss liquids," *Meas. Sci. Technol.*, vol. 7, no. 9, pp. 1260–1269, Sep. 1996.

[7] C. Quigley, C. Brekke, T. Eltoft, "Retrieval of Marine Surface Slick Dielectric Properties from Radarsat-2 Data via a Polarimetric Two-Scale Model", *IEEE Trans. Geosci. Remote Sens.*, vol. 58, no. 7, pp. 5162-5178, July 2020.

[8] A. Iodice, A. Natale, D. Riccio, "Retrieval of soil surface parameters via a polarimetric two-scale model", *IEEE Trans. Geosci. Remote Sens.*, vol. 49, no. 7, pp. 2531-2547, Jul. 2011.

[9] C. Quigley, C. Brekke, T. Eltoft, " Comparison Between Dielectric Inversion Results from Synthetic Aperture Radar Co- and Quad-Polarimetric Data via a Polarimetric Two-Scale Model", *IEEE Trans. Geosci. Remote Sens.*, (in Early Access).

[10] A. Iodice, A. Natale, and D. Riccio, "Polarimetric two-scale model for soil moisture retrieval via dual-Pol HH-VV SAR data," *IEEE J. Sel. Topics Appl. Earth Observ. Remote Sens.*, vol. 6, no. 3, pp. 1163–1171, Jun. 2013.

[11] C. Brekke, M.M. Espeseth, K. F. Dagestad, J. Röhrs, L. R. Hole and A. Reigber, "Integration of multi-sensor datasets and oil drift simulations - a free floating oil experiment in open ocean", JGR: Oceans, 2020 (in print).

[12] A.Reigber, M.Jager, M.Pinheiro, R.Scheiber, P.Prats, J.Fischer, R. Horn, A. Nottensteiner, "Performance of the P-band subsystem and the X-band interferometer of the F-SAR airborne SAR instrument," in *Geoscience and Remote Sensing Symposium (IGARSS), 2012 IEEE International*, July 2012, pp. 5037–5040.

[13] A. Freeman and S. Durden, "A three-component scattering model for polarimetric SAR data, "IEEE Trans. Geosci. Remote Sens., vol. 36, no. 3,pp. 963–973, May 1998.

[14] G. R. Valenzuela, " Scattering of electromagnetic waves from a tilted slightly rough surface ", *Radio Sci.,* vol. 3, no. 11, pp. 1057-1066, Jan. 1968.

[15] S. Skrunes, C. Brekke, C. E. Jones, M. M. Espeseth, and B. Holt, "Effect of wind direction and incidence angle on polarimetric SAR observations of slicked and unslicked sea surfaces," *Remote Sens. Environ.*, vol. 213, pp. 73–91, Aug. 2018.

[16] Brekke, C. and Solberg, A. H. S. (2005). Oil Spill Detection by Satellite Remote Sensing. *Remote Sens. Environ.*, 95(1):1–13.

[17] C. Brekke, B. Holt, C. Jones, and S. Skrunes, "Discrimination of oil spills from newly formed sea ice by synthetic aperture radar," *Remote Sens. Environ.*, vol. 145, pp. 1–14, Apr. 2014.

[18] S. Singha, R. Ressel, D. Velotto, and S. Lehner, "A combination of traditional and polarimetric features for oil spill detection using TerraSAR-X," *IEEE J. Sel. Topics Appl. Earth Observ. Remote Sens.*, vol. 9, no. 11, pp. 4979–4990, Nov. 2016.

[19] ITOPF, "Fate of marine oil spills," Inter. Tanker Owners Poll. Fed., London, UK, Tech. Info. Paper, no.2, 2011

[20] M. M. Espeseth, C. E. Jones, B. Holt, C. Brekke, and S. Skrunes, "Oil- spill-response-oriented information products derived from a rapid-repeat time series of sar images," *IEEE Journal of Selected Topics in Applied Earth Observations and Remote Sensing*, vol. 13, pp. 3448–3461, 2020.

[21] V. Wismann, M. Gade, W. Alpers, and H. Hühnerfuss, "Radar signatures of marine mineral oil spills measured by an airborne multi-frequency radar," *Int. J. Remote Sens.*, vol. 19, no. 18, pp. 3607–3623, 1998

[22] M. Gade, W. Alpers, H. Masuko, and T. Kobayashi, "Imaging of biogenic and anthropogenic ocean surface films by the multifre- quency/multipolarization SIR-C/X-SAR," *J. Geophys. Res.*, vol. 103, no. C9, pp. 18851–18866, 1998.

[23] N. Pinel, C. Bourlier, I. Sergievskaya, "Two-dimensional radar backscattering modeling of oil slicks at sea based on the model of local balance: Validation of two asymptotic techniques for thick films", *IEEE Trans. Geosci. Remote Sens.*, vol. 52, no. 5, pp. 2326-2338, May 2014.

[24] I. Sergievskaya, S. Ermakov, T. Lazareva, and J. Guo, "Damping of surface waves due to crude oil/oil emulsion films on water," *Marine Pollution Bulletin*, vol. 146, pp. 206–214, 2019.

[25] I. Hajnsek, E. Pottier, S. R. Cloude, "Inversion of surface parameters from polarimetric SAR", *IEEE Trans. Geosci. Remote Sens.*, vol. 41, no. 4, pp. 727-744, Apr. 2003.

[26] A. Iodice, A. Natale, D. Riccio, "Retrieval of soil surface parameters via a polarimetric two-scale model", *IEEE Trans. Geosci. Remote Sens.*, vol. 49, no. 7, pp. 2531-2547, Jul. 2011.

[27] S. Angelliaume, O. Boisot, C.A. Guerin, "Dual-Polarized L-Band SAR Imagery for Temporal Monitoring of Marine Oil Slick Concentration," *Remote Sens.,* vol. 10, no. 7, Jul. 2018.

Cornelius Quigley received his Bachelor degree in Physics in June 2013 from the Department of Physics at the National University of Ireland, Cork. He received his Master's degree from the Department of Physics and Technology at the University of Tromsø - The Arctic University of Norway in June 2017. He started as a PhD student at the same department in September 2017, with the Center for Integrated Remote Sensing and Forecasting for Arctic Operations (CIRFA). His current research interests include remote sensing of ocean areas, specifically by polarimetric SAR and with a focus on marine oil pollution.

Camilla Brekke (M'12) received the Cand. Mag., Cand. Scient., and Ph.D. degrees from the Department of Informatics, University of Oslo, Oslo, Norway, in 1998, 2001, and 2008, respectively. She is currently the Vice-Dean Research with the Faculty of Science and Technology, the Deputy Centre Leader with the Centre for Integrated Remote Sensing and Forecasting for Arctic Operations and full Professor at Department of Physics and Technology, UiT The Arctic University of Norway, Tromsø, Norway. Her current research interests include synthetic aperture radar and ocean color remote sensing for arctic and marine applications.

Torbjørn Eltoft (M'92) received the degrees of Cand. Real. (M.S.) and Dr. Scient. (Ph.D.) from University of Tromsø - The Arctic University of Norway, in 1981 and 1984, respectively. In 1988 he joined the Faculty of Science, University of Tromsø - The Arctic University of Norway, and is presently Professor in electrical engineering at the Department of Physics and Technology, where he also is head of the Earth Observation Laboratory and of the BARESS Remote Sensing School. He also holds a position as Adjunct Professor at Norut, Tromsø. His current research interests include multidimensional signal and image analysis with application in remote sensing, statistical models, neural networks, and machine learning. Dr. Eltoft has been associate editor of the journal Pattern Recognition for five years. He was awarded the year 2000 Outstanding Paper Award in Neural Networks by IEEE Neural Networks Council, and Honorable Mention for the 2003 Pattern Recognition Journal Best Paper Award.

9 Conclusion

The papers presented in Chapters 6-8 delved into the potential of deriving numerical estimates for the dielectric constant of oil slick as observed within SAR imagery. In addition, an analysis of the potential of multifrequency, multitemporal airborne SAR to provide an indication of the concentration of oil within slick was also presented. Section 9.1 will briefly summarize the research included in the three papers, while section 9.2 will discuss and present some directions for future work.

9.1 Research Conclusions

The entire field of oil spill remote sensing can, broadly speaking, be reduced to three sub-disciplines: (1) the detection of an oil spill, (2) differentiating environmentally harmful mineral oil from benign oil spill look-alikes and (3) extracting physical characteristics about an oil spill using remote sensing apparatus. The work presented in this thesis, is heavily slanted towards operating within the purview of the third sub-discipline just cited.

Specifically, this work aims to determine where within an oil slick more concentrated areas of oil reside. This is achieved by either performing an inversion procedure to assign a numerical indicator of the volumetric content of oil within slick, such as the dielectric constant, or exploiting the multifrequency and multitemporal aspect of successive SAR acquisitions to derive a heuristic based indicator of oil slick concentration. The research conclusions from this work are as follows.

Spaceborne SAR sensors have proven to be valuable instruments for determining the location, the extent and in some cases, the source of an oil spill [Espeseth, 2019]. For the purposes of deriving quantitative information on the internal state and structure of an oil slick, such as estimates for the dielectric constant, the noise characteristics have proven sometimes to be a major hinderance.

The authors in [Skrunes et al., 2014] performed a noise analysis, on two fine quad-polarimetric C-band Radarsat-2 data sets acquired during NOFOs oil-on-water exercise conducted in the North sea in 2011. Specifically, they compared the average radar backscatter contained within specified regions of interest from the various backscattering surfaces contained within the SAR imagery, i.e. open water, crude oil slick, slick of oil emulsion and slick of plant oil, against the NESZ information contained within the header files accompanying the data. They found that the cross-polarimetric channels were unusable for further analysis in their paper due to noise corruption. The incidence angle range of the two acquisitions was 46.1° - 47.3° and 34.5° - 36.1°, which are named 2011m and 2011e in Paper 1 respectively. The acquisition with the higher incidence angles (2011m) showed a higher degree of noise corruption, with open water on average being 3-7 dB above the noise floor, the slick of emulsion being 1-2 dB above the noise floor and the plant oil being on average 0-6 dB above the noise floor. The crude oil slick wasn't present in this scene. The scene with lower incidence angle values (2011e) showed a lower degree of noise corruption with open water on average being 9-15 dB above the noise floor, the slick of emulsion being 7-8 dB above the noise floor and the plant oil being on average 9-10 dB above the noise floor and the crude oil slick being on average 9-10 dB above the noise floor. It should be noted that despite the fact that wind speeds were recorded to be between 1.66 – 3.3 m/s, which is on the lower limit of slick detection, it can be seen that the lower values for backscatter recorded in the 2011m acquisition can be attributed to the high incidence angle range the data was acquired under.

In order to corroborate the noise analysis results presented in [Skrunes et al., 2014], as well as to investigate the noise profiles of the 2012m and 2013e acquisitions (the other two acquisitions that were presented in paper 1), an independent noise analysis was conducted. These results were not published as there was a high degree of overlap between [Skrunes et al., 2014]. However, for completeness, the results for the noise analysis of these four acquisitions are shown below in Figures 9.1 – 9.4. The same methodology as implemented by [Skrunes et al., 2014] was adopted here, where by the average backscatter values contained within boxes of 100 × 100 pixels in size were calculated as well as the standard deviation for each of the scattering surfaces contained within these SAR acquisitions. This is indicated by the vertical bars in Figures 9.1– 9.4.

Figure 9.1 and 9.2 display the results for the 2011m and 2011e acquisitions and agree with the assessments made by [Skrunes et al., 2014]. Figure 9.3 and 9.4 show the noise analysis results for the 2012m and 2013e acquisitions respectively. As can be seen, the average of the backscatter values are at least 9 dB above the noise floor of the sensor or greater. The incidence angles of these two acquisitions were 30.3° - 32.0° and 28.1°-29.9°, respectively, while wind speeds were 4 5 m/s and 5 m/s, respectively. The results of this noise analysis also concluded that the cross-polarization channels were unusable due to noise corruption.

Following [Minchew et al.,2012] and [Freeman and Durden, 1998], any pixels that have backscatter values that are at least 6 dB above the noise floor can be considered as not corrupted with noise. Given this limiting value, and the results of the noise analysis as shown in Figures 9.1 – 9.4, it can be concluded that it is possible to derive quantitative information about the internal state of an oil slick with the only major limiting factor being the incidence angle under which the acquisition was taken.

In paper 1, these four acquisitions were inverted for values of $|\varepsilon|$ using the PTSM. The PTSM was chosen as it builds upon the extended Bragg (XBragg) model, developed by [Hajnsek.,2003], by removing some simplifying assumptions. Due to the use of the co-polarization ratio, the PTSM modeled this quantity in terms of an equation that depended on two primary unknowns (see section 3.4.3 for a discussion on these points). An inversion procedure was presented that aimed to estimate values for the large-scale surface roughness *s*, before values for $|\varepsilon|$ could be determined by using a look-up table approach. The results yielded theoretically accurate values for $|\varepsilon|$, with histograms showing peaks around 2.3, the theoretical values for $|\varepsilon|$ of pure crude oil.

Although no in-situ data was available to confirm the results of this study, a methodology was presented that yielded realistic results that warranted further investigation.

The NORSE2019 oil-on-water experiment resulted in multitemporal and multifrequency airborne quad-polarimetric F-SAR data acquisitions of verified slicks of mineral oil emulsion and soybean oil acquired in X-, S- and L-bands in the North Sea. As shown in Paper 2, and then again in Paper 3, the noise characteristics of this data set varied.

In order to test the methodology presented in Paper 1, it was decided to try to apply the methodology to data sets where polarimetric information was available in the cross-polarimetric channels. In this way, the methodology presented in Paper 1 could be applied and then results could be compared to the case when the full PTSM was applied, i.e. both the co-polarimetric and cross-polarimetric channels could be modeled, and so no assumptions about

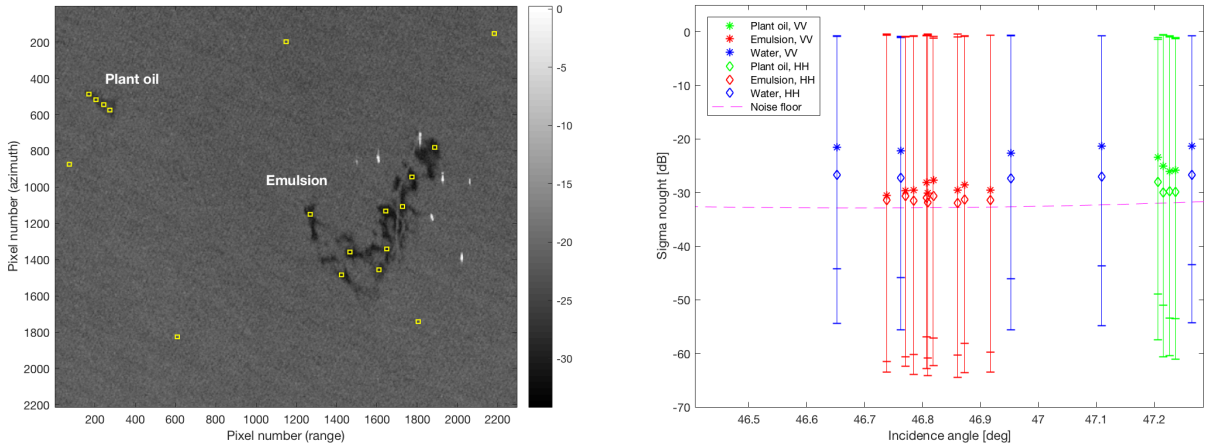

Figure 9.1: (Left) Intensity image ($\sigma^0_{VV}[dB]$), multi-looked by 9x9 window for Radarsat-2 acquisition (2011m in Paper 1). Yellow boxes indicate regions used in the noise analysis. (Right) Signal-to-noise analysis for the 2011m acquisition. Each vertical line shows the mean ± one standard deviation of the backscatter signal in the regions indicated by the yellow boxes in (Left). The purple line indicates the NESZ curve of the sensor. Note: image in (Left) is presented in Radar coordinates as it was acquired and so high incidence angle values are at the left side of this image. The Radarsat-2 data and Products © MDA LTD. 2011 – All Rights Reserved

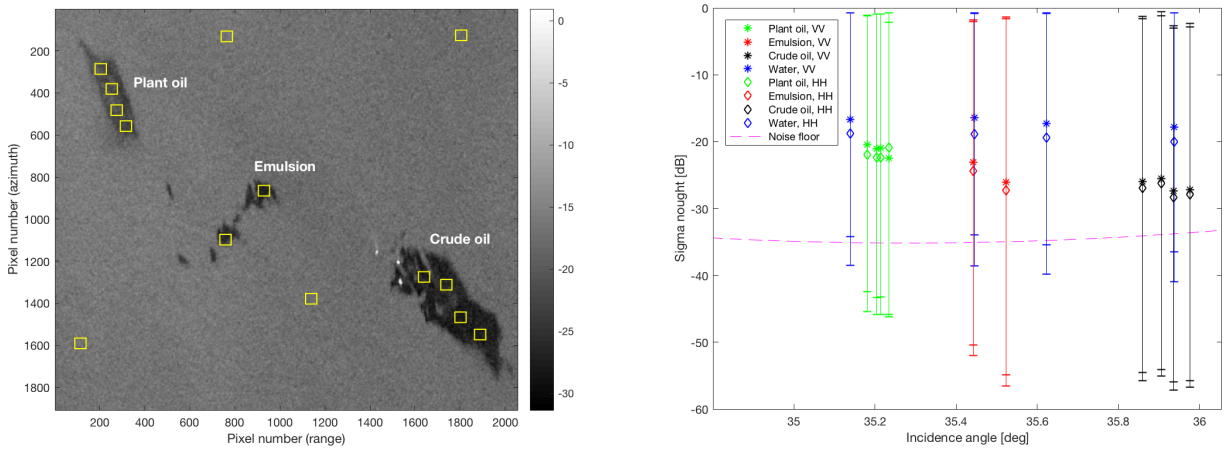

Figure 9.2: (Left) Intensity image ($\sigma^0_{VV}[dB]$), multi-looked by 9x9 window for Radarsat-2 acquisition (2011e in Paper 1). Yellow boxes indicate regions used in the noise analysis. (Right) Signal-to-noise analysis for the 2011e acquisition. Each vertical line shows the mean ± one standard deviation of the backscatter signal in the regions indicated by the yellow boxes in (Left). The purple line indicates the NESZ curve of the sensor. The Radarsat-2 data and Products © MDA LTD. 2011 – All Rights Reserved

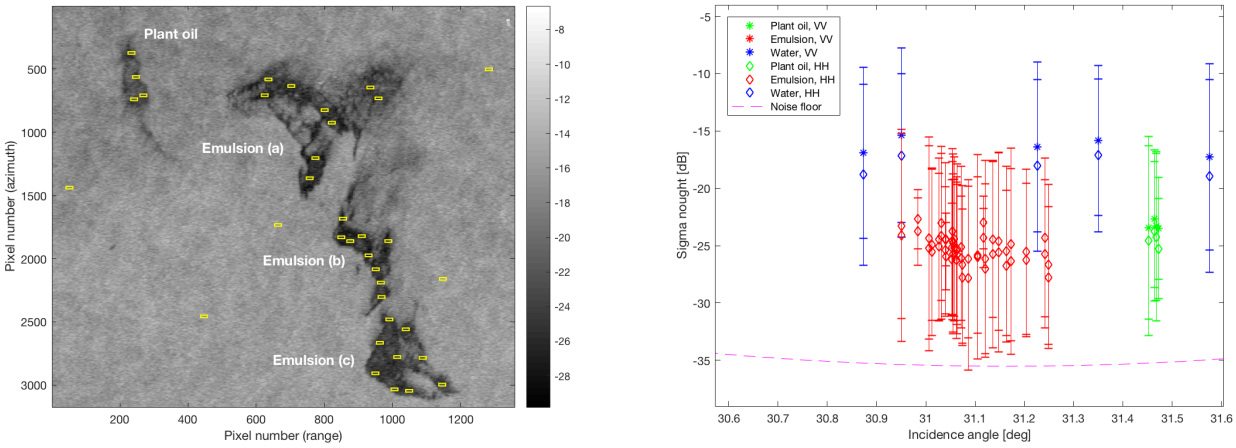

Figure 9.3: (Left) Intensity image ($\sigma^0_{VV}[dB]$), multi-looked by 9x9 window for Radarsat-2 acquisition (2012m in Paper 1). Yellow boxes indicate regions used in the noise analysis. (Right) Signal-to-noise analysis for the 2012m acquisition. Each vertical line shows the mean ± one standard deviation of the backscatter signal in the regions indicated by the yellow boxes in (Left). The purple line indicates the NESZ curve of the sensor. Note: image in (Left) is presented in Radar coordinates as it was acquired and so high incidence angle values are at the left side of this image. The Radarsat-2 data and Products © MDA LTD. 2012 – All Rights Reserved

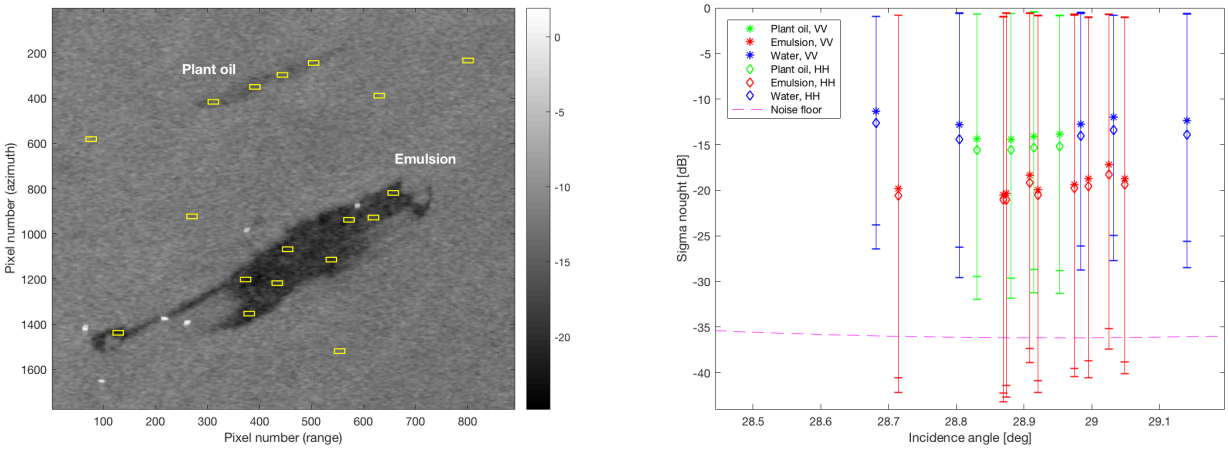

Figure 9.4: (Left) Intensity image ($\sigma^0_{VV}[dB]$), multi-looked by 9x9 window for Radarsat-2 acquisition (2013e in Paper 1). Yellow boxes indicate regions used in the noise analysis. (Right) Signal-to-noise analysis for the 2013e acquisition. Each vertical line shows the mean ± one standard deviation of the backscatter signal in the regions indicated by the yellow boxes in (Left). The purple line indicates the NESZ curve of the sensor. The Radarsat-2 data and Products © MDA LTD. 2013 – All Rights Reserved

the large-scale roughness indicator, s, had to be made. Note: going forward the method presented in Paper 1 will be referred to as method 1 and the method where both the co- and cross-polarization ratios are modeled will be referred to as method 2. This is the same convention presented in Paper 2. In this way, the results derived by applying method 2 were assumed to be more accurate and acted as a viable way to compare the two methodologies.

After a noise analysis, it was found that the L-band acquisitions were the only suitable data sets that were viable for this analysis. The results showed that low values for $|\varepsilon|$ (i.e. between 2 and 8) were correlated across both methods, but were less correlated at higher values. After conducting a sensitivity analysis, it was found that the PTSM was highly to values of s, especially at higher values for $|\varepsilon|$ (i.e. greater than 8). The conclusion of Paper 2 is that the methodology presented in Paper 1 is viable to use, but should be restricted to trying to determine low values of $|\varepsilon|$. Given that the rule of thumb for oil slick is that approximately 90% of the oil is contained in 10% of the surface area [Hollinger and Mennella, 1973], having only accurate estimations on low values of $|\varepsilon|$, may be sufficient for reliably estimating the amount of oil contained within slick.

Paper 3 attempted to delve into the benefits of using the F-SAR instrument in an operational setting for the purposes of determining values for $|\varepsilon|$ or for determining areas within slick that were more concentrated with oil as opposed to others. This paper first conducted a very detailed noise analysis on the X-, S- and L-band F-SAR data sets and found that the X-band acquisitions were unusable for this application. This is mainly due to internal system noise.

The S-band acquisitions showed a trend of having pixels external to the slick areas completely available in all four polarimetric channels i.e. all pixels were above the 6 dB threshold, while pixels within the slick areas showed a trend of having their pixels available in only the co-polarimetric channels. The L-band acquisitions had nearly 100% of their pixels available in all polarimetric channels.

In addition to the difficulty in working with the X-band data for this application, the difficulty in working with the L-band data was also demonstrated. This was linked to the penetration ability of the L-band radiation and was demonstrated by showing a time series of the L-band co-polarization ratio images.

Despite this, the advantages of having simultaneous multifrequency SAR data was demonstrated and a new polarimetric feature was proposed, which combined the information contained in the co-polarimetric ratios from each frequency band, and which could provide a heuristic based assessment on the regions within slick that were more concentrated with oil.

Following a procedure developed by [Espeseth et al., 2020], the time series aspect of the data set was exploited to try to determine where within the slick consistent zones of more concentrated oil lay over time. The philosophy of this stability measure was to derive a product that would provide first responders with an indication of the regions within a slick that are the most persistent. In their paper, [Espeseth et al., 2020] applied this measure to a time series of L-band UAVSAR data of an ocean floor oil seep using the damping ratio. In their paper, the source of the seep was known, and so a fixed point of reference could be applied to try to determine the consistently thickest parts of the slick. Paper 3 demonstrated that this stability measure could be applied to a time series of a freely floating oil slick combining multifrequency data, to determine the areas within the slick that were consistently more concentrated.

9.2 Future Outlook

A highly relevant polarimetric feature cited in the literature, called the damping ratio, which is a measure of the contrast between the oil slick area and the open ocean [Espeseth, 2019], has been reported to increase with the thickness of the emulsion layer. This has been assumed in the work of [Espeseth et al., 2020] but has also been reported in [Gade et al., 1998] and [Wismann et al., 1998]. In Paper 3, it is explained that the co-polarization ratio is assumed to provide an indication of the concentration of oil within slick. According to [ITOPF, 2002], as weathering processes occur on the ocean surface, specifically in regards to the process of emulsification, the volume of the pollutant can increase by a factor of five. In addition, the viscosity of the substance can increase dramatically as well. As emulsions form, it is not uncommon for viscosities of the order of 100,000 centistokes (cSt) to be measured [ITOPF, 2012]. In this regard, as the pollutant increases in thickness and viscosity, the concentration of oil can decrease, i.e. a higher damping ratio may be an indication of less mineral oil contained within a pixel.

One of the most common containment devices used by first responders in an oil spill event are collection booms which are free floating barriers designed to perform one or more of the following functions: oil containment and concentration, deflection and protection [ITOPF, 2011 (b)]. However, these systems have their limitations. Most conventional boom designs are not capable of containing oil against water velocities in excess of 0.5 m/s (1 knot) acting at right angles to it. However, in reality, oil can escape from one side of a boom to another in water velocities as low as 0.35 m/s (0.7 knots), irrespective of skirt depth of the boom [ITOPF, 2011 (b)]. Low viscosity oils generally escape at lower velocities than more viscous oils [ITOPF, 2011 (b)]. There are a variety of mechanisms in which oil that is present on one side of a boom may be transported to the other side. These are presented in Figure 9.5 below. As can be seen, some mechanisms can be due to the low viscosity of the pollutant, like entrainment or drainage failure for example, whereas others are due to wind or wave conditions present, like submergence, for example.

When booms are used to contain the oil, the method in which oil is then collected is via the use of skimmers [ITOPF, 2012]. In short, the booms act to concentrate the oil on the ocean surface and skimmers selectively recover and pump the oil to storage. The mechanisms in which oil is recovered from the water surface include oleophilic systems relying on adhesion of oil to a moving surface, suction systems, weir systems which rely on gravity as well as systems that physically lift the oil with mechanical scoops, belts or grabs [ITOPF, 2012]. The primary limitation on the efficiency of most skimming devices is the viscosity of the oil, where each skimming device has a range of acceptable viscosity regimes in which it can operate. See [ITOPF, 2012] for a more detailed discussion on this point. In addition, according to [Fingas, 2019], useful thickness measurements of oil slick need to be above 0.5 mm up to as much as 10 mm to be useful for oil spill countermeasures such as skimmers.

Given the complexity of oil spill clean-up operations which need to balance the current internal state of an oil slick against the clean-up mechanisms on-hand, as well as storage capacities on clean-up vessels, further research needs to be carried out on the practicality of having a numerical measure of oil concentration, such as the dielectric constant or co-polarization ratio, for oil spill clean-up operations.

Given the extent some oil spills can reach, i.e. on the scale of kilometers, a major concern for first responders can be related to the question of the most appropriate location within a slick to begin clean-up operations. Future studies should be aimed at producing an actionable product

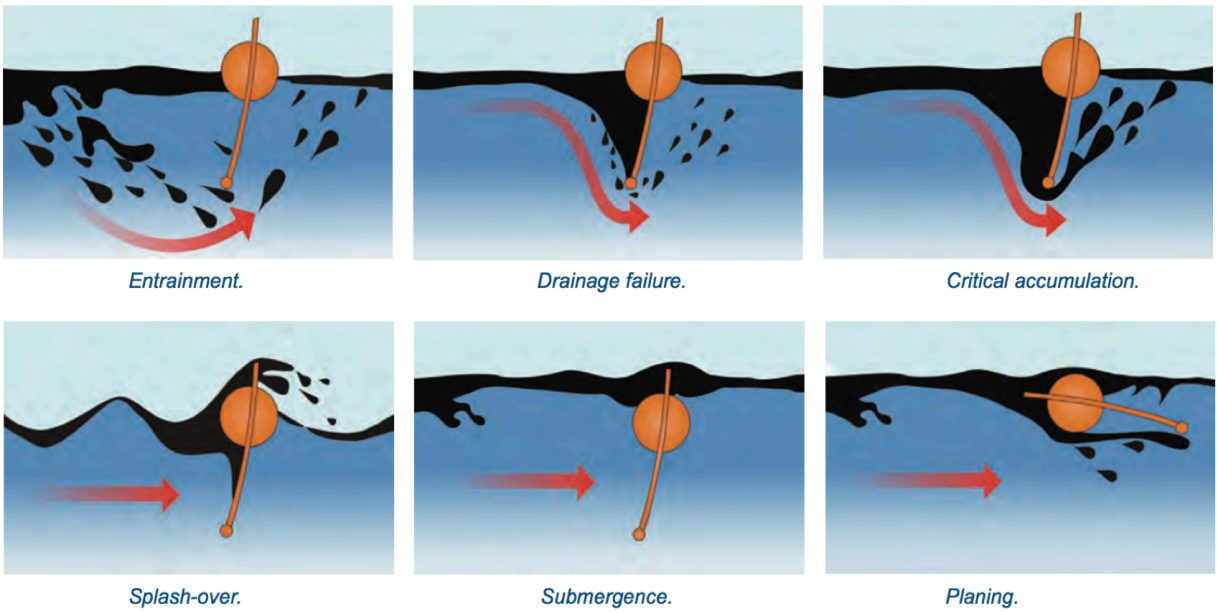

Figure 9.5: Various failure modes for oil booms. The current direction is indicated by the red arrow. Image is adapted from [ITOPF, 2011 (b)].

for the oil spill contingency community based on a combination of these two features, i.e. the damping ratio and the co-polarization ratio. A viable product that combines the information contained in these two features could produce a qualitative map of zones within slick, indicating the greatest chance of collecting the greatest amount of oil, optimized against other factors such as wind speed, wind direction, equipment available etc.

One way this may be achieved, is via the use of the Stability Level (SL) that was used in Paper 3 and which was developed by [Espeseth et al., 2020]. An attractive aspect of this method is that it works to highlight internal zones within a slick that meet a certain criterion, usually a threshold applied to a specific feature. A working hypothesis is that by examining the stability measure for both the co-polarization ratio as well as the damping ratio, maps of zones of internal stability may be derived that are anticorrelated, i.e. maps depicting persistent areas with high oil concentration but low damping, as well as maps depicting areas with low concentration but high thickness (high damping) may be utilized. Paper 3 demonstrated that is possible, at least in principle, to apply the stability level measure to SAR imagery of freely floating oil slick without a fixed point of reference. The only drawback is that a time series of SAR data is required. This may be challenging if applied to spaceborne SAR sensors.

As alluded to in a previous paragraph, the benefits of having a methodology for converting SAR data into values for the dielectric constant in an operational clean-up setting are not, as of yet, completely obvious. While the dielectric constant can provide a numerical indication for the volumetric content of oil within slick, heuristic measures, such as the co-polarization ratio, may be sufficient for clean-up operations. However, one area where having reliable values for the volume of oil spilled may be more related to law enforcement. As demonstrated in the introduction, the Arctic is set to undergo drastic environmental and industrial change in the coming century. Being able to derive reliable and timely information related to the amount of oil spilled in relation to illegal activities may prove vital in the years to come specifically in regards to bringing charges against polluting agents.

Thus, in order to attempt to derive more accurate results, a more sophisticated model should be applied and tested for this application. As already stated, the PTSM was chosen as it builds upon the XBragg model by removing some simplifying assumptions (section 3.4.3). The PTSM in its current formulation assumes that the large-scale surface slope distribution as well as the small-scale surface roughness spectrum are isotropic. For the case of the ocean surface, this is not fully realistic as anisotropy is dictated by the direction of the wind. In order to account for the surface roughness anisotropy, the authors in [Di Martino et al., 2019] developed the anisotropic PTSM (A-PTSM) for the purposes of modeling the backscatter from the ocean surface. The application of this model may provide more accurate results for the dielectric constant than the PTSM.

The gulf that exists between industry and academia can sometimes be significant as new knowledge that is generated within the academic sector can be too far removed from the realms of possibility to be applied in an operational setting. CIRFA, which is a center for research-driven innovation, aims to bridge the gap between the two sectors by collaborating and exchanging ideas and products that may have an impact on industry. The role of industry in applied scientific research cannot be understated. Industrial partners can express ambitions in relation to viable operational products which can steer scientific research. However greater communication is needed between the two sectors to bring more developed products online.

Works cited

[Alpers et al.,2017] Alpers,W., Holt,B., and Zeng,K.(2017).Oil spill detection by imaging radars: Challenges and pitfalls. *Remote Sens. Environ.,* 201:133-147.

[Angelliaume et al., 2018] Angelliaume, S., Boisot, O., Guerin, C.A. (2018). Dual-Polarized L-Band SAR Imgery for Temporal Monitoring of Marine Oil Slick Concentration. *Remote Sens.*, 10(7), 1012.

[Baghdadi et al., 2006] Baghdadi N., and Zribi M., (2006). Evaluation of Radar Backscatter Models IEM, OH and Dubois Using Experimental Observations. *International Journal of Remote Sens.*, 27(18): 3831-3852.

[Barrett et al.,2009] Barrett, B.W.; Dwyer, E., (2009). Soil Moisture Retrieval from Active Spaceborne Microwave Observations: An Evaluation of Current Techniques. *Remote Sens.,* 1:210-242.

[Bass et. al,1968 (a)] Bass, F.G., Fuks, I.M., Kalmykov, A.I., Ostrovsky, I.E., Rosenberg, A.D. (1968). Very High Frequency Radiowave Scattering by a Disturned Sea Surface Part I: Scattering from a Slightly Disturbed Boundary. *IEEE Trans. Antennas and Prop.* AP-16(5): 554-559.

[Bass et. al,1968 (b)] Bass, F.G., Fuks, I.M., Kalmykov, A.I., Ostrovsky, I.E., Rosenberg, A.D. (1968). Very High Frequency Radiowave Scattering by a Disturned Sea Surface Part II: Scattering from an Actual Sea Surface. *IEEE Trans. Antennas and Prop.* AP-16(5): 560-568.

[Bonn Agreement Secretariat, 2016] Bonn Agreement Secretariat (2016). Bonn Agreement Aerial Operations Handbook. Technical report. Available: https://www.bonnagreement.org/site/assets/files/1081/aeriaa_operations_handbook.pdf, Accessed on: Sept. 24, 2020.

[Brekke, 2008] Brekke, C. (2008). Automatic Screening of Synthetic Aperture Radar Imagery for Detection of Oil Pollution in the Marine Environment. PhD thesis, Faculty of Mathematics and Natural Sciences, Department of Informatics, University of Oslo.

[Brekke et al., 2014] Brekke, C., Holt, B., Jones, C. E., and Skrunes, S. (2014). Discrimination of oil spills from newly formed sea ice by synthetic aperture radar. *Remote Sens. Environ.*, 145:1-14.

[Brekke and Solberg, 2005] Brekke, C. and Solberg, A. H. S. (2005). Oil Spill Detection by Satellite Remote Sensing. *Remote Sens. Environ.*, 95(1):1-13.

[Canadian Space Agency, nd] Canadian Space Agency (n.d.). https://www.asc-csa.gc.ca/eng/satellites/radarsat/technical-features/radarsat-comparison.asp (last accessed 22 July 2020).

[Carpenter, 2015] Carpenter, A (2015) European Maritime Safety Agency CleanSeaNet Activities in the North Sea. In: Carpenter, A, (ed.) Oil Pollution in the North Sea. The Handbook of Environmental Chemistry, 41. Springer, Cham, pp. 33-47.

[Caruso, 2013] Caruso, M.J., M. Migliaccio, J.T. Hargrove, O. Garcia-Pineda, and H.C. Graber. (2013). Oil spills and slicks imaged by synthetic aperture radar. *Oceanography* 26(2):112-123.

[Choker et al., 2017] Choker, M., Baghdadi, N., Zribi, M., El Hajj, M., Paloscia, S., Verhoest, N.E.C., Lievens, H., Mattia, F. (2017). Evaluation of the Oh, Dubois and IEM Backscatter Models Using a Large Dataset of SAR Data and Experimental Soil Measurements. *Water*, 9(38).

[Chuvieco and Huete, 2010] Chuvieco, E. and Huete, A. (2010). Fundamentals of Satellite Remote Sensing. CRC Press Taylor and Francis Group.

[Curlander and McDonough, 1991] Curlander, J. C. and McDonough, R. N. (1991). Synthetic Aperture Radar, Systems & Signal Processing. John Wiley & Sons, INC., Wiley Series in Remote Sensing.

[Coleman, 2003] Coleman, J. (2003). Oil in the Sea III. National Academy Press, Washington DC, USA.

[Di Martino et al., 2019] Di Martino, G., Iodice, A., Riccio, D. (2019). Closed-Form Anisotropic Polarimetric Two-Scale Model for Fast Evaluation of Sea Surface Backscattering. *IEEE Trans. Geosci. Remote Sens.,* 57(8): 6182-6194.

[Elachi and van Zyl, 2006] Elachi, C. and van Zyl, J. (2006). Introduction to the Physics and Techniques of Remote Sensing. John Wiley and Sons, Inc., Publication, second edition.

[Espeseth, 2019] Espeseth, M. (2019). Analysis of Oil Spill and Sea Ice Measurements Using Full-Polarimetric and Hybrid-Polarity Synthetic Aperture Radar data. PhD thesis, Faculty of Science and Technology, Department of Physics and Technology, UiT The Arctic University of Norway.

[Espeseth et al., 2020] Espeseth, M.M., Jones, C.E., Holt, B., Brekke, C., Skrunes, S. (2020). Oil-Spill-Response-Orientated Information Products Derived From a Rapid-Repeat Time Series of SAR Images. *IEEE J. Sel. Topics Appl. Earth Observ. Remote Sens.*, 13:3448-3461.

[Fingas, 2019] Fingas, M (2019) Remote Sensing for Marine Management. In: Seppard, C, (ed.) World Seas: An Environmental Evaluation. Volume III: Ecological Issues and Environmental Impacts, pp. 103-119.

[Franceschetti and Riccio, 2007] Franceschetti, G. and Riccio, D. (2007). Scattering, Natural Surfaces, and Fractals. Elsevier Science & Technology, Publication, first edition.

[Freeman and Durden, 1998] Freeman, A., Durden, S. (1998). A three-component scattering model for polarimetric SAR data. *IEEE Trans. Geosci. Remote Sens.*, 36(3):963-973.

[Fung, 1994] Fung, A.K. (1994). Microwave Scattering and Emission Models and Their Applications. Artech House, Inc.

[Fung, 2010] Fung, A.K., Chen, K.S. (2010). Microwave Scattering and Emission Models for Users. Artech House, Inc.

[Gade et al., 1998] Gade, M., Alpers, W., Hühnerfuss, H., Masuko, H., and Kobayashi, T. (1998). Imaging of biogenic and anthropogenic ocean surface films by the multifrequency/multipolarization SIR-C/X-SAR. *J. Geophys. Res.*, 103(C9):18851-18866.

[Gadelmawla et al., 2002] Gadelmawla, E.S., Koura, M.M., Maksoud, T.M.A., Elewa, I.M., Soliman, H.H., (2002), Roughness parameters, J. Mater. Process. Tech., 123, 133-145

[Galley et al., 2016] Galley, R. J., Babb, D., Ogi, M., Else, B. G. T., Geilfus, N.-X., Crabeck, O., Barber, D. G., and Rysgaard, S. (2016), Replacement of multiyear sea ice and changes in the open water season duration in the Beaufort Sea since 2004, J. *Geophys. Res. Oceans*, 121: 1806-1823

[Grahn, 2018] Grahn, J. (2018). Multi-frequency radar remote sensing of sea ice: Modelling and interpretation of polarimetric ulti-frequency radar signatures of sea ice. PhD thesis, Faculty of Science and Technology, Department of Physics and Technology, UiT The Arctic University of Norway.

[Hajnsek, 2001] Hajnsek, I. (2001). Inversion of Surface parameters using polarimetric SAR. PhD thesis, Faculty of Chemistry and Earth Sciences, Friedrich Schiller University, Jena, Germany.

[Hajnsek et al.,2003] Hajnsek,I., Pottier,E. and Cloude,S.R. (2003).Inversion of surface parameters from polarimetric SAR. *IEEE Trans. Geosci. Remote Sens.*, 41(4):727-744.

[Ho, 2009] Ho, J. (2009). The implications of Arctic sea ice decline on shipping. *Marine Policy,* 34(3)*,* 713-715.

[Hollinger and Mennella, 1973] Hollinger, J. P. and Mennella, R. A. (1973). Oil spills: Measurements of their distributions and volumes by multifrequency microwave radiometry. *Science*, 181(4094):54-56.

[Hühnerfuss, 2006] Hühnerfuss, H. (2006). Basic physicochemical principles of monomolecular sea slicks and crude oil spills. Gade M., Hühnerfuss H., Korenowski G.M. (eds) Marine Surface Films. Springer, Berlin, Heidelberg, pages 21-35.

[Iodice et al., 2011] Iodice, A., Natale, A., Riccio, D. (2011). Retrieval of soil surface parameters via a polarimetric two-scale model. *IEEE Trans. Geosci. Remote Sens.*, 49(7): 2531-2547.

[ITOPF, 2002] ITOPF (2002). Fate of marine oil spills. *The International Tanker Owners Pollution Federation Limited, Technical report*.

[ITOPF, 2011 (a)] ITOPF (2011). Aerial observation of marine oil spills. *The International Tanker Owners Pollution Federation Limited, Technical report.*

[ITOPF, 2011 (b)] ITOPF (2011). Use of Booms in Oil Pollution Response. *The International Tanker Owners Pollution Federation Limited, Technical report.*

[ITOPF, 2012] ITOPF (2012). Use of Skimmers in Oil Pollution Response. *The International Tanker Owners Pollution Federation Limited, Technical report.*

[ITOPF, 2018] ITOPF (2018). Country and Territory Profiles. A Summary of Oil Spill Response Arrangements and Resources Worldwide. *The International Tanker Owners Pollution Federation Limited, Technical report.*

[Kasilingam et al., 1997] Kasilingam, D.,Lin, I.-I.,Lim, H.,Khoo, V.,Alpers, W.,Lim, T.K. (1997). Investigation of tropical rain cells with ERS SAR imagery and ground-based weather radar. European Space Agency, (Special Publication) ESA SP 414 (3) :1603-1608.

[Klein and Swift 1977] Klein, L. A., Swift, C.T. (1977). An improved model for the dielectric constant of sea water at microwave frequencies. *IEEE Trans.on Anten. And Prop.,* 25(1): 104-111.

[Lee and Pottier, 2009] Lee, J.-S. and Pottier, E. (2009). Polarimetric Radar Imaging: from basic to applications. Optical Science and Engineering. CRC Press Taylor and Francis Group.

[Minchew et al.,2012] Minchew,B., Jones,C.E., and Holt,B. (2012).Polarimetric Analysis of Backscatter From the Deepwater Horizon Oil Spill Using L-Band Synthetic Aperture Radar. *IEEE Trans. Geosci. Remote Sens.,* 50(10):3812-3830.

[NSIDC, nd] National Snow and Ice Data Center http://nsidc.org/arcticseaicenews/2017/05/ (last accessed 16 July 2020).

[Panciera et al., 2013] Panciera, R., Tanase, M.A., Lowell, K., Walker, J.P. (2013). Evaluation of IEM, Dubois, and Oh Radar Backscatter Models Using Airborne L-Band SAR. *IEEE Trans. Geosci. Remote Sens.*, 52(8):4966-4979.

[Park N.L., 2014] N. Laurel Park (2014). Michigan Metrology Surface Texture Parameters Glossary. Michigan Metrology LLC.

[Plant, 1990] Plant, W.J. (1990) Bragg Scattering of Electromagnetic Waves from the Air/Sea Interface. In: Geernaert, G.L., Plant,W.J. (ed.) Surface Waves and Fluxes. Volume II: Remote Sensing, pp. 41-109.

[Quigley et al., 2020] Quigley, C., Brekke, C., Eltoft, T. (2020), Comparison Between Dielectric Inversion Results from Synthetic Aperture Radar Co- and Quad-Polarimetric Data via a Polarimetric Two-Scale Model. *IEEE Trans. Geosci. Remote Sens.* (submitted).

[Rice, 1951] Rice, S.O. (1951). Reflection of Electromagnetic Waves from Slightly Rough Surfaces. Comm. Pure Appl. Math, 4: pp. 351-378.

[Shivola, 2000] Sihvola, A. (2000). Mixing Rules with Complex Dielectric Coefficients. *Subsurface Sensing Technologies and Applications* 1**,** 393-415.

[Shivola, 2008] Shivola, A. (2008). Electromagnetic Mixing Formulas and Applications. Institution of Engineering and Technology. London, UK.

[Skrunes et al., 2014] Skrunes, S., Brekke, C., and Eltoft, T. (2014). Characterization of Marine Surface Slicks by Radarsat-2 Multipolarization Features. *IEEE Trans. Geosci. Remote Sens.,* 52(9):5302-5319.

[Skrunes et al., 2017] Skrunes, S., Brekke, C., and Espeseth, M. M. (2017). Assessment of the RISAT-1 FRS-2 mode for oil spill observation. *IEEE Int. Geosci. Remote Sens. Symp. (IGARSS) Proceedings*, pages 1024-1027.

[Stiassnie et al., 1991] Stiassnie, M., Agnon, Y., and Shemer, L. (1991). Fractal dimensions of random water surfaces. *Phys. D, Nonlinear Phenomena,* 47(3)*:* 341-352.

[Sutherland, 2014] Sutherland B. R. (2014). Cambridge University Press.

[UNCTAD, 2019] UNCTAD (2019). Review of Marine Transport, 2019. The United Nations Conference on Trade and Development, Technical report.

[van Zyl and Kim, 2010] van Zyl, J. and Kim, Y. (2010). Synthetic Aperture Radar Polarimetry. WILEY.

[Wismann et al., 1998] Wismann, V., Gade, M., Alpers, W., and Hühnerfuss, H. (1998). Radar signatures of marine mineral oil spills measured by an airborne multi-frequency radar. *Int. J. Remote Sens.*, 19(18):3607-3623.

[Woodhouse, 2006] Woodhouse, I.H. (2006). Introduction to Microwave Remote Sensing. Taylor and Francis.

[Wright,1966] Wright, J.W. (1966). Backscattering from Capillary Waves with Application to Sea Clutter. *IEEE Trans. Antennas and Prop.* AP-14(6): 749-754.

[Wright,1968] Wright, J.W. (1968). A New Model for Sea Clutter. *IEEE Trans. Antennas and Prop.* AP-16(2): 217-223.

[WTO, 2015] WTO (2015). The WTO at Twenty, Challenges and Achievements. *World Trade Organization, Technical report.*

[Younis et al., 2009] Younis, M., Huber, S., Patyuchenko, A., Bordoni, F., Krieger, G. (2009). Performance Comparison of Reflector- and Planar-Antenna Based Digital Beam-Forming SAR. *International Journal of Antennas and Propagation*. 2009:1-13